

**Theoretical Analysis and Large-Eddy Simulations of
the Propagation of Land-Surface Heterogeneity in
the Atmosphere**

Inaugural-Dissertation

zur

Erlangung des Doktorgrades

der Mathematisch-Naturwissenschaftlichen Fakultät

der Universität zu Köln

vorgelegt von

Michael Hintz

aus Radevormwald

Köln 2016

Gutachter:

1. Berichterstatter (Betreuer): Prof. Dr. Yaping Shao

2. Berichterstatter: Prof. Dr. Stefan Kollet

Tag der mündlichen Prüfung: 1. Dezember 2015

To my Father

Zusammenfassung

Die vorliegende Arbeit beschäftigt sich mit der Frage wie man Bodenheterogenitäten quantifizieren kann und wie sie sich auf die atmosphärische Grenzschicht auswirken. In der Grenzschicht werden Energie und Masse hauptsächlich durch große Wirbel transportiert. Deswegen ist es wichtig zu verstehen, welche Auswirkungen Heterogenitäten auf diese Wirbel haben. Da diese Wirbel eine komplexe Struktur besitzen und auf einer großen Bandbreite von Skalen variieren, ist es sehr aufwendig Informationen über sie durch Messungen zu erhalten. Hoch aufgelöste Modelle bieten hier eine Alternative. In dieser Studie, wird ein zwischen Boden und Atmosphäre gekoppeltes großes Wirbel Model verwendet. Dieses ist in der Lage die großen Wirbel explizit aufzulösen und kann so benutzt werden, die auftretenden Fragestellungen zu beantworten.

In dieser Arbeit wird eine kurze Einführung in die Theorie der großen Wirbel Simulationen gegeben. Außerdem gibt sie einen Überblick über einige der Verfahren welche benutzt werden um Heterogenitäten zu quantifizieren. Die in dieser Arbeit entwickelte Methode, die sogenannte Entropiespektrumsmethode, welche zur Quantifizierung verwendet wird, wird anschließend erklärt. Bei dieser Methode werden die räumlich verteilten Daten (sowohl atmosphärische Größen als auch Landoberflächenparameter) mit Hilfe der Wavelettransformation in hoch- und tiefpassgefilterten Anteile zerlegt. Für jeden einzelnen Anteil wird anschließend die Shannon Entropie berechnet. Es wird außerdem gezeigt, wie man mit Hilfe der Entropiespektrumsmethode die dominante Skala einer Heterogenität bestimmen kann.

Um zu zeigen, welchen Einfluss unterschiedliche Heterogenitäten auf die atmosphärische Grenzschicht haben, werden neun verschiedene Landnutzungsmuster untersucht. Für jedes Muster werden Simulationen mit dem gekoppelten großen Wirbelmodel durchgeführt. Die Simulationsergebnisse werden mit der Entropiespektrumsmethode untersucht. Dies geschieht für die potentielle Temperatur, das Wasserdampfmischungsverhältnis, sowie für den sensiblen und den latenten Wärmefluss. Die Untersuchung wird sowohl für instantane und als auch für zeitlich gemittelte Werte durchgeführt. Die Anwendung der Methode auf die Modellergebnisse dient außerdem der Untersuchung ab welcher Höhe der Einfluss der Heterogenität vernachlässigbar ist. Die Ergebnisse zeigen, dass das Verhalten des Entropiespektrums davon abhängt, welche Größe untersucht wird. Dies läßt vermuten, dass die atmosphärische Antwort auf Landoberflächenheterogenität sehr komplex ist. Des Weiteren zeigt sich, dass für die gewählten Heterogenitäten die instantanen Werte weniger Aussagekraft darüber besitzen, ab wann der Einfluss des Bodens vernachlässigbar ist, als die zeitlich gemittelten Werte. Die Analyse

der Spektren zeigt eine stärkere Abhängigkeit von der betrachteten physikalischen Größe als von der verwendeten Landnutzung. Die Ergebnisse zeigen, dass für die untersuchten Daten der Einfluss der Heterogenität oberhalb von 400 m für die gemittelte potentielle Temperatur und das gemittelte Wasserdampfmischungsverhältnis; oberhalb von 260 m für den gemittelten sensiblen Wärmefluss; und für variierende Höhen für den gemittelten latenten Wärmefluss, vernachlässigbar ist. Ab dieser Höhe überwiegt das Eigenmuster, welches durch die Selbstorganisation der Turbulenz erzeugt wird, den Einfluss der Landoberflächenheterogenität.

Ein Vergleich der Entropiespektrumsmethode, welche den Informationsaspekt der Heterogenität beschreibt, mit statischen Methoden, welche die Struktur beschreiben, zeigt für homogene und zufällige Muster gute Übereinstimmung. Für eine real existierende Heterogenität ist die Entropiespektrumsmethode überlegen. Die Entropiespektrumsmethode zeigt außerdem, welchen Einfluss die Auflösung der Heterogenität auf die Atmosphäre hat. Dieser ist wieder abhängig von der betrachteten physikalischen Größe und ob die zugrunde liegenden Heterogenität korreliert oder zufällig angeordnet ist.

Abstract

This thesis deals with the questions how land-surface heterogeneity can be quantified and how it can influence the atmospheric boundary layer. In this layer energy and mass are mainly transported by large eddies and therefore, it is important to understand how they are affected by the land-surface heterogeneities. Since large eddies have complex structures, which vary on a wide range of scales, it is highly demanding to obtain knowledge about them via measurements. High-resolution models offer an alternative. In this study, an atmosphere and land-surface coupled large-eddy simulation (LES) model, which explicitly resolves the large eddies, is used to address the concerned questions.

In this thesis a short introduction to the theory of LES is given, followed by an outline of some approaches for heterogeneity quantification. The method developed in this study for the quantification, namely, the entropy spectrum method, is then explained. In this method, the spatially-distributed data (of atmosphere and land-surface quantities and parameters) are decomposed into low- and high-pass filtered parts via wavelet transformation. For each part, the Shannon entropy is calculated. It is elaborated how to obtain from the entropy spectrum the dominant scale of the heterogeneity.

In order to investigate how land-surface heterogeneity influences the atmospheric boundary layer, nine different land-use patterns are designed. Simulations with the atmosphere and land-surface coupled LES model are carried out for each of these patterns. The simulation results, including potential temperature, water-vapor-mixing ratio, sensible and latent heat fluxes, are analyzed with the entropy spectrum method. The analysis is done for instantaneous as well for temporally averaged values and is found useful for identifying the height above which the influence of land-surface heterogeneity is negligible. The results show that the entropy spectra differ for different atmospheric variables, suggesting that the response of the atmosphere to land-surface heterogeneity is rather complex. In addition, it is shown that for a given land-surface pattern, the instantaneous values are less helpful to answer the question above which height the influence of the heterogeneity is negligible, than the temporally averaged values. The analysis with the temporally averaged values shows larger differences between the spectra of different parameters than between the spectra of the same parameter for different heterogeneities. From the results, it is concluded that for the cases investigated, the influence of the heterogeneity is negligible above 400 m height for the averaged values of potential temperature and water-vapor-mixing ratio; 260 m for the averaged sensible heat flux (of some experiments); and varying heights for the averaged latent heat flux. Above these heights it is concluded that the Eigen-pattern

arising from the self-organization of turbulence prevails over the influences of the land-surface heterogeneity.

A comparison of entropy, which describes the information aspect of heterogeneity, with statistical methods, which describe the structure aspect of heterogeneity, shows a good agreement for homogeneous and random patterns. For a real existing heterogeneity, the entropy spectrum method is superior. Moreover, the entropy spectrum method shows how the resolution of heterogeneity influences the atmosphere. This influence is dependent on the investigated physical variable and if the investigated heterogeneity is correlated or random.

Contents

1	Introduction	1
2	Turbulent Flows in the Atmosphere	7
2.1	Governing Equations	7
2.2	The Closure Problem	14
2.3	Monin-Obukhov Similarity Theory	15
2.4	Large-Eddy Simulation	19
3	Existing Methods for Heterogeneity Quantification	31
3.1	Taylor Diagram	32
3.2	Variogram	34
3.3	Power Spectrum	35
3.4	Probability Density Function	35
3.5	Wavelet Transformation	36
3.6	Entropy	38
3.7	Entropy Spectrum	46
4	Methodology	51
4.1	Estimation of the Dominant Scale	51
4.2	Data and Model Setup	55
4.3	Entropy Analysis of the Land Use Patterns	56
5	Results	65
5.1	Normalization	65
5.2	Responses to a Homogeneous Pattern	67
5.3	Instantaneous Responses	69

5.4	Temporally Averaged Responses	72
5.5	The Influence of Resolution	81
5.6	Comparison to other Methods	86
6	Conclusion	95

List of Figures

Figure 2.1	LES-ALM configuration	26
Figure 2.2	Comparison of the LES-ALM with measurements	28
Figure 3.1	Geometric relationship between R , E' , σ_f and σ_r	33
Figure 3.2	Example of a Taylor diagram	34
Figure 3.3	Example of a homogeneous and a heterogeneous pattern	36
Figure 3.4	Patterns to illustrate the problem of entropy	44
Figure 3.5	Illustration of the entropy spectrum method	47
Figure 3.6	Illustration of the reference entropy spectrum	48
Figure 4.1	High-resolution random data with the same PDF	52
Figure 4.2	Entropy spectrum to distinguish pattern with same PDF	52
Figure 4.3	Input data for the nine numerical experiments	57
Figure 4.4	Entropy spectra for the model input	58
Figure 5.1	Temperature pattern for a homogeneous land surface	67
Figure 5.2	Water-vapor-mixing-ratio for a homogeneous land surface	68
Figure 5.3	Entropy spectrum of the instantaneous values of Θ , q , H , LE	69
Figure 5.4	Entropy spectrum of the averaged values of Θ , q , H , LE	73
Figure 5.5	Scale of S_{max} for the averaged value of Θ	75
Figure 5.6	Scale of S_{max} for the averaged value of q	77
Figure 5.7	Scale of S_{max} for the averaged value of H	79
Figure 5.8	Scale of S_{max} for the averaged value of LE	81
Figure 5.9	Influence of resolution of correlated land use patterns	83
Figure 5.10	Influence of resolution of uncorrelated land use patterns	85
Figure 5.11	Example Taylor diagram of model results	87
Figure 5.12	Comparison between entropy, R and E' for experiment (a)	89

Figure 5.13 Comparison between entropy, R and E' for experiment (c)	92
Figure 5.14 Comparison between entropy, R and E' for experiment (d)	93

List of Tables

Table 2.1	Illustration of the closure problem	14
Table 4.1	Model setup and comparison with <i>Shao et al.</i> [2013]	55
Table 4.2	Conversion between land use types and albedo values	56
Table 4.3	Entropy of the different land use inputs and entropy values of averaged Θ , q , H and LE at the surface	59

1 Introduction

Modern weather forecasting and climate projection rely primarily on numerical models. To improve these models, it is necessary to better understand the physical processes which influence the weather and climate system and to better represent them in the models. Of particular interest to this study are the atmosphere and land-surface interactions over heterogeneous areas that determine the model lower boundary conditions. In recent years, the resolution of weather and climate models has significantly increased, from 10 km to 1 km in the case of numerical weather forecast and from 100 to 10 km in the case of climate projection. However, the resolutions are still insufficient to resolve all relevant processes, and the unresolved processes have to be parametrized. There are two types of parametrization: the first type involves the representation of the interactions between the model-resolved (grid-scale) and model-unresolved (sub-grid-scale) processes, known also as the closure problem, and the second type involves the representation of the interactions between the atmosphere and the other components of the weather/climate system, e.g. between the atmosphere and the land surface, i.e., the parametrization of the model boundary conditions.

An effective transport mechanism in the atmospheric boundary layer is the convection by large eddies, and hence to investigate the atmosphere and land-surface interactions on the large-eddy scale is of particular importance. As large eddies span over a wide range of scales, high-resolution data both in space and time for variables like temperature, humidity and wind speed are required for their characterization. It is highly demanding to obtain such data via measurements, although concerted effort has been made over the years in field campaigns. The difficulty is in particular to obtain suitable data sets for the characterization the atmosphere

1. Introduction

and land-surface coupled system over heterogeneous land surfaces. As an alternative, large-eddy simulations (LES) (cf. Section 2.4) can be used to generate high-resolution synthetic data for the purpose. In recent years, LES models have been substantially improved for studying atmosphere and land surface interactions.

Most weather and climate models assume a spatially homogeneous land surface on the sub-grid scale. This is reflected in the fact, that the parametrization of surface fluxes relies on the Monin-Obukhov Similarity Theory (cf. Section 2.3). This assumption may be in general too simplistic. Studies so far have demonstrated that land-surface heterogeneity on the grid scale as well as on the subgrid scale are both important to the exchanges of energy and mass between the atmosphere and the land surface (e.g. *Hechtel et al.* [1990]; *Mahrt* [2000]; *Heinemann and Kerschgens* [2005]).

On the subgrid scale, studies (e.g. *Avissar and Pielke* [1989], *Shao et al.* [2001]) identified the "aggregation effects" and "dynamic effects" of heterogeneity. The aggregation effect occurs because the fluxes estimated using spatially averaged state variables differ from spatially averaged fluxes. This is a consequence of the non-linear relationships between the fluxes and the state variables. Dynamic effects occur because land-surface heterogeneity can generate sub-grid-scale motions, which contribute to the exchange processes, but are not accounted for in the parametrization.

A widely used method for the treatment of land-surface heterogeneity in land-surface schemes is the "mosaic" method (*Avissar and Pielke* [1989]; *Koster and Suarez* [1992]) in which land-surface cells with the same properties are grouped into patches for which the fluxes are then computed. This method recognizes the importance of the land-surface properties, but neglects the spatial variations of the atmospheric variables and the dynamic effects associated with land-surface heterogeneity.

More recently, a downscaling technique has been proposed by *Schomburg et al.*

[2010], which takes the effect of land-surface heterogeneity on the atmosphere into account. However, this technique is mainly a statistical manipulation of the data and is not a sufficient representation of the dynamic effects. The resolution is an important issue of modeling the atmosphere. The modeling of the land-surface itself on the grid-resolved scale is difficult. In addition, if land-surface heterogeneity lies on a sub-grid-scale of the model, it is difficult to resolve the effect of land-surface heterogeneity on the grid-scale.

Mahrt [2000] gave an overview of the blending height concept. He viewed the blending height as a scaling depth that describes the decrease of the influence of surface heterogeneity with height. The author was aware of the fact that the blending height is not a level where the influence of the surface heterogeneity suddenly and completely vanishes, but a height where the influence of the surface heterogeneity decreases below a threshold. This concept is useful for some applications. However, to find a universal threshold value is in general difficult. In addition, for most of the blending height concepts there is only one heterogeneity scale. The problem how to obtain this heterogeneity scale, leads to the problem how to quantify it.

One current research goal is to parametrize heterogeneous land-surface processes in weather and climate models. In order to achieve this goal several steps are necessary: (1) development of an LES model to obtain high-resolution data; (2) development of suitable decompositions of land-surface heterogeneity; (3) quantification of land-surface heterogeneity; (4) investigation of the propagation of land-surface heterogeneity in the atmospheric boundary layer; (5) describing the heterogeneity with only a few parameters in order to reconstruct land-surface heterogeneity; and (6) parametrization of land-surface heterogeneity in weather and climate models.

Point (1), the development of an LES model, has already been done by *Shao et al.* [2013]. With this model it is possible to obtain the high-resolution data needed to investigate the structure of the atmospheric boundary. The emphasis of this thesis are the points (2) - (4). Possible decomposition methods are the Fourier transfor-

1. Introduction

mation and the wavelet transformation (*Morlet et al.* [1982]; *Daubechies* [1990]). Both of them have been used in various applications (*Bacry et al.* [1993]; *Briggs and Levine* [1997]). In this thesis the wavelet transformation is used, because it keeps the prominent features of the heterogeneity unchanged.

For the quantification of land-surface heterogeneity many approaches are possible. Which one should be used depends on the scientific question. *Garrigues et al.* [2006] gave an overview of the methods used for the quantification of spatial heterogeneity. These include the autocorrelation (*Ford* [1976]), fractals (*Mandelbrot* [1983]), the local variance (*Woodcock and Strahler* [1987]), the variogram (*Curran* [1988]), spectral methods (*Hough* [1989]), the hierarchical decomposition (*Woodcock and Harward* [1992]) or the probability density function (PDF) (*Giorgi* [1997]). Other studies (e.g. *Andraud et al.* [1998]; *Van Siclen* [1997]; *Fjellstad et al.* [2001]), make use of the information entropy (*Shannon* [1948]). Some studies combine the variogram with wavelet transformation (*Gloaguen and Dimitrakopoulos* [2009]), while others use empirical orthogonal functions, cf. *Hannachi et al.* [2007] for a review. However, in this thesis the entropy spectrum method is independently developed and used, which is a combination of the Shannon entropy and wavelet transformation. In some earlier studies (*Labat* [2005]; *Brunsell et al.* [2008, 2011]; *Brunsell and Anderson* [2011]), aspects of the method proposed in this thesis have been used.

Another focus of this study is on point (4), i.e., the investigation of the propagation of land-surface heterogeneity in the atmospheric boundary layer. This point has been studied to some extent by *Courault et al.* [2007]; *Huang and Margulis* [2009] and *Shao et al.* [2013]. In this thesis, the focus lies on the response of atmospheric quantities such as temperature, moisture, sensible and latent heat fluxes to land-surface heterogeneity. To this end, atmosphere and land-surface coupled large-eddy simulations are carried and the results are analyzed with the entropy spectrum method.

In this thesis, the following two research questions are examined:

1. How to quantify land-surface heterogeneity?
2. Above which height is the influence of land-surface heterogeneity negligible?

The answer to the first question is the quantification of land-surface heterogeneity with the entropy spectrum method. The second question is answered by investigating the entropy spectra at different heights of the simulation results obtained with a coupled LES model.

The outline of the thesis is as follows. In Chapter 2 the basic theory for LES is given. In Chapter 3 a brief review of some existing methods for heterogeneity quantification is given. In Chapter 4 the improvements to the entropy spectrum and the input data and the model setup are described. In addition, an analysis of the different land-use patterns with the entropy spectrum method is shown. In Chapter 5 the results from the LES model are shown in order to investigate the atmospheric response to the different land use patterns. As an example the patterns and spectra for a homogeneous land-use pattern are shown. Afterwards, the atmospheric responses on different time scales to land-surface heterogeneity are investigated. It is also dealt with the question how the resolution of the land-use patterns influences the entropy spectra. In addition, a comparison of the entropy spectrum method with other methods is done. The thesis is closed with a conclusion.

1. Introduction

2 Turbulent Flows in the Atmosphere

2.1 Governing Equations

In order to understand the results of the present thesis, it is necessary to first explain the model with which they are obtained. The large eddy version of the WRF (Weather Research and Forecast) model is used for this study. WRF, a numerical weather prediction model, solves a set of equations for the atmospheric motion, known as the governing equation, which consists of the continuity equation, the equation of motion, the conservation of moisture, the conservation of energy and the equation of state. As the governing equations are coupled and contain non-linear terms, they must be solved numerically.

The differences between the models for atmospheric motions on different scales are diminishing. A numerical weather prediction (NWP) model can be used today for LES, if the model resolution is sufficiently high. Models, which can explicitly resolve the large-eddy scale turbulent processes in the atmosphere, i.e., the model resolution corresponds to the inertial sub-range of the turbulence, are called LES models. In order to understand how an LES model works, it is necessary to understand the governing equations for atmospheric turbulent flows and to know how they are solved. In this Chapter, the governing equations are presented, followed by an illustration of the averaging method used in most NWP models. The closure problem together with the assumption of spatial homogeneity, which is made in most NWP/climate models, is then discussed. After the discussion of these basics, the technique of LES is explained.

2. Turbulent Flows in the Atmosphere

2.1.1 Continuity Equation

The conservation of mass states that the temporal change of density ρ in a certain volume is determined by the divergence of the mass flux $\rho\mathbf{u}$,

$$\frac{\partial\rho}{\partial t} + \nabla \cdot (\rho\mathbf{u}) = 0. \quad (2.1)$$

Where \mathbf{u} is velocity and ∇ is the Nabla operator. This equation can be written in its component form using the summation convention that a summation goes over double indices in one term,

$$\frac{\partial\rho}{\partial t} + \frac{\partial\rho u_j}{\partial x_j} = 0. \quad (2.2)$$

For velocities much smaller than the speed of sound, the air can be assumed as an incompressible fluid and Equation (2.2) reduces to

$$\frac{\partial u_j}{\partial x_j} = 0, \quad (2.3)$$

which is known as the incompressibility approximation. For this kind of fluids, ρ does not depend on position \mathbf{x} or time t .

2.1.2 Equation of Motion

The derivation of the equation of motion starts with Newton's second law $\mathbf{F} = m\mathbf{a}$, i.e., force equals mass times acceleration. Mainly three external forces act on an air parcel in the atmosphere. These forces are the gravitational force, the Coriolis force and the pressure gradient force. The gravitational force is $\mathbf{F}_g = -m\mathbf{g}$, with $\mathbf{g} = (0, 0, 9.81 \text{ m/s}^2)^T$. The Coriolis force is $\mathbf{F}_c = 2m\mathbf{u} \times \boldsymbol{\Omega}$, with \mathbf{u} the velocity of the particle and $\boldsymbol{\Omega} = (0, \omega \cos \phi, \omega \sin \phi)^T$ the angular velocity vector, with the latitude ϕ and ω the angular velocity of the earth. The pressure gradient force is $\mathbf{F}_p = -\frac{m}{\rho}\nabla p$, with the density ρ and the pressure p . With this, it follows the equations of motion

$$\mathbf{F} = m\mathbf{a} = m\frac{d\mathbf{u}}{dt} = -2m\boldsymbol{\Omega} \times \mathbf{u} - m\mathbf{g} - \frac{m}{\rho}\nabla p. \quad (2.4)$$

If the total time derivative is decomposed and divided by the mass, the results are the Euler equations

$$\frac{\partial \mathbf{u}}{\partial t} + \mathbf{u} \nabla \cdot \mathbf{u} = -2\boldsymbol{\Omega} \times \mathbf{u} - \mathbf{g} - \frac{1}{\rho} \nabla p. \quad (2.5)$$

In the following the so-called flux form of the Euler equations will be derived. For a quantity a given in advection form, i.e. $u_j \frac{\partial a}{\partial x_j}$, the flux form can be obtained by adding the continuity equation multiplied by a .

$$u_j \frac{\partial a}{\partial x_j} + a \underbrace{\frac{\partial u_j}{\partial x_j}}_{=0} = \frac{\partial (a u_j)}{\partial x_j}. \quad (2.6)$$

If the advection form of Equation (2.5) is written in its components, it follows that

$$\frac{\partial u_i}{\partial t} + u_j \frac{\partial u_i}{\partial x_j} = \varepsilon_{ij3} f_c u_j - \delta_{i3} g - \frac{1}{\rho} \frac{\partial p}{\partial x_i}. \quad (2.7)$$

With ε_{ijk} being the Levi-Civita-Pseudo-Tensor, δ_{ij} the Kronecker delta and where $f_c = 2\omega \sin \phi$ denotes the Coriolis parameter. From Equation (2.7) follows the Euler equations in flux form

$$\frac{\partial u_i}{\partial t} + \frac{\partial (u_i u_j)}{\partial x_j} = \varepsilon_{ij3} f_c u_j - \delta_{i3} g - \frac{1}{\rho} \frac{\partial p}{\partial x_i}. \quad (2.8)$$

The Euler Equations are valid for a fluid without friction. If the viscous stress for an incompressible fluid $\frac{\mu}{\rho} \Delta \mathbf{u}$ (*Landau and Lifshitz* [1987]; *Prager* [2004]), where μ is the viscosity, is added to Equation (2.8) it follows the Navier-Stokes equations for an incompressible fluid

$$\frac{\partial \mathbf{u}}{\partial t} + \mathbf{u} \nabla \cdot \mathbf{u} = -2\boldsymbol{\Omega} \times \mathbf{u} - \mathbf{g} - \frac{1}{\rho} \nabla p + \nu \Delta \mathbf{u}, \quad (2.9)$$

where the kinematic viscosity $\nu = \frac{\mu}{\rho}$ is introduced. For convenience, the Navier Stokes equations is written in their different components

$$\frac{\partial u_i}{\partial t} + u_j \frac{\partial u_i}{\partial x_j} = -\delta_{i3} g + \varepsilon_{ij3} f_c u_j - \frac{1}{\rho} \frac{\partial p}{\partial x_i} + \nu \frac{\partial^2 u_i}{\partial x_j^2}. \quad (2.10)$$

2. Turbulent Flows in the Atmosphere

The second term can be written as

$$u_j \frac{\partial u_i}{\partial x_j} = \frac{\partial (u_j u_i)}{\partial x_j} - \underbrace{u_i \frac{\partial u_j}{\partial x_j}}_{=0} \quad (2.11)$$

This leads to a form of the Navier-Stokes equations needed in Section 2.4:

$$\frac{\partial u_i}{\partial t} + \frac{\partial (u_j u_i)}{\partial x_j} = -\delta_{i3}g + \varepsilon_{ij3}f_c u_j - \frac{1}{\rho} \frac{\partial p}{\partial x_i} + \nu \frac{\partial^2 u_i}{\partial x_j^2}. \quad (2.12)$$

2.1.3 Conservation of Moisture

Moisture is an important quantity in the atmosphere. The temporal changes of moisture in the atmosphere can be attributed firstly to the advection by wind and molecular diffusion and secondly to the moisture sources and sinks. This can be expressed as

$$\frac{\partial q}{\partial t} + u_j \frac{\partial q}{\partial x_j} = \nu_q \frac{\partial^2 q}{\partial x_j^2} + \frac{S_q}{\rho_{\text{air}}}, \quad (2.13)$$

where q is the specific humidity of air and ν_q is the molecular diffusivity for water vapor.

2.1.4 First Law of Thermodynamics

The First Law of Thermodynamics is the law of energy conservation, which states that the change of energy E can be done via work $dW = -pdV$ or heat transfer dQ

$$dE = -pdV + dQ. \quad (2.14)$$

Here p is pressure and V is volume. With the specific heat capacity at constant volume and the temperature T , the entropy S and the mass m

$$c_v = \frac{T}{m} \left(\frac{\partial S}{\partial T} \right)_v = \frac{1}{m} \left(\frac{\partial E}{\partial T} \right)_v, \quad (2.15)$$

it follows that

$$mc_v dT = -pdV + dQ \quad (2.16)$$

$$c_v dT = -pd\alpha + d\tilde{Q}, \quad (2.17)$$

with $\alpha = V/m = 1/\rho$ the specific volume and $\tilde{Q} = Q/m$ the heat transfer per mass. After taking the derivative with respect to time it follows that

$$c_v \frac{dT}{dt} = -p \frac{d\alpha}{dt} + \frac{d\tilde{Q}}{dt}. \quad (2.18)$$

2.1.5 Equation of State

Temperature and pressure variations are related via the equation of state. If air is assumed to act like an ideal gas, that is the individual gas molecules can be seen as point particles with weak or no interactions between each other, then the ideal gas law is

$$pV = Nk_B T = nN_A k_B T = nRT, \quad (2.19)$$

with N being the number of gas particles, $k_B = 1.38 \cdot 10^{-23}$ J/K the Boltzmann constant, $N_A = 6.02 \cdot 10^{23}$ 1/mol the Avogadro number and $R = N_A k_B = 8.31$ J/molK the ideal gas constant. If one writes in Equation (2.19) for $n = \frac{m}{M}$, with m being the mass of the particles in kg and M the molecular mass in kg/mol, then Equation (2.19) becomes

$$pV = \frac{m}{M} RT = mR_M T \Leftrightarrow p = \frac{m}{V} R_M T = \rho R_M T, \quad (2.20)$$

where R_M is the specific gas constant of air.

2.1.6 Reynolds Averaging

In atmospheric models, the Equations (2.2), (2.12), (2.13), (2.18) together with Equation (2.20), form a complete set of equations for the variables ρ , \mathbf{u} , T , q and p . These equations are difficult to solve analytically and are commonly solved numerically. For Reynolds averaged atmospheric models, physical variables are decomposed into a mean part and turbulent perturbations. The following averaging rules are valid for general variables $A = \bar{A} + a'$ and $B = \bar{B} + b'$

$$\overline{(A + B)} = \bar{A} + \bar{B} \quad (2.21)$$

2. Turbulent Flows in the Atmosphere

$$\overline{\overline{A}} = \overline{A} \quad (2.22)$$

$$\overline{\overline{AB}} = \overline{AB} \quad (2.23)$$

$$\overline{\frac{dA}{dt}} = \frac{d\overline{A}}{dt} \quad (2.24)$$

From rules (2.21) to (2.24) it can be obtained that

$$\overline{a'} = 0 \quad (2.25)$$

$$\overline{\overline{Ba'}} = 0 \quad (2.26)$$

$$\overline{AB} = \overline{AB} + \overline{a'b'}. \quad (2.27)$$

Terms like $\overline{a'b'}$, $\overline{a'^2}$, $\overline{a'b'^2}$ and $\overline{a'^2b'^2}$ are not necessarily zero. In the following, the process of Reynolds averaging is demonstrated by filtering the Navier-Stokes Equations (2.12). It can be similarly applied for Equations (2.2), (2.13), (2.18) and (2.20). The decomposition for velocity can be written

$$u_i = \overline{u}_i + u'_i, \quad (2.28)$$

where \overline{u}_i is the mean part of the velocity and u'_i is the turbulent part. In addition to u_i , the decomposition is done for the variables $\rho = \overline{\rho} + \rho'$ and $p = \overline{p} + p'$. Also the Boussinesq approximation is applied, that is the assumption $\rho' \ll \overline{\rho}$ is made, if it is not related to g . With this it follows from Equation (2.12)

$$\begin{aligned} & \frac{\partial (\overline{u}_i + u'_i)}{\partial t} + (\overline{u}_j + u'_j) \frac{\partial (\overline{u}_i + u'_i)}{\partial x_j} \\ &= -\delta_{i3}g + \varepsilon_{ij3}f_c (\overline{u}_j + u'_j) - \frac{1}{\overline{\rho}} \frac{\partial (\overline{p} + p')}{\partial x_i} + \nu \frac{\partial^2 (\overline{u}_i + u'_i)}{\partial x_j^2}. \end{aligned} \quad (2.29)$$

Arranging the terms and averaging the whole equation lead to

$$\overline{\frac{\partial \overline{u}_i}{\partial t}} + \underbrace{\overline{\frac{\partial u'_i}{\partial t}}}_{=0} + \overline{u'_j} \frac{\partial \overline{u}_i}{\partial x_j} + \underbrace{\overline{u_j} \frac{\partial u'_i}{\partial x_j}}_{=0} + \underbrace{u'_j \frac{\partial \overline{u}_i}{\partial x_j}}_{=0} + \overline{u'_j \frac{\partial u'_i}{\partial x_j}}$$

2.1. Governing Equations

$$= -\overline{\delta_{i3}g} + \overline{\varepsilon_{ij3}f_c\bar{u}_j} + \underbrace{\overline{\varepsilon_{ij3}f_c u'_j}}_{=0} - \frac{1}{\bar{\rho}} \frac{\partial \bar{p}}{\partial x_i} + \underbrace{\frac{1}{\bar{\rho}} \frac{\partial p'}{\partial x_i}}_{=0} + \nu \frac{\partial^2 \bar{u}_i}{\partial x_j^2} + \nu \underbrace{\frac{\partial^2 u'_i}{\partial x_j^2}}_{=0}. \quad (2.30)$$

The result is

$$\frac{\partial \bar{u}_i}{\partial t} + \bar{u}_j \frac{\partial \bar{u}_i}{\partial x_j} + \overline{u'_j \frac{\partial u'_i}{\partial x_j}} = -\delta_{i3}g + \varepsilon_{ij3}f_c\bar{u}_j - \frac{1}{\bar{\rho}} \frac{\partial \bar{p}}{\partial x_i} + \nu \frac{\partial^2 \bar{u}_i}{\partial x_j^2}. \quad (2.31)$$

Adding to the third term $\overline{u'_i \frac{\partial u'_j}{\partial x_j}} = 0$ for an incompressible fluid and write this term in the following form

$$\overline{u'_j \frac{\partial u'_i}{\partial x_j}} + \overline{u'_i \frac{\partial u'_j}{\partial x_j}} = \frac{\partial(\overline{u'_j u'_i})}{\partial x_j}. \quad (2.32)$$

and obtain the Reynold averaged Navier-Stokes equations in flux form

$$\frac{\partial \bar{u}_i}{\partial t} + \bar{u}_j \frac{\partial \bar{u}_i}{\partial x_j} + \frac{\partial(\overline{u'_j u'_i})}{\partial x_j} = -\delta_{i3}g + \varepsilon_{ij3}f_c\bar{u}_j - \frac{1}{\bar{\rho}} \frac{\partial \bar{p}}{\partial x_i} + \nu \frac{\partial^2 \bar{u}_i}{\partial x_j^2}. \quad (2.33)$$

By moving the third term to the right hand side, it follows

$$\underbrace{\frac{\partial \bar{u}_i}{\partial t}}_I + \underbrace{\bar{u}_j \frac{\partial \bar{u}_i}{\partial x_j}}_{II} = -\underbrace{\delta_{i3}g}_{III} + \underbrace{\varepsilon_{ij3}f_c\bar{u}_j}_{IV} - \underbrace{\frac{1}{\bar{\rho}} \frac{\partial \bar{p}}{\partial x_i}}_V + \nu \underbrace{\frac{\partial^2 \bar{u}_i}{\partial x_j^2}}_{VI} - \underbrace{\frac{\partial(\overline{u'_j u'_i})}{\partial x_j}}_{VII}. \quad (2.34)$$

Equation (2.34) is similar to Equation (2.12), except for the turbulent terms at the end. The meanings of the different terms are as follows:

- Term I represents the storage of mean momentum;
- Term II describes the advection of mean momentum by the mean wind;
- Term III shows that gravitation acts only in the vertical direction;
- Term IV describes the Coriolis force;
- Term V represents the pressure gradient force;
- Term VI represents the influence of viscous stress on the mean motion;
- Term VII represents the influence of Reynolds' stress on the mean motion.

2. Turbulent Flows in the Atmosphere

Term VII can also be written as

$$\frac{\partial(\overline{u'_j u'_i})}{\partial x_j} = \frac{1}{\rho} \frac{\partial \tau_{ij}}{\partial x_j} \quad (2.35)$$

where $\tau_{ij} = -\overline{\rho u'_i u'_j}$ is the Reynolds' stress tensor.

Equation (2.34) is the equation for the mean velocity, but it is not closed because the Reynolds shear stress terms, $\overline{u'_j u'_i}$, are unknown. In other words, to forecast the behavior of the mean velocity, knowledge on turbulence is needed. This leads to the closure problem.

2.2 The Closure Problem

As a result of Reynolds averaging applied to the Equations (2.2), (2.13), (2.18) and (2.20), the mean quantities now depend on the correlations (or the second statistical moment) of the turbulent components, e.g., $\overline{u'_i u'_j}$. In principle, it is possible to derive the equations for the correlations, but they again contain higher order moments $\overline{u'_i u'_j u'_k}$. The number of unknowns grows faster than the number of equations, as Table 2.1 illustrates. The order of the moment for which a prognostic

Table 2.1: Example showing a tally of equations and unknowns for various statistical moments, demonstrating the closure problem for turbulent flow. The full set of equations includes even more unknowns. Taken from *Stull* [1988]

Prognostic Eq. for:	Moment	Equation	Number of Equations	Number of Unknowns
$\overline{u_i}$	First	$\frac{\partial \overline{u_i}}{\partial t} = \dots - \frac{\partial(\overline{u'_i u'_j})}{\partial x_j}$	3	6
$\overline{u'_i u'_j}$	Second	$\frac{\partial \overline{u'_i u'_j}}{\partial t} = \dots - \frac{\partial(\overline{u'_i u'_j u'_k})}{\partial x_k}$	6	10
$\overline{u'_i u'_j u'_k}$	Third	$\frac{\partial \overline{u'_i u'_j u'_k}}{\partial t} = \dots - \frac{\partial(\overline{u'_i u'_j u'_k u'_m})}{\partial x_m}$	10	15

equation is established gives the order of the closure. From Table 2.1 it can be

seen, that the number of unknowns is larger than the number of equations for each order of closure. In order to solve the closure problem, several techniques have been proposed. One simple approach of a first order closure scheme is the K-theory, in which the fluxes of a variable ξ are parametrized via the gradient of ξ times a parameter K , that is

$$\overline{u'_j \xi'} = -K \frac{\partial \bar{\xi}}{\partial x_j}, \quad (2.36)$$

ξ stands for any physical variable, like u , T or q . K is the exchange coefficient. For atmospheric surface-layer flow simulations, K can be estimated using the Monin-Obukhov similarity theory (MOST). In order to understand the difference between most weather models and the LES model used in the present study it is necessary to understand MOST, which is explained in the following section.

2.3 Monin-Obukhov Similarity Theory

Monin and Obukhov [1954] analyzed the processes of turbulent mixing in the atmospheric surface layer using the theory of similarity. The starting point is the Reynolds averaged Navier-Stokes Equations (2.34):

$$\frac{\partial \bar{u}_i}{\partial t} + \frac{\bar{u}_j \partial \bar{u}_i}{\partial x_j} = -\delta_{i3} g + \varepsilon_{ij3} f_c \bar{u}_j - \frac{1}{\bar{\rho}} \frac{\partial \bar{p}}{\partial x_i} + \nu \frac{\partial^2 \bar{u}_i}{\partial x_j^2} - \frac{\partial (\overline{u'_j u'_i})}{\partial x_j}. \quad (2.37)$$

To this equation, the following assumptions are made

- The flow is stationary: $\frac{\partial \bar{u}_i}{\partial t} = 0$.
- The flow is horizontally homogeneous: $\frac{\partial \bar{u}_j}{\partial x_j} = 0$, except for $j = 3$.
- The mean vertical velocity is zero: $\bar{u}_3 = \bar{w} = 0$, therefore $\bar{u}_j \frac{\partial \bar{u}_j}{\partial x_j} = 0$.
- The Coriolis force can be neglected: $f_c = 0$.
- The horizontal pressure gradient can be neglected: $\frac{\partial \bar{p}}{\partial x_1} = \frac{\partial \bar{p}}{\partial x_2} = 0$.
- The viscous friction can be neglected: $\nu \frac{\partial^2 \bar{u}_i}{\partial x_j^2} = 0$

2. Turbulent Flows in the Atmosphere

- The turbulent momentum flux is horizontally homogeneous: $\frac{\partial(\overline{u'_j u'_i})}{\partial x_j} = 0$, except for $j = 3$.
- The flow is aligned to the x_1 direction.

With these assumptions, Equations (2.37) are reduced to

$$\frac{\partial \overline{u'w'}}{\partial z} = 0. \quad (2.38)$$

or

$$-\overline{u'w'} = \text{const.} \quad (2.39)$$

In other words, the momentum flux in the vertical direction

$$\frac{\tau}{\rho} = -\overline{u'w'} \quad (2.40)$$

is vertically constant.

Following *Monin and Obukhov* [1954], the logarithmic wind profile can be derived based on similarity arguments.

The dynamic (or friction) velocity, u_* , is defined as

$$u_*^2 = \tau / \bar{\rho}. \quad (2.41)$$

Monin and Obukhov [1954] used the fact, that the dynamic velocity (as a statistical moment) is invariant under the similarity transformations

$$x' = kx, \quad y' = ky, \quad z' = kz \quad t' = kt. \quad (2.42)$$

In the stationary regime, they investigated the behavior of the ratio

$$\frac{\bar{u}(z_2) - \bar{u}(z_1)}{u_*} = f\left(\frac{z_2}{z_1}\right). \quad (2.43)$$

Corresponding to the ratio of the velocities, the function f is a non-dimensional quantity. Due to the assumption of self-similarity f is a function only depending

2.3. Monin-Obukhov Similarity Theory

of the ratio z_2/z_1 . The function can be determined in the following way. Assume $z_3 > z_2 > z_1$. Then

$$\begin{aligned} f\left(\frac{z_2}{z_1}\right) + f\left(\frac{z_3}{z_2}\right) &= \frac{\overline{u}(z_2) - \overline{u}(z_1) + \overline{u}(z_3) - \overline{u}(z_2)}{u_*} = \frac{\overline{u}(z_3) - \overline{u}(z_1)}{u_*} \\ &= f\left(\frac{z_3}{z_1}\right) = f\left(\frac{z_3}{z_2} \frac{z_2}{z_1}\right). \end{aligned} \quad (2.44)$$

With $\zeta_1 = z_2/z_1$ and $\zeta_2 = z_3/z_2$, Equation (2.44) can be written as

$$f(\zeta_1 \zeta_2) = f(\zeta_1) + f(\zeta_2). \quad (2.45)$$

Equation (2.45) has the solution

$$f(\zeta) = C \ln \zeta. \quad (2.46)$$

Assuming $C = 1/\kappa$, with κ being the Karman constant, then from Equation (2.43) it follows

$$\frac{\overline{u}(z_2) - \overline{u}(z_1)}{u_*} = \frac{1}{\kappa} \ln \frac{z_2}{z_1}. \quad (2.47)$$

Equation (2.47) can be written as

$$\overline{u}(z_2) - \overline{u}(z_1) = \frac{u_*}{\kappa} \ln \frac{z_2}{z_1}. \quad (2.48)$$

Equation (2.48) can be integrated between the heights z_1 and z_2

$$\int_{z_1}^{z_2} \frac{d\overline{u}}{dz} dz = \frac{u_*}{\kappa} \int_{z_1}^{z_2} \frac{1}{z} dz. \quad (2.49)$$

When examining infinitesimal close values z_1 and z_2 , that means $|z_2 - z_1| < \varepsilon$, $\varepsilon > 0$, it follows from Equation (2.49)

$$\frac{d\overline{u}}{dz} = \frac{u_*}{\kappa z}. \quad (2.50)$$

2. Turbulent Flows in the Atmosphere

Monin and Obukhov [1954] introduced a length scale L

$$L = -\frac{u_*^3}{\kappa \frac{g}{T} \frac{q}{c_p \bar{\rho}}} \quad (2.51)$$

and a temperature T_*

$$T_* = -\frac{1}{\kappa u_*} \frac{q}{c_p \bar{\rho}}. \quad (2.52)$$

The minus sign and the Karman constant are introduced due to convention. The signs of L and T_* are determined by the kind of stratification. *Monin and Obukhov* [1954] investigated the non-dimensional magnitudes

$$\frac{\kappa z}{u_*} \frac{d\bar{u}}{dz} \quad (2.53)$$

and

$$\frac{z}{T_*} \frac{d\bar{T}}{dz} \quad (2.54)$$

They stated that these non-dimensional characteristics should be functions of external parameters and of z . From Equations (2.53) and (2.54) follows

$$\frac{\kappa z}{u_*} \frac{d\bar{u}}{dz} = \varphi_m \left(\frac{z}{L} \right) \quad (2.55)$$

and

$$\frac{z}{T_*} \frac{d\bar{T}}{dz} = \varphi_h \left(\frac{z}{L} \right), \quad (2.56)$$

where φ_m is the stability function of momentum and φ_h is the stability function of heat. Equations (2.55) and (2.56) can be written as

$$\frac{d\bar{u}}{dz} = \frac{u_*}{\kappa z} \varphi_m \left(\frac{z}{L} \right) \quad (2.57)$$

and

$$\frac{d\bar{T}}{dz} = \frac{T_*}{z} \varphi_h \left(\frac{z}{L} \right). \quad (2.58)$$

The K-Theory (Equation (2.36)) represents a connection between the flux and the gradient:

$$-u_*^2 = \overline{u'w'} = -K_m \frac{d\bar{u}}{dz}. \quad (2.59)$$

Where K_m stands for the exchange coefficient for momentum. By inserting Equation (2.57) in Equation (2.59) it follows

$$u_*^2 = K_m \frac{d\bar{u}}{dz} = K_m \frac{u_*}{\kappa z} \varphi_m \left(\frac{z}{L} \right). \quad (2.60)$$

From which the coefficient K_m is calculated as

$$K_m = \frac{\kappa u_* z}{\varphi_m \left(\frac{z}{L} \right)}. \quad (2.61)$$

Similarly, for Equations (2.36) and (2.58), it follows

$$\frac{q}{c_p \bar{\rho}} = \overline{T'w'} = -K_h \frac{d\bar{T}}{dz} = K_h \frac{T_*}{z} \varphi_h \left(\frac{z}{L} \right). \quad (2.62)$$

The exchange coefficient for heat K_h is

$$K_h = \frac{qz}{c_p \bar{\rho} T_* \varphi_h \left(\frac{z}{L} \right)} \quad (2.63)$$

together with Equation (2.52) it follows

$$K_h = \frac{qz}{c_p \bar{\rho} q \varphi_h \left(\frac{z}{L} \right)} = \frac{\kappa u_* z}{\varphi_h \left(\frac{z}{L} \right)}. \quad (2.64)$$

With this knowledge, it is possible to understand the LES used in the thesis and explained in the next section.

2.4 Large-Eddy Simulation

Large eddies are the main contributors to the transfer processes in the atmospheric boundary layer. LES models were invented in the 1960s (*Smagorinsky* [1963]), and substantially developed in the 1970s and 1980s (*Deardorff* [1970]; *Moeng*

2. Turbulent Flows in the Atmosphere

[1984]). Today, LES models are well established for the simulation of turbulent flows in the atmosphere (*Sullivan et al.* [1998]; *Beare et al.* [2006]; *Kleissl et al.* [2006]; *Kumar et al.* [2006]).

2.4.1 LES Filtering

In LES models, the equation system is filtered into a grid-resolved part and a subgrid part. The large eddies lie on the grid-resolved part and the small eddies lie on the subgrid part (*Leonard* [1975]; *Moeng* [1984]). The filtering is done via the convolution with a filter function $G(\mathbf{x})$

$$\langle u_i \rangle(\mathbf{x}) = \int G_i(\mathbf{x}) u_i(\mathbf{x} - \mathbf{r}) d\mathbf{r}, \quad (2.65)$$

where u_i stands for the different components of the velocity. For the filtering, many functions can be chosen, for example Gaussian or box filters. Following *Pope* [2000] the residual field can be written as

$$u'_i = u_i - \langle u_i \rangle. \quad (2.66)$$

Therefore, the LES decomposition is

$$u_i = \langle u_i \rangle + u'_i. \quad (2.67)$$

This decomposition appears similar to the Reynolds decomposition, but is different in that

$$\langle u'_i \rangle \neq 0. \quad (2.68)$$

Applying the LES filtering to the Navier-Stokes equations (Equation 2.12) leads to

$$\frac{\partial \langle u_i \rangle}{\partial t} + \frac{\partial \langle u_i \rangle \langle u_j \rangle}{\partial x_j} = -\delta_{i3} g + \varepsilon_{ij3} f_c \langle u_j \rangle - \frac{1}{\rho} \frac{\partial \langle p \rangle}{\partial x_i} - \frac{\partial \tau_{ij}}{\partial x_j} + \nu \frac{\partial^2 \langle u_i \rangle}{\partial x_j^2}, \quad (2.69)$$

where

$$\tau_{ij} = \langle u_i u_j \rangle - \langle u_i \rangle \langle u_j \rangle \quad (2.70)$$

is the subgrid stress. In order to solve Equation (2.69), a closure for the subgrid stress is again needed. Several subgrid closures are available. One is the Smagorinsky closure (*Smagorinsky* [1963]), in which the subgrid stress tensor is parametrized as follows

$$\tau_{ij} = -2K_{sm}\langle S_{ij} \rangle, \quad (2.71)$$

where the $\langle S_{ij} \rangle$ is the rate of strain tensor

$$\langle S_{ij} \rangle = \frac{1}{2} \left(\frac{\partial \langle u_i \rangle}{\partial x_j} + \frac{\partial \langle u_j \rangle}{\partial x_i} \right) \quad (2.72)$$

and

$$K_{sm} = (C_s \Delta_c)^2 \sqrt{2\langle S_{ij} \rangle \langle S_{ij} \rangle} \quad (2.73)$$

is the subgrid eddy viscosity. The parameter C_s depends on the filter width Δ_c which is often chosen to be the model resolution. In this case, C_s is usually set to $C_s \approx 0.17$.

Another widely used closure is the $k-l$ model (*Deardorff* [1980]). In this closure, the subgrid fluxes are parametrized by

$$\tau_{ij} = K_m \left(\frac{\partial \langle u_i \rangle}{\partial x_j} + \frac{\partial \langle u_j \rangle}{\partial x_i} \right), \quad (2.74)$$

with

$$K_m = C_k l \sqrt{e}, \quad (2.75)$$

where e is the subgrid turbulent kinetic energy, l is the mixing length and C_k is an empirical constant $C_k = 0.15$ (*Shao et al.* [2013]). If the mixing length is set corresponding to the model resolution, so that $l_x = \Delta x$ and $l_z = \Delta z$, then the subgrid eddy diffusivity for a scalar $K_{h,sg}$ can be expressed as

$$K_{h,sg} = \frac{K_{m,sg}}{P_r}, \quad (2.76)$$

where $P_r \approx 0.3$ is the Prandtl number.

2. Turbulent Flows in the Atmosphere

2.4.2 LES-ALM

Equation (2.69) is the starting point for the development of the LES model of *Shao et al.* [2013]. The underlying weather model is the WRF model (*Skamarock et al.* [2008]). The used land-surface scheme is based on the NOAH community land-surface model (*Chen and Dudhia* [2001]), where NOAH stands for the four involved collaborators: National Centers for Environmental Prediction (NCEP), Oregon State University, Air Force, Hydrologic Research Lab. *Shao et al.* [2013] made three modifications to the model, and called the modified model a Large-Eddy Simulation Atmosphere-Land-surface Model (LES-ALM). In the following, the paper by *Shao et al.* [2013] is summarized and their modifications are outlined.

Shao et al. [2013] first adopted the idea of *Shaw and Schumann* [1992] and treated vegetation as momentum sinks in the equations of motion. They added a term for the canopy drag

$$S_{Mi} = -\alpha_f C_d V \langle u_i \rangle \quad (2.77)$$

to Equation (2.69). The variables in Equation (2.77) are $C_d = 0.15$ the dimensionless drag coefficient (*Shaw et al.* [1988]), V is the local wind speed and α_f is the vegetation frontal area index. The final equation of motion reads as

$$\frac{\partial \langle u_i \rangle}{\partial t} + \frac{\partial \langle u_i \rangle \langle u_j \rangle}{\partial x_j} = -\delta_{i3} g + \varepsilon_{ij3} f_c \langle u_j \rangle - \frac{1}{\rho} \frac{\partial \langle p \rangle}{\partial x_i} - \frac{\partial \tau_{ij}}{\partial x_j} + \nu \frac{\partial^2 \langle u_i \rangle}{\partial x_j^2} + S_{Mi}. \quad (2.78)$$

In a similar way as for momentum, the vegetation also acts as sources or sinks for heat. The source term can be added to the temperature equation (Equation (2.18)) through

$$S_T = -\alpha_t C_T V (\bar{T} - T_c). \quad (2.79)$$

In Equation (2.79), the quantities are the leaf area density α_f , the dimensionless exchange coefficient C_t , the air temperature \bar{T} and the canopy temperature T_c .

In addition, the vegetation acts also as a source for moisture. The source term

can be expressed as

$$S_q = - (1 - f_{\text{wet}}) \frac{\alpha_t}{2} C_q [\bar{q} - q_s(T_c)] - f_{\text{wet}} \frac{\alpha_t}{2} C_d V [\bar{q} - q_s(T_c)], \quad (2.80)$$

where f_{wet} is the fraction of wet vegetation, \bar{q} the specific humidity and $q_s(T_c)$ is the saturation specific humidity at canopy temperature T_c . This source term can be added to the moisture equation (Equation (2.18)).

Shao et al. [2013] concluded from Equation (2.79) and (2.80) that a scheme for the canopy temperature is needed. In the following, a brief discussion of the idea of their scheme is presented. They stated that the canopy temperature is determined by

$$\alpha_t \varepsilon \sigma T_c^4 = k_s R_s + k_l R_l - \rho c_p S_T - \rho L S_q, \quad (2.81)$$

where ε is the vegetation emissivity, σ is the Stefan-Boltzmann constant, k_s , k_l are canopy extinction coefficients for short-wave net radiation flux R_s , and long-wave net radiation flux R_l , respectively. ρ is the air density, c_p is the air specific heat at constant pressure and L is the latent heat of vaporization of water. Their idea was that they expressed the short-wave radiation through the vegetation canopy by dividing the vegetation into bins of size δz .

In order to explain the second modification made by *Shao et al.* [2013], first the parametrization of the sensible heat in usual LES models is shown. The sensible heat flux $H = c_p \overline{\rho w' T'}$ can be parametrized via Equation (2.36):

$$H = \rho c_p K_h \frac{\partial \bar{T}}{\partial z} \quad (2.82)$$

The eddy diffusivity K_h can be derived from MOST (Equation 2.64) as

$$K_h = \frac{\kappa u_* z}{\varphi_h}, \quad (2.83)$$

with κ , u_* and φ_h defined as in Section 2.3.

2. Turbulent Flows in the Atmosphere

The sensible heat flux can also be expressed by

$$H = -\rho c_p \frac{\bar{T}_a - \bar{T}_0}{r_h}, \quad (2.84)$$

with \bar{T}_a being the reference-level air temperature and \bar{T}_0 the surface temperature. The aerodynamic resistance r_h is related to the eddy diffusivity as follows

$$r_h = \int_{z_0}^z \frac{1}{K_h} dz'. \quad (2.85)$$

Since K_h is known from MOST (cf. Equation (2.83)), an integration can be done which gives

$$r_h = \frac{1}{\kappa u_*} \left\{ \ln \left(\frac{z}{z_{0h}} \right) - \int_{z_{0h}}^z \left[1 - \varphi_h \left(\frac{z'}{L_0} \right) \right] d \ln z' \right\}. \quad (2.86)$$

z_{0h} stands for the roughness length for heat and L_0 is the Obukhov length. This flux formulation is used in large-eddy atmosphere and land-surface coupled simulations. However, *Shao et al.* [2013] emphasized four points, why this flux formulation is questionable:

1. The derivation of MOST assumes horizontal homogeneity with the effect of advection being negligible. These assumptions do not hold on the scale of atmospheric large eddies.
2. The MOST similarity functions are empirically derived using averaged boundary-layer measurements.
3. In the framework of an LES model, the MOST-based diffusivity and viscosity estimates near the surface are inconsistent with the model closure-based diffusivity and viscosity estimates, causing contradictions between model closure and boundary condition.
4. Even if MOST were applicable, the similarity parameters could not be specified with confidence, especially in areas of land-surface heterogeneity, causing large uncertainties in flux estimates.

Especially point (1) is the reason why LES-ALM is used in the present thesis, since the flux formulation in LES-ALM does not rely on MOST and therefore not on spatial homogeneity.

In the following, an outline of the LES-ALM flux formulation is given. In LES-ALM, the fluxes are expressed through a grid-resolved flux and a subgrid flux. That means for the sensible heat flux H

$$H = H_g + H_{sg}, \quad (2.87)$$

and for the latent heat flux LE

$$LE = LE_g + LE_{sg}. \quad (2.88)$$

The grid-resolved fluxes can be computed as

$$H_g = \rho c_p \tilde{w} \tilde{T} \quad (2.89)$$

and

$$LE_g = \rho L \tilde{w} \tilde{q}. \quad (2.90)$$

Where \tilde{w} and \tilde{T} are the grid-resolved vertical velocity and air temperature, respectively. The subgrid heat fluxes are calculated as

$$H_{sg} = -\rho c_p \frac{\tilde{T}_a - \tilde{T}_0}{r_{h,sg}} \quad (2.91)$$

and

$$LE_{sg} = -\rho L \beta \frac{\tilde{q}_a - \tilde{q}_s(\tilde{T}_0)}{r_{q,sg}}, \quad (2.92)$$

where \tilde{T}_a and \tilde{q}_a are the air temperature and specific humidity at the lowest model level. The variable \tilde{T}_0 is the surface skin temperature and $\tilde{q}_s(\tilde{T}_0)$ is the saturation specific humidity at \tilde{T}_0 . β is usually assumed to be a linear function of the soil moisture in the top soil layer (*Irannejad and Shao [1998]*). For simplicity it is assumed that $r_{h,sg} = r_{q,sg}$. The main point is now that these resistances cannot be

2. Turbulent Flows in the Atmosphere

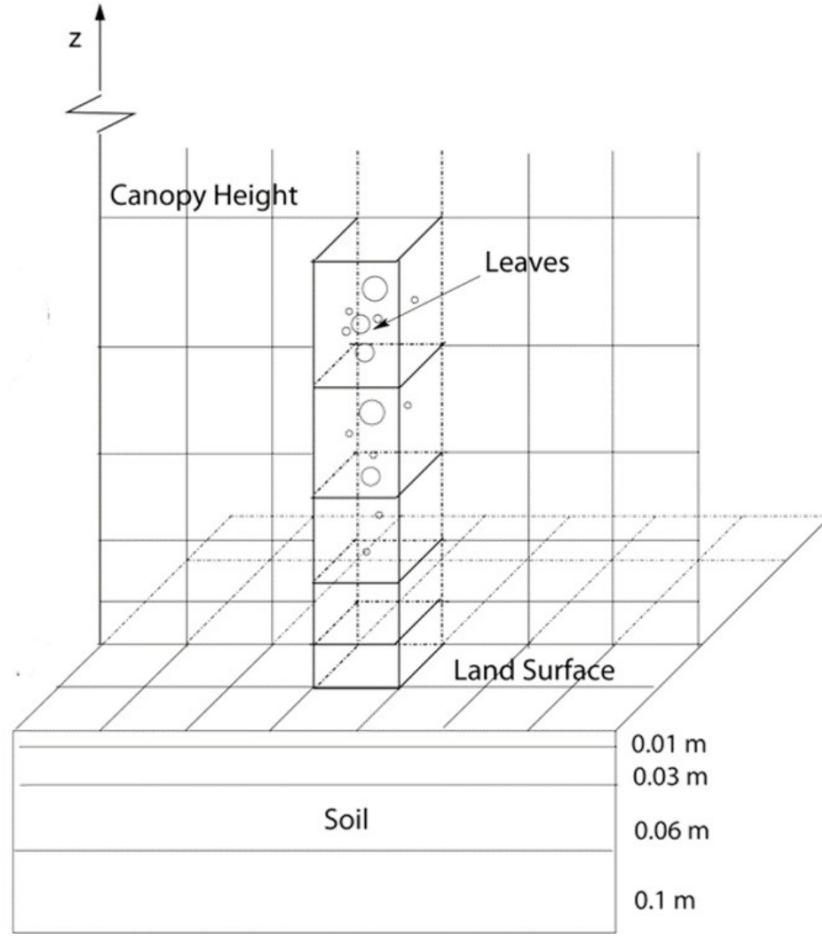


Figure 2.1: LES-ALM configuration. The vegetation canopy is vertically resolved in multiple layers and thin soil layers are used to allow the land surface to respond on the large-eddy time scale. Taken from *Shao et al.* [2013].

obtained by MOST. Instead, the resistances are calculated as the integral over the reciprocal eddy diffusivity

$$r_{h,sg} = \int_{z_{0s}}^{z_1} K_{h,sg}^{-1}(z) dz, \quad (2.93)$$

where z_{0s} is the roughness length which depends on the land use type. z_1 is the lowest model level height. It is assumed that the eddy diffusivity scales with the height z as

$$K_{h,sg}(z) = K_{h,sg}(z_1) \left(\frac{z}{z_1} \right)^n. \quad (2.94)$$

The eddy diffusivity at the lowest model level height $K_{h,sg}(z_1)$ is estimated from the subgrid closure scheme (Equation (2.76)). The integration of Equation (2.94) together with Equation (2.93) gives

$$r_{h,sg} = \frac{z_1}{K_{h,sg}(z_1)} \left[\ln \left(\frac{z_1}{z_{0s}} \right) \right], \quad (2.95)$$

for $n = 1$. For $n > 1$ the integration gives

$$r_{h,sg} = \frac{z_1}{(1-n)K_{h,sg}(z_1)} \left[1 - \left(\frac{z_1}{z_{0s}} \right)^{n-1} \right]. \quad (2.96)$$

Shao et al. [2013] summarized that their flux calculation differs from that of a conventional land-surface scheme in the following three points

1. The main components of the fluxes are grid-resolved.
2. The parametrization of the subgrid components are in consistency with the flow subgrid closure.
3. The computation of the fluxes does not rely on MOST.

However, *Shao et al.* [2013] stated that the validity of the scaling behavior of $K_{h,sg}$ (Equation (2.94)) has to be analyzed further.

The third modification which was made to the model by *Shao et al.* [2013], was to choose an appropriate soil-layer configuration. They stated that to allow land surface to respond to the effects of large-eddies, the thickness of the soil layer Δs should be corresponding to the typical atmospheric time scales t_A and the soil thermal diffusivity ν_G , as follows

$$\Delta s \sim \sqrt{\nu_G t_A}. \quad (2.97)$$

For $t_A = 1$ day, Δs should be approximately 0.2 m. For a shorter time $t_A = 10$ min, Δs should be approximately 0.01 m. The soil-layer configuration as well as a sketch of the canopy temperature scheme is shown in Figure 2.1.

2. Turbulent Flows in the Atmosphere

2.4.3 Performance of the LES-ALM

Shao et al. [2013] compared the model output of the LES-ALM with measurements. These measurements were obtained from the Transregional Collaborative Research Centre 32 "Patterns in Soil-Vegetation-Atmosphere-Systems: Monitoring, Modelling and Data Assimilation" (*Vereecken et al.* [2010]). The data in the present thesis is also partly based on these measurements (cf. Section 4.2 for more details). For the comparison measurements from two fields (sugar beet and harvested winter wheat) were used. In the following only one example of their comparison is shown. Figure 2.2 shows the comparison of the simulated and observed sensible heat and latent heat fluxes for the harvested wheat and the sugar beet surface averaged over a 30 minute interval. The two different experiments

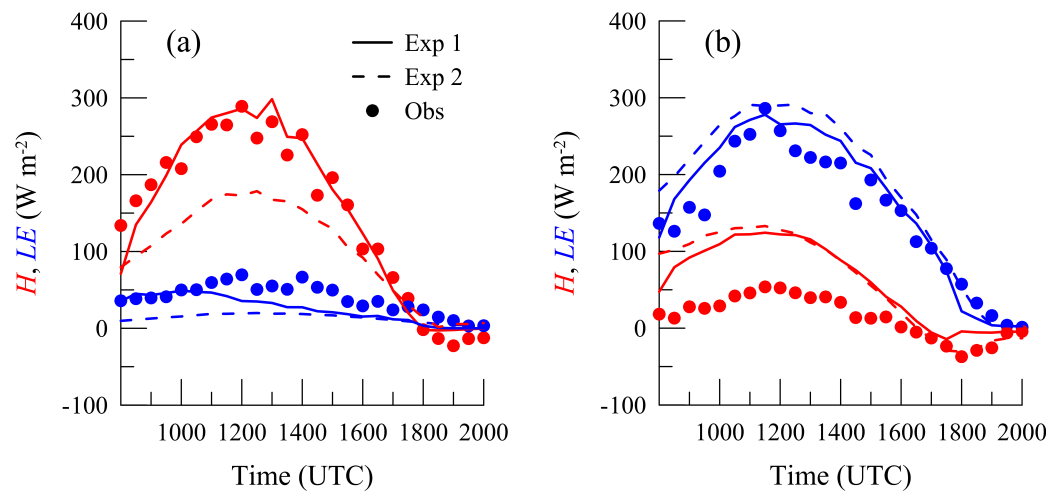


Figure 2.2: Comparison of the LES-ALM with measurements. **(a)** Comparison of the simulated and observed sensible heat (red) and latent heat fluxes (blue) for the harvested wheat surface. **(b)** As (a) but for the sugar beet surface. Experiment 1 is the model setup with the explicit canopy scheme a fine soil layer configuration as shown in Figure 2.1 and the surface layer scheme explained in Section 2.4.2. Experiment 2 is the model setup with with a bulk canopy scheme and 4 soil layers: 0.1, 0.3, 0.6 and 1 m. The surface layer scheme is based on MOST. Obs. stands for the observations. Taken from *Shao et al.* [2013].

refer to the different model setups. Experiment 1 is the model setup with the explicit canopy scheme a fine soil layer configuration as shown in Figure 2.1 and the surface layer scheme explained in Section 2.4.2. Experiment 2 is the model

setup with a bulk canopy scheme, 4 soil layers: 0.1, 0.3, 0.6 and 1 m. The surface layer scheme is based on MOST. *Shao et al.* [2013] obtained from Figure 2.2 that for the harvested wheat surface, the sensible heat flux of the second experiment is underestimated from the late morning to the early afternoon. They concluded that the simulated sensible heat flux of the first experiment agreed much better with the observations. They stated that the latent heat flux of the second experiment over the sugar beet surface is overestimated compared to the measurements. This overestimation has been reduced in the first experiment. For the sugar beet surface, both experiments showed an overestimation of the sensible heat flux. *Shao et al.* [2013] argued that this overestimation is based on setting of the albedo value for the sugar beet surface of 0.22. This value could have been too low. However, *Shao et al.* [2013] concluded that their modifications to the model have improved the model results significantly.

Tests show that LES-ALM is able to investigate the influence of the land-use heterogeneity on the atmospheric boundary layer. As explained in the introduction, to have this kind of high-resolution models is the first step of the investigation. The next step is to define heterogeneity in order to understand its influence on the atmosphere. The next chapter gives a review of existing methods for heterogeneity quantification and introduces the Shannon entropy and the entropy spectrum for the quantification.

2. Turbulent Flows in the Atmosphere

3 Existing Methods for Heterogeneity Quantification

To understand how land-surface heterogeneity influences the atmospheric boundary layer, it is essential to find a quantification for heterogeneity. In the following, a short outline of the traditional approaches to quantifying many important aspects of land-surface heterogeneity is given (*Hintz et al.* [2014]).

The term heterogeneity is used in different scientific fields, and may mean different things. For example, in ecological science, the meaning of heterogeneity is different from the meaning in biology, physics or meteorology. The problem how to quantify heterogeneity is an old one and the literature is very extensive. The way how to deal with the problem of characterizing heterogeneity is very field specific. In most cases the characterization is done regarding to a specific scientific question. To give a comprehensive overview of all methods used for heterogeneity quantification is beyond the scope of the present thesis. Therefore, only the most common methods for the description of two-dimensional heterogeneities are discussed here.

As summarized by *Mölders et al.* [1996] and *Garrigues et al.* [2006, 2007], there are several ways to deal with heterogeneity. One way is, for instance, to average the surface properties (*Lhomme* [1992]; *Dolman* [1992]). This leads to a more homogeneous surface, but tells nothing about how heterogeneous the underlying structure was before averaging. Some researchers understand heterogeneity as the variance of a physical quantity. They obtain the relative variance by normalizing

3. Existing Methods for Heterogeneity Quantification

the variance with the mean. A high relative variance implies a more heterogeneous surface, while a low relative variance implies a more homogeneous one. While relative variance is useful as an integrated statistical quantity, it is insufficient to distinguish the structures of the heterogeneity. That means heterogeneities with the same relative variance can be profoundly different in terms of structure. Alternatively, researchers use spectral and PDF approaches describing surface heterogeneity. The spectral approaches refer to methods that use Fourier transformation and related techniques.

Land-surface heterogeneity can be differentiated with respect to four main aspects: structure, information, anisotropy and contrast. The diversity of the different aspects of heterogeneity makes it difficult to find a single measure, which can describe all aspects. Each of the four categories has influences on the atmospheric motion. The focus of the present thesis is the quantification of the information aspect of heterogeneity. In the following, an outline of the approaches used for quantification, namely, the Taylor diagram, the variogram, the power spectrum and the PDF approach, is given. The last one is important to develop the entropy spectrum method.

3.1 Taylor Diagram

The Taylor diagram groups together several statistical parameters (e.g. correlation coefficient, root mean square error difference and variance) (*Taylor* [2001]) in a single plot. It shows how much structures have in common in terms of their statistics.

Let R be the correlation coefficient function and E' the centered root mean square error difference, defined by

$$R = \frac{1}{N\sigma_f\sigma_r} \sum_{n=1}^N (f_n - \bar{f})(r_n - \bar{r}) \quad (3.1)$$

and

$$E' = \sqrt{\frac{1}{N} \sum_{n=1}^N [(f_n - \bar{f})(r_n - \bar{r})]^2}, \quad (3.2)$$

respectively. In Taylor's notation, f_n is the investigated variable, r_n is the reference variable, \bar{f} and \bar{r} are their mean values and σ_f, σ_r are the standard deviations

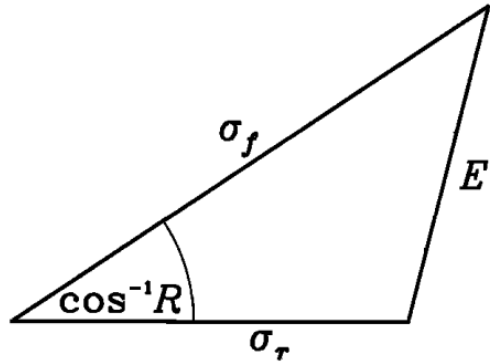


Figure 3.1: Geometric relationship between the correlation coefficient R , the centered root means square error difference E' and the standard deviations σ_f and σ_r . Taken from *Taylor* [2001].

of f and r , respectively. The data set contains N points in time or space. Then, the geometric relationship between R, E', σ_f and σ_r is as follows

$$E'^2 = \sigma_f^2 + \sigma_r^2 - 2\sigma_f\sigma_r R. \quad (3.3)$$

This can be obtained via the law of cosines

$$c^2 = a^2 + b^2 - 2ab \cos \phi. \quad (3.4)$$

The Taylor diagram is then constructed as shown in Figure 3.1. An example is given in Figure 3.2. According to *Taylor* [2001], it is not possible to determine from E' how much of the error comes from the difference in structure and phase or how much error comes from the difference in the amplitude of the variations. From the Taylor diagram it can directly be seen how much two structures have in common, in terms of their statistics. However, for using the Taylor diagram

3. Existing Methods for Heterogeneity Quantification

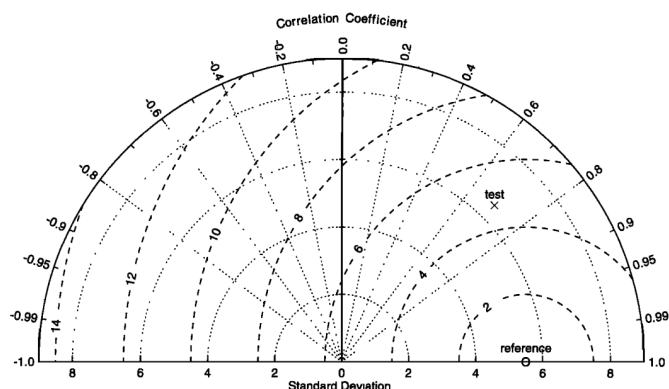


Figure 3.2: Example of a Taylor diagram. The radial distance from the origin is proportional to the standard deviation. The centered RMS error difference between the test and reference field is proportional to their distance apart (in the same units as the standard deviation). The correlation between the two fields is given by the azimuthal position of the test field. Taken from *Taylor* [2001].

for heterogeneity quantification one has to choose a threshold, in order to tell if two structures are significantly different. The Taylor diagram of one of the model results is shown in Section 5.6.

3.2 Variogram

One often-used tool is the variogram γ (or structure function). A variogram describes the difference between the values at the points $Z(x_i + h)$ and $Z(x_i)$ as a function of h

$$\gamma(h) = \frac{1}{2n(h)} \sum_{|x_i - x_j| = h}^{n(h)} [Z(x_i) - Z(x_j)]^2. \quad (3.5)$$

The sum goes over all $n(h)$ pairs of points x_i and x_j at lag distance h . This method has the advantage, that it can describe heterogeneities in terms of spatial correlations at different lag distances. There is a strong connection between variogram and autocorrelation coefficient function R . The larger the autocorrelation coefficient function and the smaller the variogram is, the stronger the correlation between the locations with distance h .

3.3 Power Spectrum

Another often-used method to investigate land-surface heterogeneities is the power spectrum. There are two equivalent definitions of a power spectrum. The first is that it is the magnitude of the Fourier transform of the data, and the second is that it is the Fourier transform of the autocorrelation function.

3.4 Probability Density Function

Another approach is to investigate the PDF, $p(x)$, of surface parameter x , which tells how frequent a certain parameter value occurs. If the range of possible x -values is divided into $m = \frac{x_{max} - x_{min}}{\Delta}$ windows of size Δ , then the probability $p_i = p(x_i) \Delta$ of finding x in bin i is

$$p_i = \frac{n_i}{N}. \quad (3.6)$$

Here, N is the total number of grid cells and n_i the number of cells with x lying in the interval $x_i - \frac{\Delta}{2} < x \leq x_i + \frac{\Delta}{2}$. Therefore, the PDF shows how often a specific value occurs. If the surface parameter consists only of a few values, then the surface is usually more homogeneous. If it consists of many different values the surface is often more heterogeneous. Figure 3.3 shows as an example the albedo patterns of two real land surfaces (cf. Section 4.2 for more details). In Figure 3.3 (a), the pattern is relatively homogeneous compared to the pattern in Figure 3.3 (b). Figure 3.3 (c) and (d) show the corresponding PDFs. The latter has a uniform shape in comparison to the former.

The PDF gives no information on the spatial distribution of the parameters on the surface. To take the spatial distribution into account, it is necessary to find a way to decompose the surface into different parts. Many decomposition methods are available. There are studies which use the Fourier transformation for the decomposition, e.g. *Perron et al.* [2008]. The Fourier transformation has the disadvantage that it changes the prominent features of the heterogeneity. Therefore, the method presented in this study makes use of a more localized transformation,

3. Existing Methods for Heterogeneity Quantification

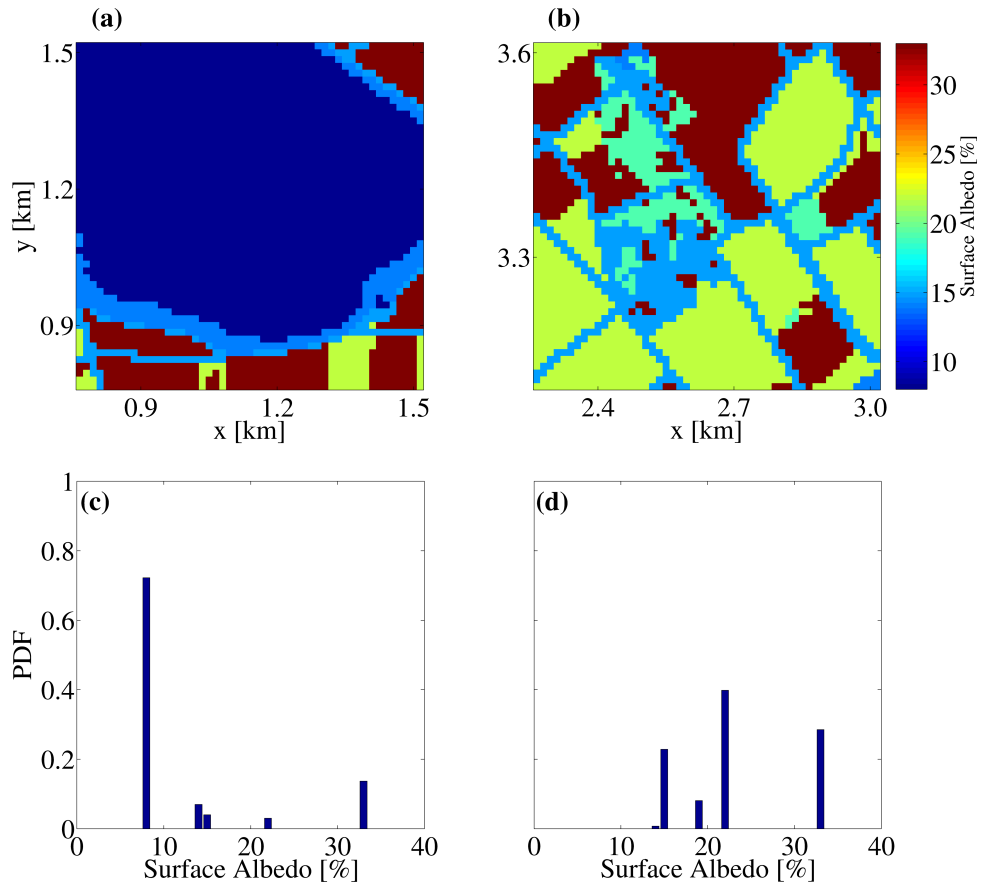


Figure 3.3: Surface albedo (a) and the corresponding PDF (c) for a relatively homogeneous surface. (b) and (d) as (a) and (c), but for a more heterogeneous surface. Taken from *Hintz et al.* [2014].

namely, the wavelet transformation. Another possibility can be the recently developed orthogonal PDF decomposition method by *Liu et al.* [2015].

3.5 Wavelet Transformation

Wavelet transformation is widely used in science for data analysis (cf. *Kumar and Foufoula-Georgiou* [1997]; *Labat* [2005] for reviews). Some other examples of the applications of wavelet transformation can be found in *Kumar and Foufoula-Georgiou* [1993], where they used wavelet transformation to analyse rain fall data. *Labat et al.* [2005] used the wavelet transformation to study the time scale vari-

ability of river discharges. *Brunsell et al.* [2008] used the wavelet transformation for the study of remote sensing data. *Gloaguen and Dimitrakopoulos* [2009] applied wavelet transformation in combination with the variogram method to analyse the spatial dependencies of geological patterns.

The wavelet transformation is an integral transformation similar to the Fourier transformation. For a function $f(x)$ and the wavelet $\Psi \in L^2(\mathbb{R})$, the wavelet transformation of $f(x)$ to the wavelet Ψ is defined as

$$L_{\Psi}f(a, b) = \frac{1}{\sqrt{c_{\Psi}|a|}} \int f(x) \Psi\left(\frac{x-b}{a}\right) dx, \quad (3.7)$$

where $L^2(\mathbb{R})$ denotes the vector space of square-integrable functions and $a \in \mathbb{R} \setminus \{0\}$ and $b \in \mathbb{R}$ are the wavelet parameters. The parameter a zooms the wavelet and b shifts the wavelet. The parameter c_{Ψ} is defined as $c_{\Psi} = 2\pi \int \frac{|\widehat{\Psi}(\omega)|^2}{|\omega|} d\omega$, where $\widehat{\Psi}(\omega)$ denotes the Fourier transformation of the wavelet. The coefficient c_{Ψ} can also be used to define a wavelet. That means every function Ψ is a wavelet, if the condition $0 < c_{\Psi} < \infty$ holds. Geometrically, the condition means that wavelets are functions which Fourier transformation decays faster than their arguments.

Many wavelets are possible for analysis. In the present thesis, the Haar wavelet (*Haar* [1910]) is used. It is defined as

$$\Psi(t) = \begin{cases} 1 & 0 \leq t < \frac{1}{2} \\ -1 & \frac{1}{2} \leq t \leq 1 \\ 0 & \text{else} \end{cases} \quad (3.8)$$

The interpretation of the Haar wavelet is that it gives the deviations of f from its local mean value. The wavelet filter acts as a high pass filter. The corresponding low pass filter is then the difference between the original signal and its high pass filter that means between f and $L_{\Psi}f$. Here, the Haar-wavelet transformation is iteratively applied to the low pass signal. The one-dimensional wavelet transformation is generalized into two dimensions by first transforming in the horizontal

3. Existing Methods for Heterogeneity Quantification

direction of the surface and afterwards in the vertical direction.

A disadvantage of the wavelet transformation, when applied to not sufficiently continuously distributed data, is that filtering can create new values, which were not present prior to filtering. For example, the low pass of 12 and 10 is 11. If the number 11 was not present in the data set prior to the filtering, the filtering would create this new value.

Via the wavelet transformation, it is possible to define a scale as the wavelet filtering length. In the case of the wavelet transformation, the filtering length is increased by a factor of two in every filtering step. For example for a data set with 15 m resolution, the filtering lengths or scales are 30 m, 60 m, 120 m etc.

3.6 Entropy

For heterogeneity quantification (cf. point (3) in the introduction), it is useful to find an integrative parameter that quantifies the amount of information of the heterogeneity, namely the information entropy. Entropy is a quantity used in many scientific fields. In the next paragraph, the origin of entropy from thermodynamics is shown (as can be found in e.g. *Fließbach* [2010]). After that, the concept is transferred to information theory by mainly following the idea of *Shannon* [1948] and a derivation which can be found in *Haken* [1983].

3.6.1 Entropy in Thermodynamics

Entropy is a well-known concept in physics. In statistical thermodynamics, one macrostate can represent a physical system, for example, the magnetization of a metal, or the pressure in a volume filled with gas. Each macrostate has a very large number of microstates, which can be the orientation of the individual spins in a metal or the velocity of the individual particles in a volume. Entropy is a macroscopic quantity which relates the logarithm of the number of microstates Ω to one macrostate M

$$S(M) = k \ln \Omega. \quad (3.9)$$

The proportionally constant k is the Boltzmann constant $k_B = 1.38 \cdot 10^{-23} \text{ J/K}$. The partition function is another term for the number of microstate. This definition builds a connection between the microscopic properties of a system and its macroscopic values. For example, the temperature T of a system can be obtained as the derivative of the entropy with respect to energy E

$$\frac{1}{T} = \frac{\partial S}{\partial E}. \quad (3.10)$$

This is done via the relation

$$dE = TdS - pdV + \mu dN. \quad (3.11)$$

The variables here are pressure p , volume V , chemical potential μ and particle number N . The entropy defined here is additive. This can be seen by looking at two systems A and B . Assuming that Ω_A is the partition function of system A and Ω_B is the partition function of system B . Then the partition function of the combined system is $\Omega = \Omega_A \Omega_B$ and the entropy calculates as

$$S = k_B \ln \Omega = k_B \ln(\Omega_A \Omega_B) = k_B [\ln \Omega_A + \ln \Omega_B] = S_A + S_B. \quad (3.12)$$

Thermodynamic entropy can be seen as a measure for the disorder of the system. The reason is, that perfect order of a system is realized when there is only one possible state, meaning $\Omega = 1$ and therefore $S = 0$. If there is a large number of microstates, then entropy is higher. Entropy reaches its maximum in the equilibrium, which is the macrostate with the highest number of microstates, which means a higher disorder of the system.

3.6.2 Entropy in Information Theory

There is another but related use of the entropy concept, which is used in the present thesis. In the following the main aspects of the entropy in information theory are derived. The derivation of the ideas is similar to that found in *Haken* [1983].

Let R be the number of possible realizations of a system, which is the number of

3. Existing Methods for Heterogeneity Quantification

how many different states a system can have. For a coin with two sides, the number of possible realizations is two. For a six-sided dice, the number is six. A connection between the number of realizations and the information S is demanded. This connection should be of the form, that information should be additive for independent realizations. That means if there are two independent realizations of the system, R_1 and R_2 then for the total number of realizations R the following condition holds

$$R = R_1 \cdot R_2. \quad (3.13)$$

For example, for two six-sided dices, $R_1 = R_2 = 6$. The total number of realizations is $R = R_1 \cdot R_2 = 36$. Like for the entropy in thermodynamics, the following condition has to be valid

$$S(R_1 \cdot R_2) = S(R_1) + S(R_2). \quad (3.14)$$

This condition can only be fulfilled, if the information or Shannon entropy (*Shannon* [1948]) is of the form

$$S = k \ln R. \quad (3.15)$$

At this stage, the choice of the constant k and the base of the logarithm are arbitrary.

A practical example is how the information is stored in a computer. All data in a computer are stored as series of length N of zeros and ones. Therefore, the number of possible realizations is 2^N . The typical unit for data storing is the bit. If information is expressed in bits, meaning that information of a series of length N of zeros and ones has the information N bit, and then the entropy is

$$S = k \ln R = k \ln 2^N = kN \ln 2 = N \text{ [bits]}. \quad (3.16)$$

That means the constant k has to be set to

$$k = \frac{1}{\ln 2} = \frac{\log_2 e}{\log_2 2} = \log_2 e. \quad (3.17)$$

In general, the constant k can have any value and can give the entropy a unit.

In the following, a practical formula is derived which is more convenient for the application to land-surface heterogeneity, that is an expression for the number of realizations R found that can be connected to the PDF of the parameters of the surface. This derivation can also be found in *Haken* [1983]. Assume a sequence of zeros and ones of length N . Let N_0 be the number of zeros and N_1 the number of ones. Then for the length of the sequence $N = N_0 + N_1$ is valid. The number of possible realizations R of this sequence can be estimated through the possible distributions of a set of N_0 elements on a set with N elements:

$$R = \binom{N}{N_0} = \frac{N!}{N_0!(N - N_0)!} = \frac{N!}{N_0!N_1!}. \quad (3.18)$$

The information $S' = k \ln R$ is then calculated as

$$S' = k (\ln N! - \ln N_0! - \ln N_1!). \quad (3.19)$$

The nomenclature is changed from S to S' , the reason for this will become clear later. With the help of Stirling's formula, the natural logarithm can be tailored in the following way

$$\ln N! \approx N(\ln N - 1) \quad (3.20)$$

For large N ($N > 100$) this approximation is good. Applying Stirling's formula to in the Equation (3.19) leads to

$$S' = k [N \ln N - N - N_0 \ln N_0 + N_0 - N_1 \ln N_1 + N_1] \quad (3.21)$$

$$S' = k [(N_0 + N_1) \ln N - N_0 \ln N_0 - N_1 \ln N_1] \quad (3.22)$$

$$S' = k [N_0 (\ln N - \ln N_0) + N_1 (\ln N - \ln N_1)] \quad (3.23)$$

$$S' = -k [N_0 (\ln N_0 - \ln N) + N_1 (\ln N_1 - \ln N)] \quad (3.24)$$

$$S' = -k \left[N_0 \ln \frac{N_0}{N} + N_1 \ln \frac{N_1}{N} \right]. \quad (3.25)$$

3. Existing Methods for Heterogeneity Quantification

By now introducing the information per symbol, it follows that

$$\frac{S'}{N} = -k \left[\frac{N_0}{N} \ln \frac{N_0}{N} + \frac{N_1}{N} \ln \frac{N_1}{N} \right]. \quad (3.26)$$

With the probability p_0 to obtain a zero or p_1 to obtain a one, that means

$$p_i = \frac{N_i}{N}, \quad i = 0, 1, \quad (3.27)$$

the entropy is

$$S = \frac{S'}{N} = -k [p_0 \ln p_0 + p_1 \ln p_1]. \quad (3.28)$$

S is called the entropy (or information) of the sequence. This can be generalized to systems that have m different states:

$$S = -k \sum_{i=1}^m p_i \ln p_i. \quad (3.29)$$

For the quantification of land-surface heterogeneity, this entropy is used. The p_i are the PDF of the investigated parameters on the surface. The constant is set to one, $k = 1$ and the logarithm is set to the base 2. The sum over the p_i is constrained by

$$\sum_{i=1}^m p_i = 1. \quad (3.30)$$

Following *Haken* [1983], it can be derived for which distribution of the parameters the entropy has its maximum value. This means to find an extreme value for the p_i . With the constraint of Equation (3.30), the method of the Lagrange multipliers is used, so that the following term is an extreme

$$- \sum_{i=1}^m p_i \ln p_i + \lambda \sum_{i=1}^m p_i = \text{Extr.} \quad (3.31)$$

The task is to find the value of Lagrange parameter λ . Therefore, the derivative with respect to p_i of the equation is taken. This leads to

$$-\ln p_i - 1 + \lambda = 0. \quad (3.32)$$

This equation has the solution

$$p_i = e^{\lambda-1}. \quad (3.33)$$

The solution is independent of the index i . Therefore, all p_i have to be equal. Putting the result in the constraint that the sum over all probabilities has to be unity

$$\sum_{i=1}^m p_i = 1 \quad (3.34)$$

leads to

$$\sum_{i=1}^m e^{\lambda-1} = M \underbrace{e^{\lambda-1}}_{p_i} = 1 \quad (3.35)$$

$$\Rightarrow p_i = \frac{1}{M}. \quad (3.36)$$

That means entropy has its maximum value if all parameters are equally distributed. This is true if the number of parameters does not change, that is $m = \text{const}$. However, when comparing the entropy of two different surfaces with different m , the entropy will be in general larger if the number of different parameter values is higher. This requires some considerations on how to compare entropies of different surfaces.

Entropies are usually additive. The entropy investigated in the present thesis is a function of the PDF of parameters on the surface. In the following, an example is shown, why it is not possible that this entropy is always additive. Figure 3.4 shows two artificial surfaces. Both of them consist of 64 grid points with two parameters. Consider the left pattern in Figure 3.4. The left area of the pattern consists of the parameter one and the right area consists of parameter two. This configuration can be seen as an analogy to thermodynamics, where a box is separated by a wall into a gas filled area and an empty area. In thermodynamics, the empty area has only one microstate, therefore the entropy is equal to zero,

3. Existing Methods for Heterogeneity Quantification

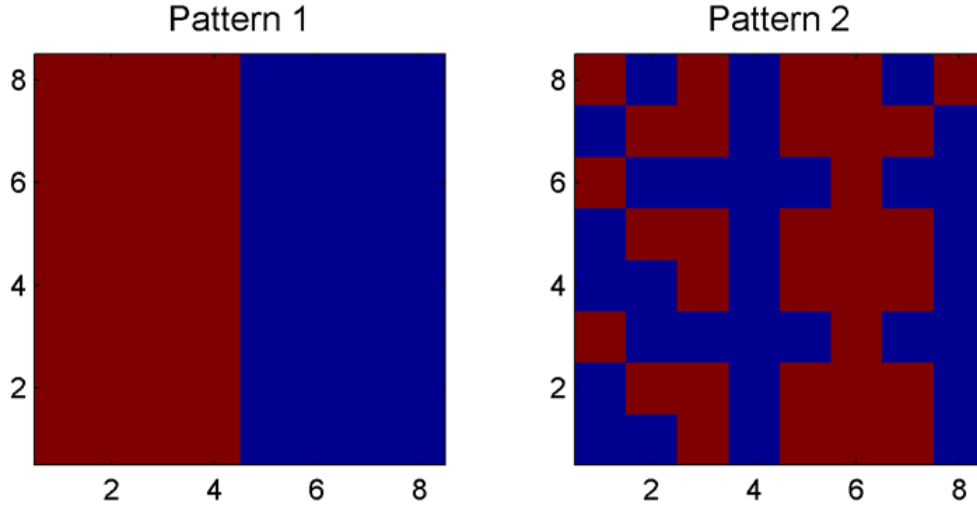


Figure 3.4: Patterns to illustrate the problem of entropy. Two artificial surfaces with 8x8 grid points. Both consist of two parameters and have the same PDF. The spatial arrangement is different, but the entropy is the same.

$S_1 = 0$. The entropy of the area filled with gas depends on the number of particles in the area. Assume there are N gas molecules. The number of different possible configurations of N particles is

$$\sum_{k=1}^{N-1} \binom{N}{k} = 2^N. \quad (3.37)$$

The entropy is calculated as follows

$$S_2 = k_B \ln 2^N = k_B N \ln 2. \quad (3.38)$$

If the wall is now removed, the particles will distribute in the whole volume. However, since the number of particles does not change, the entropy S_t of the whole system will not change,

$$S_t = k_B N \ln 2. \quad (3.39)$$

This is equal to the sum of the entropies for each individual system, that is

$$S_t = S_1 + S_2 = k_B N \ln 2. \quad (3.40)$$

In contrast to thermodynamics, it is shown in the following, that the entropy in the information theory context is not additive. Looking again at the left pattern of Figure 3.4, which has only two parameters and each parameter only in one area of the pattern. That means for the probabilities

$$p_1 = p_2 = \frac{1}{2}. \quad (3.41)$$

The entropy of pattern one is

$$S = -k \left[\frac{1}{2} \ln \frac{1}{2} + \frac{1}{2} \ln \frac{1}{2} \right] = -k \ln \frac{1}{2} = k \ln 2. \quad (3.42)$$

If the left pattern of Figure 3.4 is divided into two parts, then each part consists of one parameter only. That means that in this case $p_1 = 1$. Then the entropy of each individual part is

$$S_1 = -k p_1 \ln p_1 = 0 \quad (3.43)$$

and

$$S_2 = -k p_2 \ln p_2 = 0. \quad (3.44)$$

The total entropy

$$S_t = S_1 + S_2 = 0 \neq k \ln 2 \quad (3.45)$$

is not additive. A possible explanation is that the individual parts of the surfaces are only characterized by its PDF. The PDF does not take into account the spatial distribution of each individual grid point. It merely gives the relative occurrence of a parameter on the surface. Therefore, the PDF is the same for 64 grid points with 1 parameter or for 32 with 1 parameter. The PDF will always give $p_1 = 1$. Entropy is an integrative quantity of the PDF. If the surface is divided into parts, then the PDF will change. Due to this effect of changing the PDF, this will change the entropy. The solution would be a PDF of the surface that not only keeps track of how often a surface parameter occurs, but also on its position on the surface.

3. Existing Methods for Heterogeneity Quantification

This would lead to a multi PDF. The description of a surface with this multi PDF, that is the occurrence and position of all surface parameters, will need as much data as the surface itself. Therefore, this PDF will not help to describe the surface with fewer parameters. However, if it is possible to obtain such multi PDF of the surface, then the resulting entropy of the surface should be additive. In the present thesis, the common PDF definition is used. Therefore, a decomposition will change the PDF in a non-additive way. Consequently, the resulting entropy is not additive.

The Shannon entropy describes the information content of a surface. It is an integrative quantity of the parameter PDF. Therefore, surfaces with the same PDF will have the same entropy. This can be seen again in the example of Figure 3.4, where the two shown surfaces have the same PDF, but their spatial arrangement is obviously different. Due to the equal PDF, the entropies are identical. To solve the problem of the non-uniqueness of entropy, a decomposition method is needed to take into account the spatial arrangement. In the present study, the wavelet transformation is used in order to decompose the surface into a low- and a high pass part.

3.7 Entropy Spectrum

If the wavelet transformation and entropy calculation is applied iteratively to the low pass part, the result is an entropy distribution on different wavelet scales. This is called the entropy spectrum. It is used for the quantification of land-surface heterogeneity. It can also be used as a definition of a pattern. That means that a pattern is the distribution of information on different scales. The entropy spectrum has the following advantages. It takes into account the spatial arrangement of a pattern. That means it is able to distinguish between land surfaces with the same PDF but different spatial arrangements. The reason is the clear scale dependence of the entropy spectrum. In addition, the information aspect of heterogeneity can be estimated. With the entropy spectrum relevant scales can be determined. Moreover, the location of the relevant structures can easily be reconstructed since the sum of the low pass and the high pass reproduces the original data.



Figure 3.5: Artificial example patterns to illustrate the entropy spectrum method (the combination of wavelet transform and information entropy)

An example for the entropy spectrum and for the application for two-dimensional patterns is shown in Figure 3.5, where the two-dimensional patterns consist of the arbitrary chosen values 1, 2, 3 and 4. With the help of the wavelet transformation the surface is decomposed into a low- and high pass part. For this example, this is only done in the horizontal direction. The result is that the resolution in the horizontal direction decreased by a factor of two. This means that the two horizontal grid points have the same value in the low pass. After computing the low and high pass parts, the entropy for each is calculated. In this example, most information content lies on the first wavelet scale, since on that scale entropy has its maximum.

The approach is not completely new. It has been applied by several research groups, for example *Brunsell et al.* [2008, 2011] and *Brunsell and Anderson* [2011]. The method is improved by *Hintz et al.* [2014] by investigating the influence of the parameter PDF to the entropy spectrum. In order to distinguish which part of information comes from the surface and which comes from the parameter PDF, the entropy at each scale is compared to a reference value obtained

3. Existing Methods for Heterogeneity Quantification

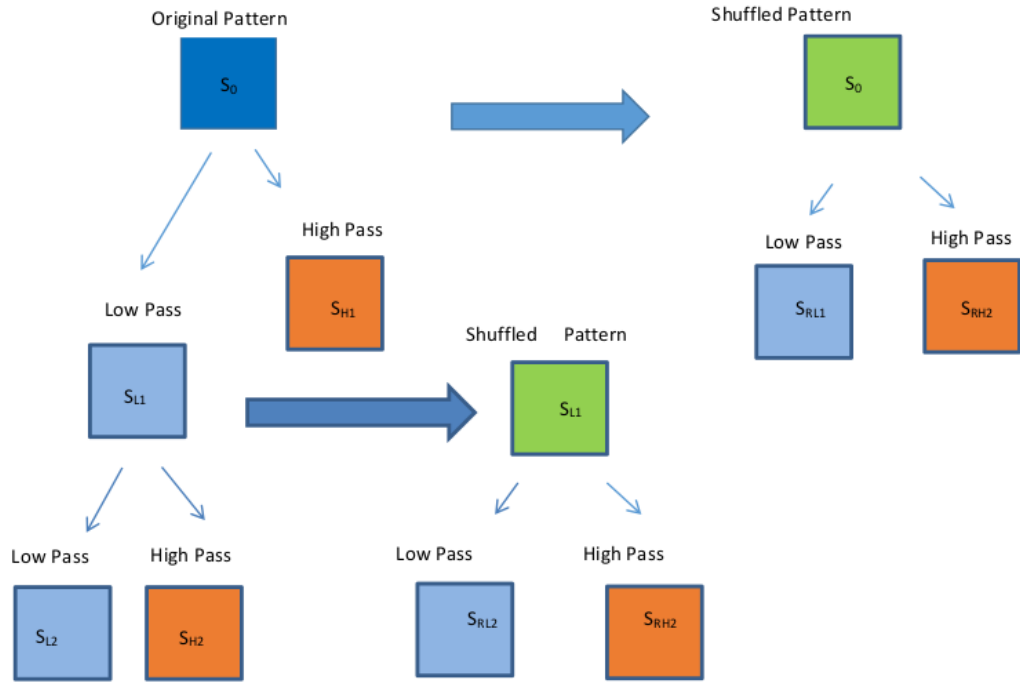


Figure 3.6: Illustration of the reference entropy spectrum. The bold blue arrows stands for shuffling of the pattern. The light blue arrows stands for applying the low- and the high pass filter, respectively. S_0 is the entropy of the original pattern which is equal to the entropy of the shuffled pattern. S_{L1} is the entropy of the level 1 low pass. S_{H1} is the entropy of the level 1 high pass. S_{RL1} stands for the entropy of the level 1 low pass obtained from the shuffled pattern. S_{RH1} stands for the entropy of the level 1 high pass obtained from shuffling the original pattern. S_{L2} is the entropy of the level 1 low pass of the level 1 low pass of the original pattern. S_{H2} is the entropy of the level 1 high pass obtained from the level 1 low pass of the original pattern. S_{RL2} stands for the entropy of the level 1 low pass obtained from the shuffled pattern of the level 1 low pass. S_{RH2} stands for the entropy of the level 1 high pass obtained from the shuffled level 1 low pass.

by estimating the low or high pass entropy of a randomly arranged surface with the same PDF as the preceding low pass. Usually, this value is different from the low- or high pass entropy obtained by iteratively applying the filter to a randomly arranged surface with the PDF of the original surface. The method to get the reference value numerically is to take the preceding low pass surface and shuffle the grid cells until all spatial correlations are destroyed. From this reference surface, the corresponding low and high pass entropies are estimated as usual. A chart to illustrate procedure of the reference spectrum is shown in Figure 3.6.

3. Existing Methods for Heterogeneity Quantification

4 Methodology

In Chapter 3 some of the main existing methods for heterogeneity quantification are outlined. It is explained, that land-surface heterogeneity can be differentiated regarding four main aspects: structure, information, anisotropy and contrast. In this thesis the focus lies on the quantification of the information aspect of land-surface heterogeneity. This quantification is done via the entropy spectrum method. This method, i.e., a combination of Shannon entropy and the wavelet transformation, has been used in studies by *Labat* [2005]; *Brunsell et al.* [2008, 2011]; *Brunsell and Anderson* [2011]. This method is independently developed in this study and has been improved by investigating the dominant scale from the entropy spectrum, as shown in the following section.

4.1 Estimation of the Dominant Scale

To illustrate how to estimate the dominant scale of a pattern, two synthetic patterns (Figure 4.1) are taken as examples. In the two patterns each cell represents an area of $15 \times 15 \text{ m}^2$. Both patterns have the same PDF. The data shown in Figure 4.1 (a) are created by randomly arranging values for each cell which corresponds to a $15 \times 15 \text{ m}^2$ area. For the pattern shown in Figure 4.1 (b) correlated structures of size 11×11 cells, corresponding to $165 \times 165 \text{ m}^2$ are created. These structures are randomly arranged.

Figure 4.2 (a) shows the low pass entropy spectrum of the random pattern shown in Figure 4.1 (a) as a solid red curve and the reference curve as a dashed red line. The solid black line represents the high pass entropy spectrum, while the

4. Methodology

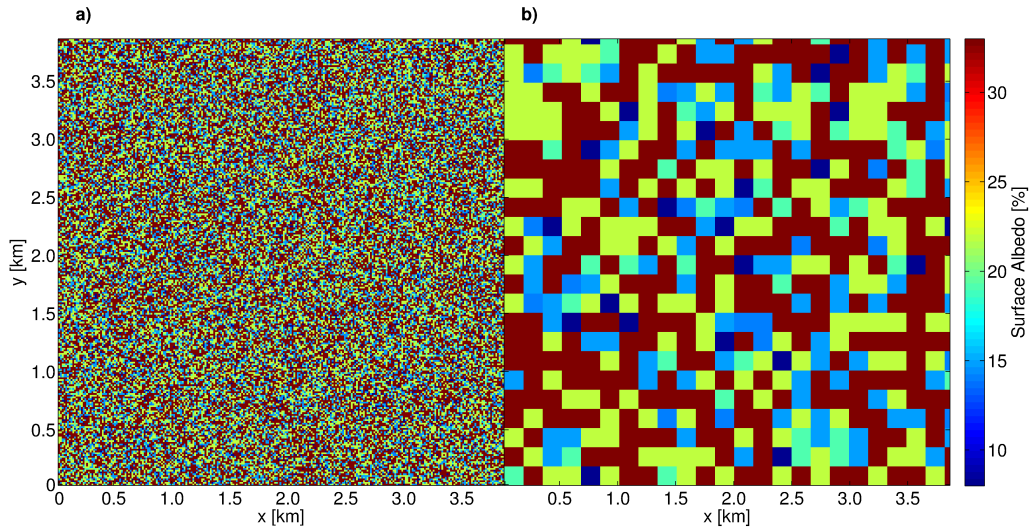


Figure 4.1: Two different synthetic surface albedo patterns with the same PDF. **(a)** Data randomly arranged with spatial resolution of 15 m, and **(b)** data randomly arranged with spatial resolution of 165 m, i.e., each big cell contains 11×11 grid cells. Taken from *Hintz et al.* [2014].

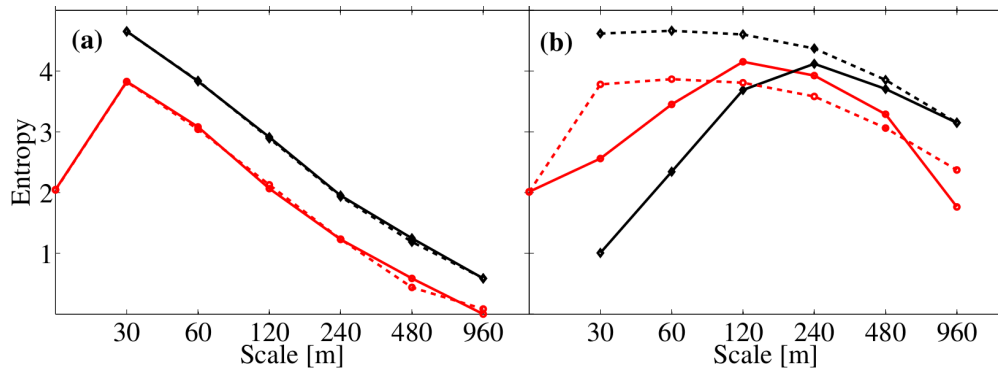


Figure 4.2: **(a)** Entropy spectrum calculated from the random surface shown in Figure 4.1 (a) The low-pass entropies are shown as red lines, and the black lines show the high-pass entropies. The full lines correspond to the estimated values, while the dashed lines correspond to the reference values, respectively. **(b)** Same as (a) but for the correlated pattern shown in Figure 4.1. Taken from *Hintz et al.* [2014].

dashed black curve corresponds to the reference high pass entropy spectrum. Figure 4.2 (b) shows the Haar entropy spectrum for the surface shown in Figure 4.1 (b) with the same color code as before. In Figure 4.2 (a), a strong increase of the entropy is seen in the first filtering step. This occurs because the distribution of the values is pronounced non-equidistant (values are 8, 14, 15, 19, 22 and 33). The Haar wavelet filter creates new values, which are not present in the original pattern. This leads to an artificial increase in entropy. In the shown example, the second and following filtering steps create only few values and enhance parameter values around the global mean value. The effect that most of the numbers lies around the global mean value dominates the effect of creating new parameter values, which leads to a decrease of entropy.

In Figure 4.2 (a), the reference curve, and the original curve agree very well with each other, verifying that the pattern is pure noise. Correlations of the surface lead to similar low-pass values. Deviations occur only at the borderlines between the structures. The effect of the borders increases with increasing filtering scale up to the half size of the structures. If new values are created at the borders, the low pass entropy of the Haar wavelet filtering increases on small scales. By studying many different surfaces it can be seen that the maximum low pass entropy might occur earliest at the filtering scale just below the structure length, and latest at the filtering scale that is twice the structure scale. Thus, if the maximum of the low pass entropy occurs at a characteristic scale, L , then the structure length λ lies between half of the scale and twice the scale. To narrow this range the position of maximum high pass entropy has to be taken into account. If the maxima of both low and high pass, occur at the same scale, L , then the dominant scale λ lies between half and the full scale, i.e.

$$0.5L \leq \lambda < L. \tag{4.1}$$

If instead the maximum of the low pass L occurs one filtering scale earlier, i.e. half the scale, than for the high pass, then the dominant scale λ lies between $L \leq \lambda < 2L$. On scales much larger than the structure sizes, the surface looks random again and the low pass entropy decreases. The entropy approaches the

4. Methodology

reference value. The filtering scales, where the deviation to the reference values are most pronounced, indicate the width of the correlated structures.

Figure 4.2 (b) shows the Haar entropy spectrum of the structure shown in Figure 4.1 (b). The red full curve shows again the low pass entropy. As predicted, it increases up to scales below the pattern size, and decrease at scales above it. The maximum low pass entropy occurs at filtering scale $L=120$ m. Thus, the pattern must have a dominant scale between 60 m and 240 m. The maximum of the high pass entropy occurs at filtering scale 240 m. This reduces the range of possible the dominant scales between 120 m and 240 m. This is in agreement with the synthetic pattern where the real length scale of the structures is 165 m. The high pass of the Haar wavelet filtering consists of the deviations between the low pass and the preceding low pass. If the surface has correlations the high pass PDF becomes peaked at value zero and the resulting entropy is small. Deviations occur again at the borders between structures. Thus, the entropy rises with increasing filtering scale up to the size of the structures. On larger scales, the structures have a noisy behavior. The entropy decreases. Therefore, the maximum of the high pass indicates the length of the structure size. For randomly arranged surfaces, the entropy is larger than in the correlated case. Thus, again the difference between the entropy value and the corresponding reference value indicates the strength of the correlations on this scale.

However the method has some limitations. The entropy spectrum is only able to find the dominant scale under the following conditions. (i) The number of values is not too large. That means the number of values should be less than 10 % of the number of grid points. This is a rough estimate. The reason is, if the number of values is too large, every surface will look random. This can be understood by investigating a pattern, where every grid point has a different value. In reality the difference of the values may be marginal; however, the entropy spectrum will still count every single value even if the value does not differ very much from its neighbor value. This problem is taken into account by normalizing and rounding of the values (cf. Section 5.1). However, if the numbers of values are too large the entropy spectrum will show a peak at the first filtering scale and then will

Table 4.1: Model setup and comparison with *Shao et al.* [2013]

	This study	<i>Shao et al.</i> [2013]
Model	LES-ALM	LES-ALM
Domain Size	3.84 x 3.84 x 2.2 km ³	7.5 x 6.0 x 2.2 km ³
Horizontal Resolution	15 m	60 m
Simulation Time	12.00 - 13.30 UTC	8.00 - 20.00 UTC
Horizontal Wind Speed	none	3-4 m s ⁻¹

show a fast decrease. This behavior is usually the behavior of a random pattern. The number of values where the method still works can depend on the spatial arrangement. (ii) The size of the biggest structures should be smaller than the filtering size. (iii) The number of values is too less. The reason is if there are only two values, the dominant scale is found at that scale, where the number of values, due to the filtering process, reaches its maximum. These errors can be avoided if one takes into account also the reference entropy spectrum. The calculation of the reference spectrum is computationally intensive. Therefore, and in order to make the results plots better to read, the reference spectrum is omitted.

4.2 Data and Model Setup

The study area is the Rur River catchment (6.4°E, 50.8°N), Germany. Many field measurements have been carried out in the context of the SFB/TR 32 Patterns in Soil-Vegetation-Atmosphere-Systems: Monitoring, Modeling, and Data Assimilation *Vereecken et al.* [2010]. The simulations are carried out for the area around the two towns Selhausen and Merken. The area is arable land with 75 % covered by cultivated plants. Typical field sizes of the region are in the range of one to a few hectares with a typical length scale of 100 m. The horizontal resolution of the data set is 15 m. The land use data set is taken from *Waldhoff* [2010]. The simulation domain is 3.84 km in the east-west direction and in the north-south direction. This is due to the fact, that with the Haar wavelet transformation, the filtering length is a power of two. Therefore, this domain size to 3.84 km = 15 m x 256 grid points is chosen.

4. Methodology

Table 4.2: Conversion between land use types and corresponding albedo values

Land Use Type	Albedo [%]
Forest	14
Pasture	19
Beet	22
Water	8
Settlement	15
Bare Soil	33

The choice of this area has the following advantages to the simulations. First, due to the structure of the fields and their typical sizes of 100 m, one of the dominant heterogeneity length scale is a priori known. Second, the data set has a resolution high enough to analyze large eddies. Third, due to the field experiments the simulation results can be compared to measurements. This has already been done by *Shao et al.* [2013] (Cf. Section 2.4.3).

Shao et al. [2013] also uses the LES-ALM. The model setup in the present thesis is equal to that of *Hintz et al.* [2014]. Table 4.1 shows the model setup, together with a comparison with the model setup of *Shao et al.* [2013]. There are two main differences in the model setup. First the resolution is chosen to be 15 m. Second the simulations are done without wind. If the simulations would be in the presence of wind, the signal of the land surface would have been shifted inside or outside of the domain. Moreover, it would be more difficult to find relationships between the lower layers and the layers above them.

4.3 Entropy Analysis of the Land Use Patterns

In this section, the applications of the entropy spectrum method to the results of numerical experiments are shown. To understand the influence of land-surface heterogeneity nine different numerical experiments with different land-use inputs are set up. These inputs are **(a)** A constant land use where the whole domain consists only of bare soil. **(b)** An arrangement, where the center of the domain is forest surrounded by bare soil. **(c)** A random arrangement with nearly the same

4.3. Entropy Analysis of the Land Use Patterns

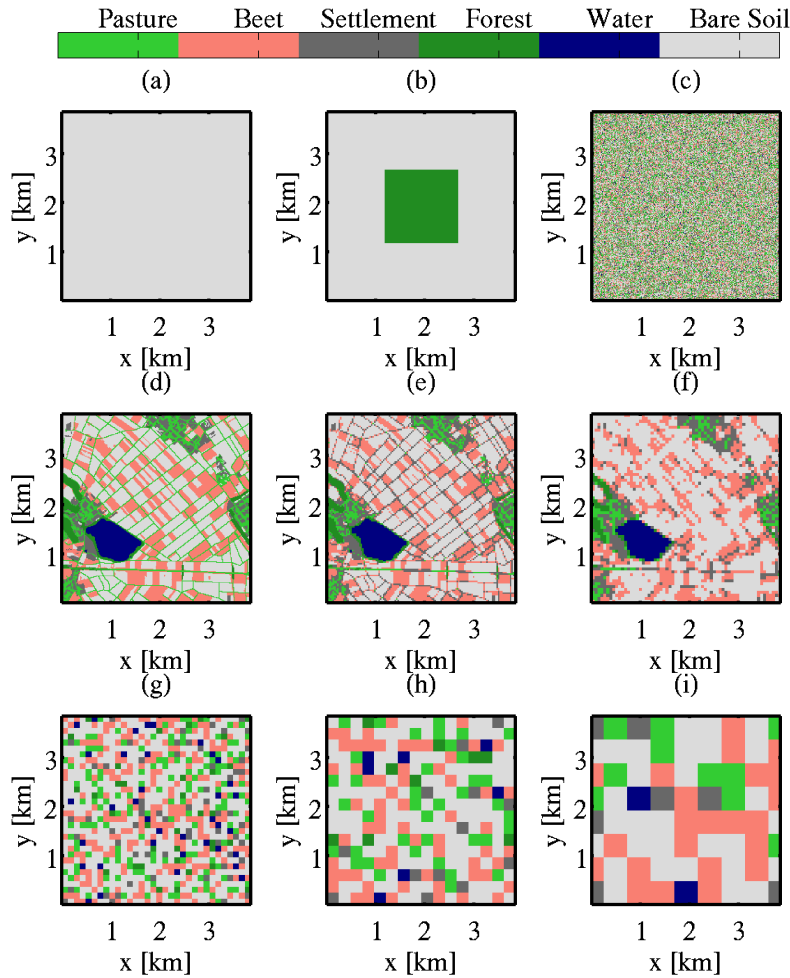


Figure 4.3: Different land uses, used as input data for the numerical experiments with the LES-ALM. **(a)** A constant land use where the whole domain consists only of bare soil. **(b)** An arrangement, where the center of the domain is forest surrounded by bare soil. **(c)** A random arrangement with nearly the same PDF as the original data. **(d)** The original land use data with 15 m structure size. **(e)** The level 1 Haar wavelet filtered surface. **(f)** The level 2 Haar wavelet filtered surface. **(g)** random arranged surface with structures of the size of 120 m **(h)** Same as (g) but the structure sizes are 240 m **(i)** Same as (g) and (h) but the structure sizes are 480 m and the blocks are shifted with respect to the origin.

4. Methodology

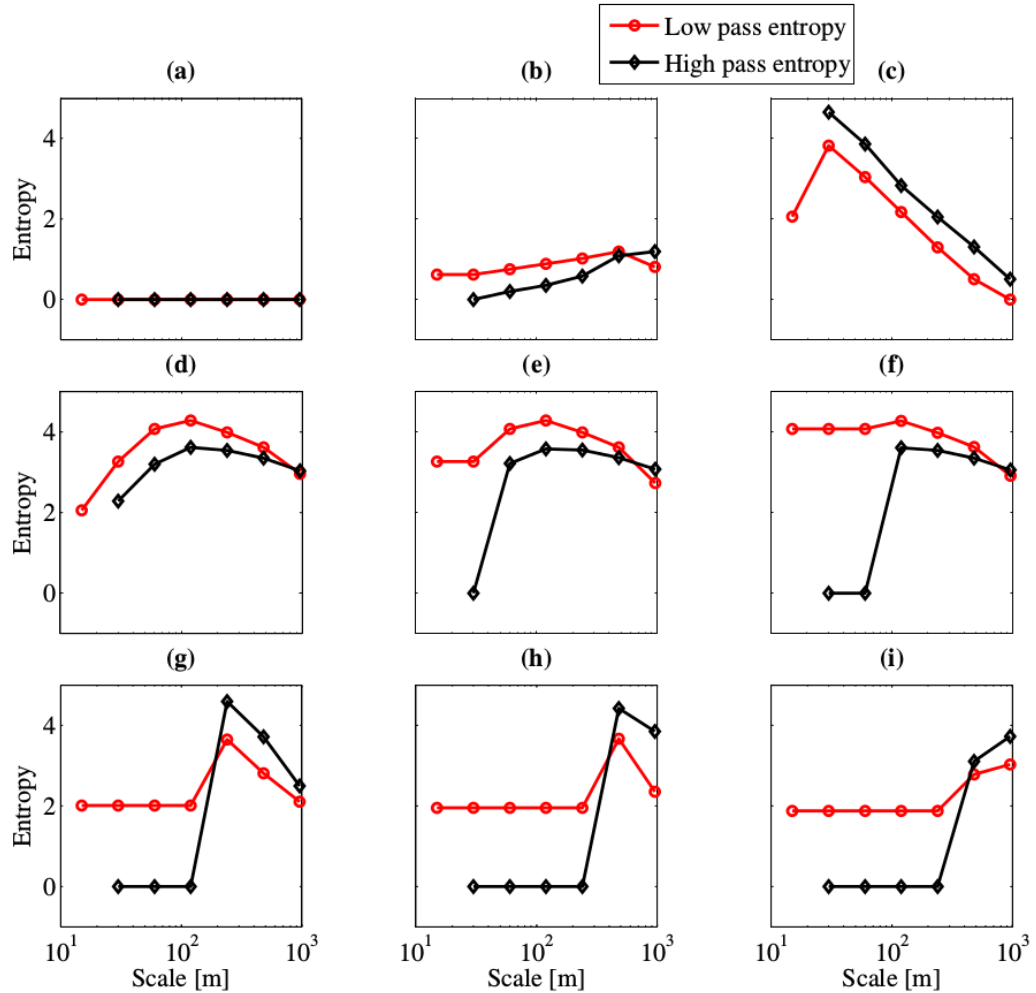


Figure 4.4: The entropy spectra of the albedo patterns shown in Figure 4.3. For **(a)** the dominant scales is $\lambda = 3840$ m. **(b)** The dominant scale lies in the range between $240 \leq \lambda < 480$ m. **(c)** The dominant scale lies in the range between $15 \leq \lambda < 30$ m **(d) - (f)** The dominant scale lies in the range between $60 \leq \lambda < 120$ m **(g)** The dominant scale lies between $120 \leq \lambda < 240$ m **(h)** The dominant scale lies in the range of $240 \leq \lambda < 480$ m **(i)** The dominant scale lies between $480 \leq \lambda < 960$ m.

4.3. Entropy Analysis of the Land Use Patterns

Table 4.3: Entropy of the different land use inputs S_{LU} and of the averaged values of temperature S_{Θ} , water vapor S_q , sensible heat flux S_H and latent heat flux S_{LE}

Land use pattern	S_{LU}	S_{Θ}	S_q	S_H	S_{LE}
(a)	0	2.23	2.48	2.33	2.44
(b)	0.62	2.15	1.46	2.15	0.70
(c)	2.12	2.43	2.38	2.16	2.17
(d)	2.05	2.34	2.44	2.06	2.25
(e)	2.02	1.85	2.32	2.05	2.01
(f)	1.89	1.72	2.43	1.87	1.96
(g)	2.01	2.24	2.41	1.99	2.19
(h)	1.95	2.20	2.28	1.96	2.07
(i)	1.88	1.99	2.87	2.04	1.63

PDF as the original data. **(d)** The original land use data with 15 m resolution. **(e)** A level 1 Haar wavelet filtered surface. **(f)** A level 2 Haar wavelet filtered surface. **(e)** and **(f)** were obtained by first converting the land use data into albedo values, and then make the Haar wavelet transformation and converting it back to land use data by combining the new created albedo values into accordingly chosen land use types. The conversion from land use to albedo values is done via Table 4.2. **(g)** An arrangement where a similar PDF as **(d)** is put together to blocks of the size of 120 m and these are then randomly distributed. **(h)** Same as **(g)** but the blocks are 240 m large. **(i)** The same as **(g)** and **(h)** but the blocks are 480 m large and the blocks are shifted with respect to the origin. That means that the borders of the blocks do not lie on the filtering window, which is for the Haar wavelet transformation a power of two. Each of the land use data has a resolution of 15 m. Table 4.3 shows the entropy of the land-use-input pattern, together with the entropy of the temporal averaged (cf. Section 5.4) values at the surface. The surfaces **(c)**, **(e)**, **(h)** and **(i)** were created with nearly the same PDF as the original data of the whole 7.5 x 6 km domain, consisting of the different land use types forest, pasture, water, settlement, beet and bare soil. However, for the simulation only a part of the domain (3.84 km x 3.84 km) is chosen. As already explained, the domain size corresponds to 256 x 256 grid points. This has been done, because if the size of the domain in grid size is a power of two then there is no confusion what might occur when the filter reaches the border of the domain. Figure 4.3 from left to

4. Methodology

right and from top to bottom show the albedo structures corresponding to these land use inputs.

For each of the land use inputs the dominant scale is computed. Due to the fact, that the entropy spectrum method cannot be applied directly to the land use values, they are first transformed into albedo values. From the albedo values the entropy spectrum and the dominant scale is then estimated. Figure 4.4 shows the entropy spectrum for each of the albedo structures of Figure 4.3. For each of the entropy spectra the dominant scale is estimated. For Figure 4.3 (a) the dominant scale is $\lambda = 3840$ m, because this distribution consists only of one value. Therefore, all entropies are to zero. Thus, the dominant scale is defined as the domain size.

For (b) the dominant scale lies in the range of $240 \leq \lambda < 480$ m. This can be estimated, because the low pass and the high pass entropy have both their maximum at the 480 m scale. That means that the dominant scale lies between $\frac{1}{2} 480 = 240$ m and 480 m. The patch size of the forest values were chosen to be of the order of 100×100 grid points, which converts to 1500×1500 m. The maximum filtering length would be 3840 m, which translate to $256=2^8$ grid points. The entropy spectra are calculated up to $64=2^6$ grid points. This corresponds to 960 m filtering length. Therefore, the entropy spectrum of Figure 4.3 (b) cannot resolve this dominant scale. The maxima of the low and the high pass entropy occur at a scale of 480 m. At this scale, the number of parameters has its maximum. Therefore, in this special and artificial case, where the surface consists only of two parameters, the dominant scale cannot be estimated correctly with the entropy spectrum method. However, this can be solved by choosing a larger domain size.

(c) For the random arranged surface, the dominant scale lies in a range between $15 \leq \lambda < 30$ m. This is consistent, because arranging the surface randomly, should destroy every spatial correlations and therefore there is no dominant length scale. The fact, that the entropy spectrum finds a dominant structure between 15 and 30 m, is reasonable, because the spatial resolution is 15 m meaning that the smallest scale possible is 15 m. The reason why the entropy does peak at the 30 m

rather than on the 15 m scale, is that the albedo values are a only six values and during the filtering process, many new albedo values between the original ones are created. In this case a higher number of values leads to a higher entropy. Consistently, the entropy spectrum estimates the lack of a dominant scale or in other words, there is no spatial correlation between the different points.

This can be discussed even further. Comparing the entropy spectrum of the structure consisting only of one value (Figure 4.4 (a)) with that of the random case (Figure 4.4 (c)). The entropy spectrum of (a) is flat, the entropy of (c) is a fast decaying function. These two cases are the extremes of a homogenous surface (a) and heterogeneous surface (c). All other surfaces lie between them. From this, it can be speculated that if the entropy spectrum has a similar shape to that of (a) or (c) it is very likely that the structure is constant or random, respectively. Of course, there can be exceptions to this rule. However, it is a first hint, how one can make a reconstruction of the pattern, if the entropy spectrum is the only known quantity.

The structure Figure 4.3 (d) consists of the albedo values obtained, by the transforming the land use data into corresponding albedo values. For the entropy spectrum, both low- and high pass entropies show a maximum at a scale $L = 120$ m. Thus, typical structures have a length scale $60 \leq \lambda < 120$ m. This is in agreement with the field size of around 100 m.

The pattern of Figure 4.3 (e) is the level one Haar wavelet transformation of the original data shown in Figure 4.3 (d). The entropy spectrum of the low pass is constant in the unfiltered and the first filtering step, i.e. at a scale of 15 m and 30 m. This is reasonable, because the in the first level Haar wavelet filtering step the average goes over 30 m of the data. The dominant scales of (d) and (e) lie on a scale larger than 60 m. Therefore, the shape of (e) is similar to that of (d) between the 30 m and 60 m.

For the same reason the dominant scale of Figure 4.3 (f) lies in the range between $60 \leq \lambda < 120$ m. However, here the first three scales have the same entropy. The

4. Methodology

shape differs from that shown in (d), but it is still able to determine the dominant scale. Even though it not so easy to perceive the maximum, as in the two spectra of (d) and (e).

The entropy spectra (g) - (i) are the spectra of the artificially generated surfaces. Their dominant scales are known in advance. This is achieved this by considering the following two points. First, blocks of a specific size (120 m for (g), 240 m for (h) and 480 m for (i)) are put together. Second, these blocks are arranged randomly so that spatial correlations is destroyed as much as possible.

From the entropy spectrum (g) can be seen that it is constant for the scales from 15 to 120 m. At the 240 m scale, both low pass and high pass entropies have a peak. So that it can be concluded, that the dominant scale lies in the range of $120 \leq \lambda < 240$ m. The sizes of the blocks with the same values are 8 x 8 grid points, which corresponds to 120 m x 120 m. Therefore, the entropy spectrum can determine the dominant scale appropriately.

The same method of arranging the surface randomly was used for the surface shown in Figure 4.3 (h). Here blocks of the size of 16 x 16 grid points (corresponding to 240 m x 240 m) are put together. The entropy spectrum gives a dominant scale of $240 \leq \lambda < 480$ m. This is again in agreement with reality.

In Figure 4.3 (i) a surface which is similar to those in (g) and (h) is shown. However, here the blocks have sizes of 480 m. To investigate the behavior of the entropy spectrum, if the filtering window does not match the block borders, the blocks are shifted so that most of block borders will not lie at even positions. Because the filtering scales are a power of two, shifting the blocks means that the filtering windows lies beyond the border of one block. It can be seen that the entropy spectrum can still resolve the dominant scale between $480 \leq \lambda < 960$ m, but the maxima are not so pronounced.

For each of the nine numerical experiments the entropy spectrum has been calculated for the physical parameters like temperature, water-vapor-mixing ratio,

4.3. Entropy Analysis of the Land Use Patterns

sensible and latent heat flux. As mentioned before the dominant scale of the pattern can be estimated, by comparing the scale of the low pass entropy and the high pass entropy. Due to the huge number of spectra, this process has been automated. Therefore, it has not been investigated what happens if the maximum of the high pass entropy occurs two scales later or at a very different position than the peak of the low pass entropy.

4. Methodology

5 Results

In this chapter, the propagation of land surface heterogeneity in the atmospheric boundary layer is investigated. This is done via the application of the entropy spectrum method to the model output of the nine numerical experiments (cf. Section 4.3). The chapter is structured as follows, after a necessary normalization of the model outputs (cf. Section 5.1), two examples of the atmospheric responses of normalized potential temperature and normalized water-vapor-mixing ratio to a homogeneous land surface are shown (cf. Section 5.2). In Section 5.3 the application of the entropy spectrum method to the model output of all nine numerical experiments after a spin-up time of 30 minutes is shown. These instantaneous output, i.e. the output at a specific time, show mainly the behavior of the atmospheric turbulence and not so much the influence of the land-surface heterogeneity. Therefore, in Section 5.4 the entropy spectrum is applied to the averaged model output. From these results it is possible to study the influence of resolution to the entropy spectrum (cf. Section 5.5). In order to validate the results obtained from the entropy spectrum method, the results are compared to statistical methods (cf. Section 5.6). For convenience, in this chapter temperature stands for the averaged potential temperature and water vapor stands for the normalized water-vapor-mixing ratio.

5.1 Normalization

In order to ensure the comparability of patterns at different heights and to simultaneously take into account the varying number of values per variable at every level, these variable values have to be normalized.

5. Results

For Gaussian distributed values, the normalization would usually be done via the standard score

$$Z_{sc}(i, j) = \frac{x(i, j) - \mu}{\sigma}, \quad (5.1)$$

where μ is the mean value of the variable x and σ is the standard deviation. For Gaussian distributed values, the normalized values usually lie between $-3\sigma \leq Z_{sc}(i, j) \leq 3\sigma$. However, for non-Gaussian distributed values, the normalized values can be much larger than 3σ or smaller than -3σ . Therefore, with the standard score, it is not easy to find a threshold, which is good for all heights. The data investigated in the present thesis are not all Gaussian distributed. Thus, the feature scaling normalization is applied. The feature scaling normalization is done as follows. For every height, the minimum value x_{\min} and the maximum value x_{\max} are calculated. Then, at each grid point (i, j) , the minimum is subtracted from the value at this point $x(i, j)$ and the result is divided by the difference between the maximum and the minimum:

$$Z(i, j) = \frac{x(i, j) - x_{\min}}{x_{\max} - x_{\min}}. \quad (5.2)$$

For the investigated data, i and j range from 1 to 256. After normalization, the normalized values lie between 0 and 1. If the variable at one height has only one value, the normalized value is set to 0.

The normalized values are rounded to the first digit. That means the variables take usually the values $[0, 0.1, 0.2, \dots, 0.9, 1]$. If the normalized values were rounded to the second digit, which means 101 different values would be possible. This would result in a low pass entropy spectrum which in most cases peaks at the first scale. The reason is that the first filtering step generates the most new values. Also the spectrum would exhibit an artificial random behavior. That means the entropy spectrum would decrease very fast after the peak. If the bin size for low and high pass would also be taken as 0.1, the resulting entropy spectrum would be flat. Therefore, for the low and high pass filter a bin size of 0.01 is used.

5.2 Responses to a Homogeneous Pattern

In the following, the entropy spectrum method is applied to an ideal experiment representing the response of temperature to a land-surface input, which consists only of bare soil. Figures 5.1 (a) - (e) show the temperature at the surface and in 3, 36, 117 and 561 m height. Figures 5.1 (f) - (j) show the corresponding entropy spectra. The temperature fields are obtained after a spin-up time of 30 minutes. This is done to assure that turbulence is fully developed. The development of larger structures from the bottom to the top of the domain are distinct. From the shape of the entropy spectrum, a dominant scale between $30 \leq \lambda < 60$ m near the surface is estimated. The shape of the high pass entropy, in particular its fast decrease, shows that the pattern of the normalized temperature has a more random distribution near the surface than in higher layers. The dominant scale increases to a range of $60 \leq \lambda < 120$ m at 36 and 177 m height. At 561 m

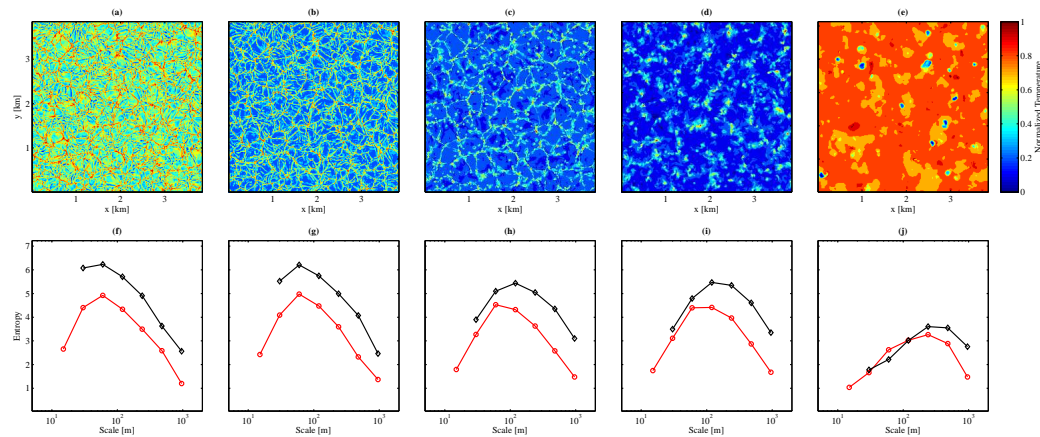


Figure 5.1: (a) - (e) Normalized temperature patterns for the bare soil land-use (experiment (a)) at the surface and in the heights of the 3, 36, 117 and 561 m at 12.30 UTC. (f) - (j) show the corresponding entropy spectra.

height, the dominant scale increases further to a range of $120 \leq \lambda < 240$ m. These dominant scales cannot be obtained visually from the temperature fields in Figures 5.1 (a) - (e) alone. The possibility to identify the dominant scale is a clear advantage of the entropy spectrum.

The water vapor for the same bare soil experiment is shown in Figure 5.2 (a) - (e)

5. Results

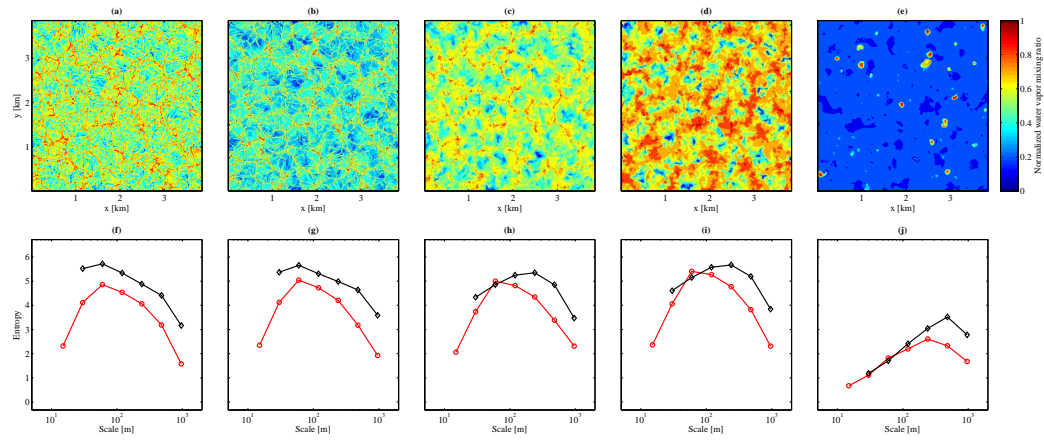


Figure 5.2: (a) - (e) Normalized water-vapor-mixing-ratio structures for the bare soil land use at the surface and in the heights of the 3, 36, 117 and 561 m. (f) - (j) show the corresponding entropy spectra.

for the patterns and (f) - (j) the corresponding entropy spectra in the same heights as for Figure 5.1. The patterns of water vapor look similar to those of temperature. Especially at 3 m height, the pattern shows a random behavior. However, in 36 and 117 m bigger structures than in the same heights for the temperature field can be seen. At 561 m, larger structures dominate, but the variations are not as large as for the temperature at the same height. These large structures at 561 m can also be seen by eye and are confirmed by the entropy spectrum. That means that the entropy spectrum can reproduce the impression of the typical structure size of a pattern as it is seen by the human eye. However, the judgement by eye can now be exchanged with an analytical procedure which is able to quantify patterns. At 3 m height, the entropy spectrum decreases fast after a filtering scale of 60 m. This is usually an indicator for a random behavior. In all levels exhibited in Figure 5.2, with the exception of 561 m, a clear maximum of the low pass filter entropy at the 60 m scale can be seen. This is also true for the temperature field. However, for the water vapor the maximum is more pronounced. A trend to larger structures with increasing height is discernible from the entropy spectra of the water vapor, where the position of the low pass entropy maximum at 561 m height, lies at the 240 m scale. The difference to the temperature is that there is an intersection between the low pass entropy and the high pass entropy, which is an indicator for correlations. This intersection occurs for temperature only at the 561 m height.

5.3 Instantaneous Responses

In this section, the results of the entropy analysis of the nine numerical experiments (explained in Section 4.3) for the instantaneous model outputs of temperature, water vapor, sensible and latent heat flux are presented. Figure 5.3 shows the entropy normalized by the entropy at the surface for the instantaneous values of temperature Θ , water vapor q , sensible H and latent heat fluxes LE at 13 UTC. From the blue line in Figure 5.3 it can be seen that for the instantaneous values of temperature, the corresponding entropies show oscillations in the first 50 m. Between 50 m and 200 m, the entropies show a small increase or decrease, depending on the land use input. At approximately 200 m the entropies begin to increase until a maximum is reached. The maxima of the entropies occur at similar heights for all experiments. That means that the height of the maximum

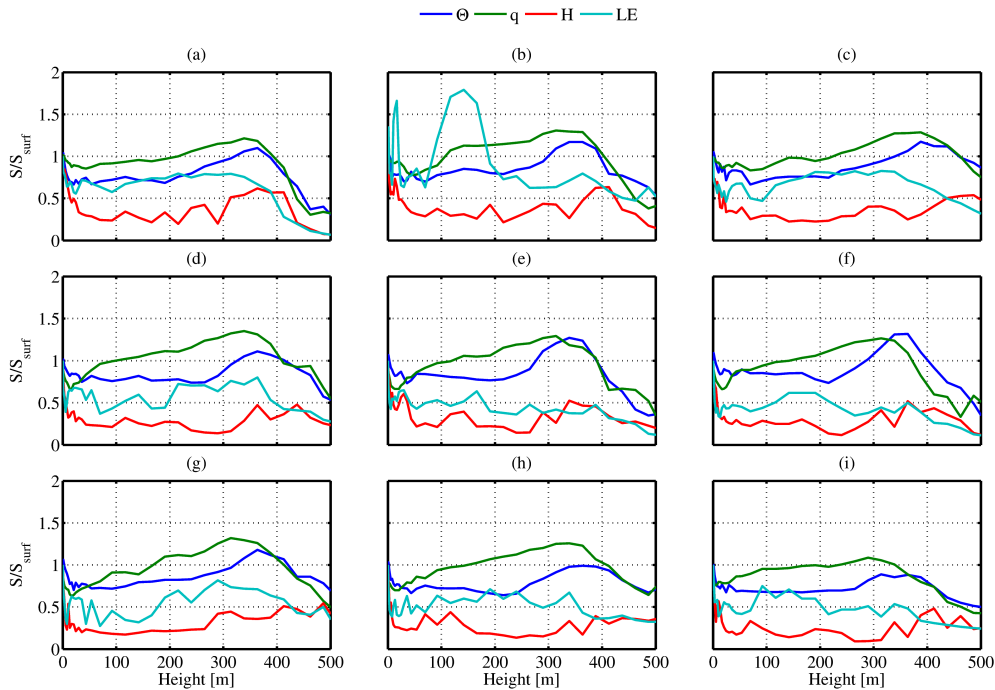


Figure 5.3: (a) - (i) Entropies normalized by the entropies at the surface as a function of height for the instantaneous values of temperature Θ , water vapor q , sensible heat flux H and latent heat flux LE at 13 UTC for the land use inputs of Figure 4.3.

5. Results

is nearly independent from the underlying land use. The positions of the maxima are 364 m for (a), (d), (g) and (h); 339 m for (b), (e) and (f); and 388 m for (c) and (i). The heights of the maxima may not have the accuracy of 1 m, since the difference between two vertical levels are 24.65 m for levels above 90 m height. In addition, for experiment (f) the maximum is difficult to obtain since the entropy of (f) is nearly constant between 339 m and 364 m.

The increase of entropy could be an indicator that above 200 m, the atmosphere begins to form an Eigen-turbulence-pattern through self-organization and the influence of the land surface vanishes. In this case, the formation of the Eigen-turbulence-patterns begins at 200 m height until it reaches its maximum information content at the heights of the position of the peak in the entropy spectrum. After that, the information content decreases with increasing height.

Even though the general shapes of the blue curves of Figure 5.3 are similar, their differences are distinct. The degree of how strong the maximum entropy decreases with height at high levels differs for each experiment. The entropy of experiments (e) and (f), which are the Haar filtered cases, have the most features in common. The main difference is that the edges of (f) look rougher than the ones in (e). The entropy of (a), (c), (d) and (g) have a similar shape. That means that the response of the atmosphere with respect to temperature is similar for a constant land use input as in experiment (a) for the original land use input in experiment (d) and for a random input with structure sizes of 15 m as in experiment (c) or 120 m as in experiment (g).

Since in experiment (a) the whole surface has bare soil as land use, the maximum entropy spectrum of (a) can be interpreted as the response of the atmosphere to a homogeneous case. The peak of the maximum entropy is clearly visible. As the surface input is homogeneous, the gain of information at higher levels leads to the conclusion that this gain is a self-organization effect, which is nearly independent of the surface for heights above 364 m. This assertion is supported by the fact that the spectra of the other experiments peak at nearly the same height as in experiment (a). If the entropy of the other experiments would peak in at different

heights compared to experiment (a), the gain of information could not be seen as independent from the land surface. In the experiments (c), (g), (h) and (i), nearly all spatial correlation is erased. This means the entropy spectra are those obtained from a random input. For (c), (g), (h) and (i) it can be seen that the increase and decrease of entropy is not so profound.

For water vapor q (green curves in Figure 5.3) all experiments look even more similar than the entropy spectra of temperature. After a decrease of entropy in the first 30 m above the surface, the entropies increase nearly linearly with height. The heights of the maxima are 339 m for the spectra of experiments (a), (b), (d) and (h); 388 m for (c); 314 m for (e), (f) and (g); and 290 m for (i). As for temperature, these heights may not have the accuracy of 1 m. After the maxima, the entropies decrease faster for (a) - (f) compared to (g) - (i). At 462 m, the entropy spectra of experiments (a), (b) and (f) show a local minimum. For (d) and (e) the entropy spectrum shows a plateau. The height of the minimum is 487 m for (h). The entropy spectra of experiments (g) and (i) do not show any special feature in the vicinity of these heights. Therefore, it can be concluded from the results, that for the instantaneous values of water vapor, the land surface is not an important factor for the information content at higher levels.

The entropy profiles of the sensible heat flux H (red curve in Figure 5.3) show much more variations than the corresponding ones for temperature and water vapor. For the sensible heat flux the entropy decrease in the first 20 m above surface. The entropy of experiment (b), (c), (e) (g) and (f) show some oscillations in this height, while the entropy of experiments (a), (d) and (h) decrease smoothly. It is difficult to obtain insights from these spectra, since their shape is dominated by oscillations. However, maxima can be detected at 364 m for (a), (d) and (f); 388 m for (b) and (h); 314 m for (c) and (g); 339 for (e); and 413 m for (i). Another difference to temperature and water vapor is that the entropy for the sensible heat flux is below 1 for nearly all heights. That means that information at the surface has its maximum value and due to the atmospheric motion the information at higher levels is destroyed.

5. Results

The entropy of the latent heat flux LE (cyan curve in Figure 5.3) exhibit similar variations as that of the sensible heat flux. However, for latent heat flux there are significant differences in the entropy between the different experiments. After oscillations in the first 100 m above surface, the entropy spectra of experiment (a) and (c) are smooth, with an increasing entropy up to a maximum of 314 m. The entropy of experiment (b) shows three local maxima: the first at 17 m, the second at 142 m and the third at 364 m. The position of the maxima for the experiments (d) - (i) are 364 m for (d); 166 m for (e) and (f); 290 m for (g); 339 m for (h); and 92 m for (i). That means that for the instantaneous values of latent heat, the land use is important, since maxima of entropy has some correspondence with the underlying land use input. However, it is difficult to find a relationship between the heights of the maxima and the dominant scale of the underlying land use input.

The results show that for the instantaneous values of the model output it is difficult to relate the entropy spectrum to the underlying land use input. Therefore, the entropy spectrum is applied to temporal averaged parameters.

5.4 Temporally Averaged Responses

In the following, the results of the entropy analysis of the nine numerical experiments for the temporally averaged parameters are shown. Figure 5.4 shows the entropy normalized by that at the surface for temperature Θ , water vapor q , sensible H and latent LE heat fluxes averaged over a time period from 1300 - 1330 UTC as a function of height. Figure 5.4 illustrates the differences and similarities between the entropy profiles of temperature, water vapor, sensible and latent heat flux. The entropy spectra for all experiments, except the entropy spectrum of latent heat flux LE of experiment (b), show a similar behavior. That means as for the instantaneous parameters, it is difficult to see the influence of the underlying land surface and when this influence can be neglected. However, some insights can be found. Therefore, in the following a detailed description of the similarities and differences between the entropy spectra for the different parameters and experiments are shown. From that some conclusions are obtained.

5.4. Temporally Averaged Responses

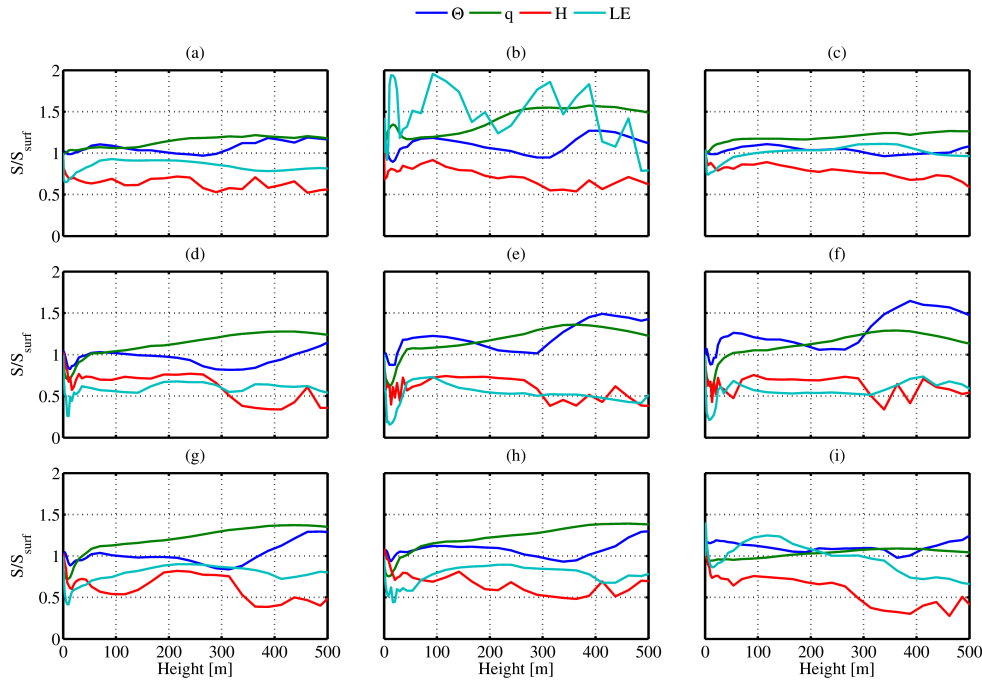


Figure 5.4: Entropy normalized by that at the surface for temperature Θ (blue), the water vapor q (green), sensible H (red) and latent LE (cyan) heat fluxes averaged over a time period from 1300 - 1330 UTC for all nine numerical experiments as a function of height.

From Figure 5.4 it can be seen that entropy profiles for temperature have a similar shape for experiments (a) and (c), which are the constant land use and the randomly arranged land use patterns with 15 m structure size. This is reasonable since it shows that temperature in the atmosphere responds to a homogeneous land use in a similar way as to a land use with very small structures. For (a) and (c) the entropy values do not exceed 1.2. This implies that the information content at higher levels is similar to that at the surface. The entropy profiles of experiments (b), (d), (e), (f), (g) and (h) show a decrease of entropy in the first meters above the surface. At approximately 30 to 40 m, a local minimum is reached. After this minimum the entropy is increasing to local maximum is reached. The heights of these maxima are not very profound for most of the experiments. They are approximately at the heights of 70 m for experiment (a); 92 m for experiments (b) and (e); 117 m for experiment (c); 70 m for experiment (d); 54 m for experi-

5. Results

ment (f); 240 m for experiments (g) and (h); and 314 m for experiments (i). The position of the second minimum for the normalized entropy lies in the interval between 290 and 364 m. The entropy spectra of show a second maximum at approximately 400 m for experiments (e) and (f). These approximate heights can be interpreted as the heights where the influence of the land-surface heterogeneity begins to become less important.

The profiles that have the most similar shape are the spectra of the random structure with 120 m structure size in experiment (g) and the random structure with a structure size of 240 m in experiment (h). This can be explained as follows. From Table 4.3 it can be seen that the entropies of temperature at the surface for experiments (a), (g) and (h) are similar. That means that at the surface the temperature has a similar PDF for all three experiments. The similarity between these three entropy spectra means that similar PDF of temperature at the surface is important. In other words, if the information of temperature at the surface is similar, then the responses of temperature in higher levels are similar. An exception is if the land surface is constant, as in experiment (a). The reason for that is, even though the PDF of temperature is similar to that of (g) and (h), the response of the atmosphere is determined more by the constant land use pattern. The land use patterns of experiments (g) and (h) are similar in terms of their correlation: Both are randomly arranged, which means that most correlations are destroyed.

From Figure 5.4 it can be seen that the shape of the spectrum of the original land use pattern in experiment (d) has more similarities with the spectra of the random patterns in experiments (g) and (h) than with experiments (e) and (f). The underlying land use inputs of experiments (e) and (f) are the level 1 and level 2 Haar wavelet filtered experiments. Therefore, it is expected that the entropy spectra of experiments (d), (e) and (f) should show more similarities than (d) with (g) and (h). This can be explained as follows. Since the PDF of (d) is more similar to that of (g) and (h) than to the PDF of experiments (e) and (f), it can be concluded that for the response of the temperature the PDF is more important than the arrangement of the underlying land use. Otherwise, the entropy spectra of experiment (d) with (e) and (f) would have more features in common. The construction of the

5.4. Temporally Averaged Responses

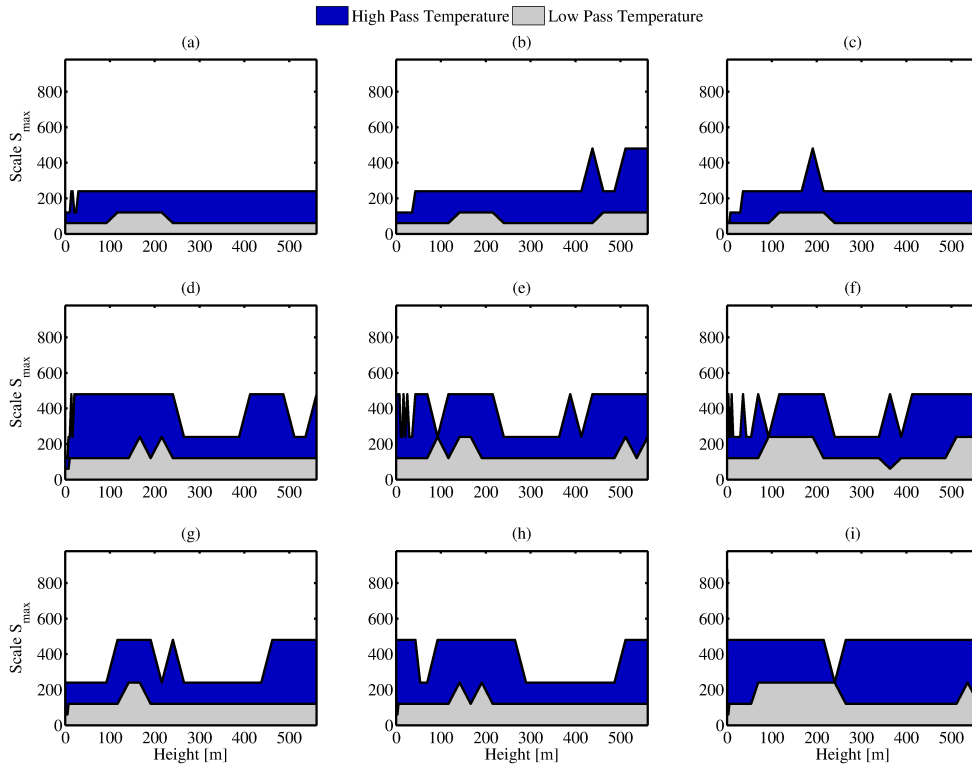


Figure 5.5: Scale of the maximum entropy S_{\max} of the temporal average of temperature Θ between 13.00 - 13.30 UTC as a function of height. The grey area shows the scale of the maximum low pass entropy. The blue area shows the scale of the maximum high pass entropy.

land use patterns (g) and (h) through the Haar wavelet transformation is that the resolution decreases by a factor of two from (d) to (e) and by a factor of 4 from (d) to (f). This decrease in resolution is not perfect, since the transformation is applied to albedo values and not to the land use itself. Since the entropy spectra of experiments (e) and (f) look similar it can be concluded that this change of resolution has a minor effect on the response of temperature. This argument is supported by the similarities of the entropy spectra (g) and (h), where the structure size increases by a factor of two from 120 m to 240 m. That a very fine or a very coarse resolution has an effect on the response of the temperature can be seen by the fact that the entropy spectra of experiment (d) is not strongly related to the entropy spectra of experiments (e) and (f). In addition, for the coarse resolution of experiment (i), the response is different from that of experiments (g) and (h). The

5. Results

effect of the different resolutions is discussed in more detail in Section 5.5. The entropy spectrum of experiment (b), which is a forest patch surrounded by bare soil, differs strongly from all other entropy spectra. This is due to the fact that the land surface pattern of experiment (b) is very different to that of the others. The reason why it is not totally different from the others lies in the fact that the PDF of the temperature at the surface is similar to that of (a), (d), (g) and (h). The spectrum of the experiment (i) is also different from the others, since firstly the land use pattern has a large structure size of 480 m and secondly the borders of the structures are shifted compared to experiments (g) and (h).

In order to find a relationship between the dominant scale of the model output and the normalized entropy, the maximum of the low and high pass entropy at each height is computed. The scale of maximum entropy is the scale on which the maximum entropy occurs. For example, the scale of the maximum entropy of spectrum of Figure 4.2 (d) is the 120 m scale. As explained in Section 4.1 the scale on which the maximum low and high pass entropy occurs is connected to the dominant scale of the pattern. Figure 5.5 shows the scale of the maximum of the low pass entropy (grey area) and of the high pass (blue area) as a function of height. From Figure 5.5 it can be seen that for the entropy spectra of experiments (a) and (c), the position of the maximum of the low pass entropy increases after 117 m height and decreases after 216 m height. In this interval, the position of the entropy remains constant at the 120 m scale. This interval of the constant low pass occurs for all of the nine numerical experiments performed in the present study. However, for experiments (d), (e) and (h), this plateau is interrupted. From Figure 5.5 it can be seen that if the scale of the maximum low pass entropy does not change, the entropy curve roughly follows the change of the scale of the high pass entropy. This can be seen for example in the entropy spectrum of experiment (d) where, after 240 m height, the position of the maximum high pass entropy decreases from 480 to 240 m. At 413 m height, the scale of the maximum high pass entropy increases from 240 to 480 m. The entropy mimics roughly this behavior. A similar behavior can be seen in entropy spectrum of experiments (e) between 216 and 388 m height, as well as in the entropy spectrum of experiment (f) between 216 and 364 m height. However, in order to certain the hypothesis of

5.4. Temporally Averaged Responses

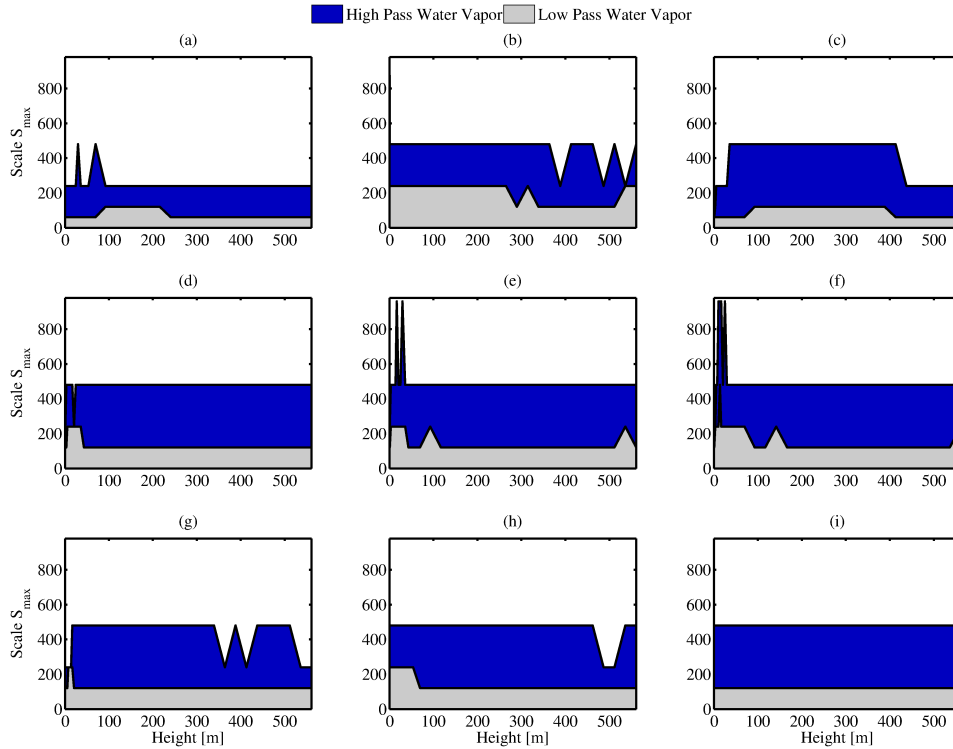


Figure 5.6: Scale of the maximum entropy S_{\max} of the temporal average of water vapor q between 13.00 - 13.30 UTC. The grey area shows the scale of the maximum low pass entropy. The blue area shows the scale of the maximum high pass entropy.

a direct connection between the scale of the maximum high pass entropy and the change of normalized entropy, more entropy spectra need to be investigated. In addition, for some entropy spectra, for example the entropy spectrum of experiment (h) between 43 and 92 m height, the change of the scale of the maximum high pass entropy does not lead to significant change of normalized entropy. The scale of the high pass entropy maximum shows more variations than the low pass entropy maximum for experiments (d) - (h). Especially for experiments (e) and (f), the oscillations of the scale of maximum high pass entropy are stronger than for other experiments. A general tendency is that the position of the high pass entropy maximum increases in the first 50 m above surface. It stays constant in heights of 100 to 300 m above ground and decreases after approximately 300 m height. In addition, it can be seen that for larger resolutions of the underlying

5. Results

land surface input, the high pass entropy maximum shows more oscillations. This can be seen by comparing experiment (d) with (e) and (f); and (c) with (g) and (h), respectively. However, if the resolution becomes too coarse or the structures become too large, the variations in the high pass entropy maximum decrease. For example, for experiments (b) and (i), the variations in the high pass entropy maximum are not well pronounced.

The spectra of entropy for water vapor q look more similar for all nine numerical experiments performed in the present thesis, than the spectra of the entropies of temperature Θ shown above. It can be seen from Figure 5.4 that the spectra do not show a minimum in the same height as the entropy spectra of the temperature. After 15 m height, the entropies for experiments (d) - (h) increase with increasing height. Below 15 m height these entropy spectra show a global minimum. The minimum is connected to an increase in the scale of the maximum low pass entropy shown in Figure 5.6. The similarities between the different entropy spectra are reflected by the approximately constant scales of the low and high pass entropy maxima. For the water vapor these scales do not change with height for (d) - (f) and (i) after 15 m height. For all of the entropy spectra the normalized entropies show a maximum approximately 400 m height. The maxima are approximately independent from the land-surface pattern. For experiments (a), (c) and (i) the entropy stays in essence constant. For (b) the entropy show a local maximum at 17 m height. The conclusion is that for a homogeneous (a) and a random surface (c) as well as a land-surface pattern with large structures, the response of water vapor is similar. Also for structures with a similar information content, but different spatial arrangement the responses are similar. For a land-surface pattern with strong contrast and a very different information content, the response of water vapor in lower heights is completely different. However in levels higher than 70 m the response of water vapor is similar. Figure 5.6 shows the scales of maximum low- and high pass entropy. These scales do not change very much with height. This leads to the conclusion that if the scales of maximum low- and high pass entropy do not change very much, then the corresponding entropy spectrum does not show many oscillations.

5.4. Temporally Averaged Responses

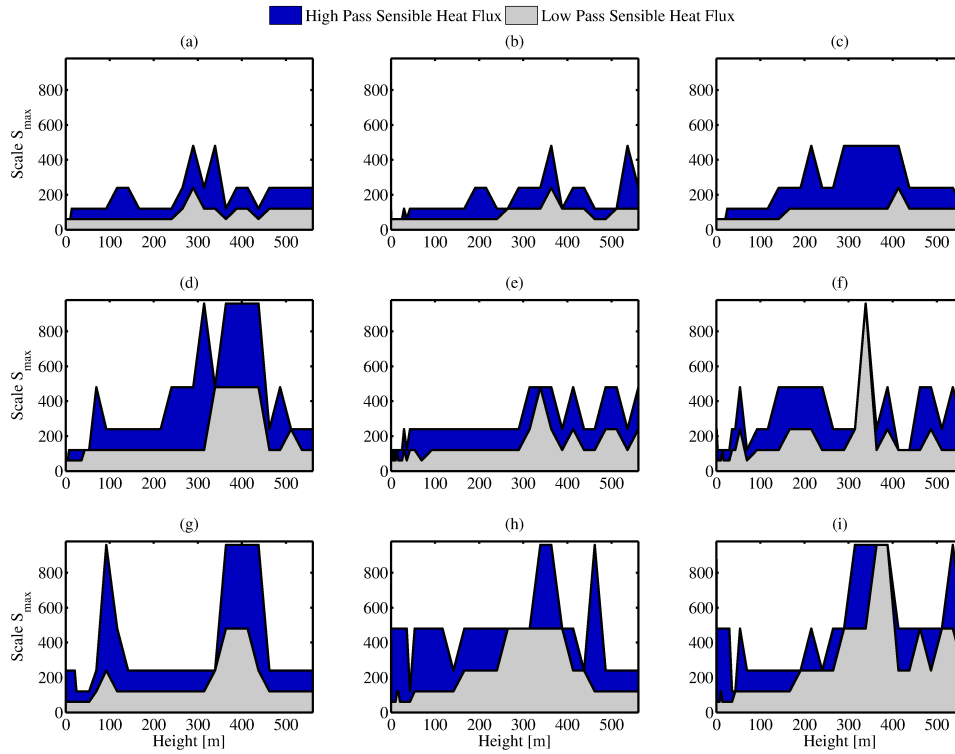


Figure 5.7: Scale of the maximum entropy S_{\max} of the temporal average of the sensible heat flux H between 13.00 - 13.30 UTC as a function of height. The grey area shows the scale of the maximum low pass entropy. The blue area shows the scale of the maximum high pass entropy.

The red curve in Figure 5.4 shows the entropy spectra of the sensible heat flux H as a function of height. These spectra show the most variations compared to the entropy spectra of temperature and water vapor. The entropy of sensible heat flux gradually decreases with height. In addition, it can be seen that the entropy is below 1 for all heights above the surface. That means the information at the surface is maximal. The spectrum for experiment (a) is approximately constant. The entropy spectrum of experiment (b) is also nearly constant, but there is a trend to lower entropies at higher levels. The entropy spectra of experiments (c), (h) and (i) show a similar decrease of entropy. The entropy spectra of experiments (d) - (f) have some features in common: Firstly all show oscillations at lower heights, secondly the plateau between 60 m and 260 m height and thirdly a decrease of entropy in levels above 260 m. This leads to the conclusion that the height of 260

5. Results

m is the height where the information of the underlying land surface is negligible. By taking into account the scale of maximum low- and high pass entropy shown in Figure 5.7, it can be seen that the decrease of normalized entropy corresponds to an increase of the scale of low- and high pass entropy. However, this behavior is only true for experiments (d) - (f). The plateau and the decrease of entropy can also be seen in the entropy spectrum of experiment (g). However, spectrum (g) differs from (d) in the occurrence of a local minimum at 92 m. From Figure 5.7 it can be seen that the minimum at 92 m can be related to the increase of the low and high pass maxima at the same height. In addition, it can be seen that an increase in scales of both low and high pass entropy lead to a minimum of normalized entropy. Figure 5.7 also shows that the scales of the maximum low and high pass entropy have more variations than for the other parameters. This can be a hint, that for the sensible heat flux, the change in the dominant scale of the sensible heat flux pattern, leads to oscillating entropy.

The entropy spectra of latent heat flux LE are shown as the cyan curves in Figure 5.4. From the Figure it can be seen that all entropy spectra, except for the entropy spectrum of experiment (b), do not show as much variations as the sensible heat flux H (cf. red curve in Figure 5.4). Although for most of experiments the entropy maxima are not very profound, the following heights can be obtained. The heights are 92 m for experiments (a) and (e); 339 m for experiment (c); 290 m for experiment (d), 412 m for experiment (f); 216 m for experiments (g) and (h); and 142 m for experiment (h). For experiment (b) it is difficult to find the maximum. The scales of the maximum low and high pass entropy are shown in Figure 5.8. For (b) the position of the high pass entropy maximum oscillate. However, the oscillating behavior of entropy cannot be explained by the change of the scale of maximum entropy. Since the contrast between the land use values of experiment (b) is much higher than for the other eight experiments, and since the effect that the latent heat flux is related to the vertical velocity and the water vapor, the oscillation can be explained by the strong circulations induced by the strong contrast. The connection between water vapor and latent heat flux leads to a smoother entropy spectrum. However, the entropy spectra of water vapor and the latent heat flux are not identical. As for sensible heat flux, the entropy is lower than 1 above

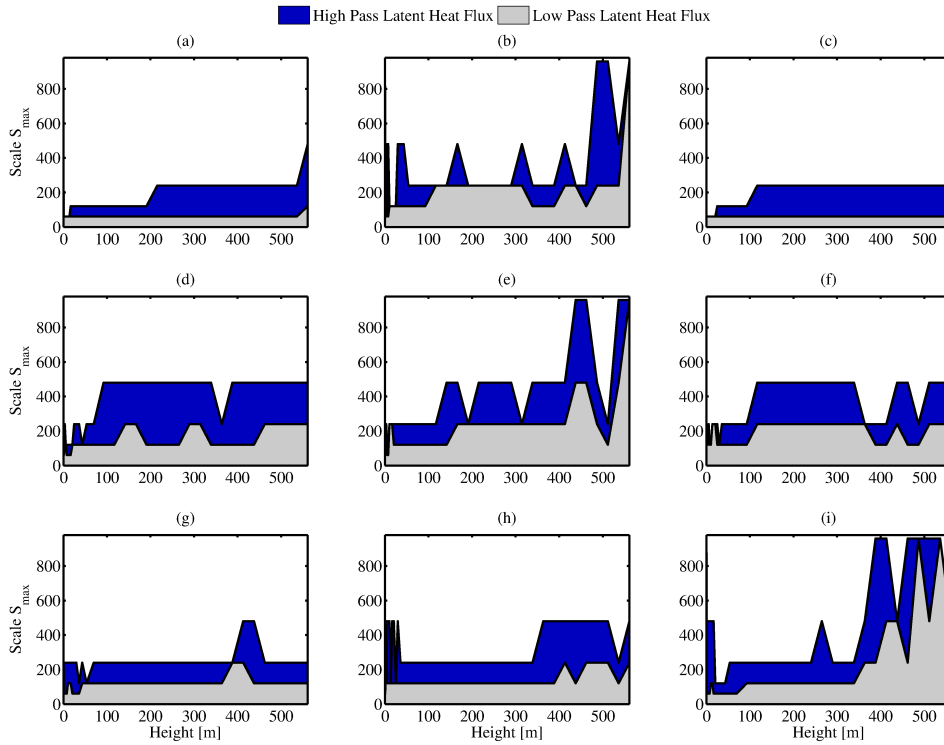


Figure 5.8: Scale of the maximum entropy S_{\max} of the temporal average of the latent heat flux LE between 13.00 - 13.30 UTC as a function of height. The grey area shows the scale of the maximum low pass entropy. The blue area shows the scale of the maximum high pass entropy.

the surface for most of the experiments. This means that the information content at the surface is maximal. Only for the entropy spectrum of experiment (b) as well as the entropy spectrum of experiment (c) between 265 and 413 m and the entropy spectrum of experiment (i) between 43 and 314 m the entropy exceed 1. From Figure 5.8 which shows the scale of the entropy maxima it is difficult to find a connection between the change of scale and the shape of the normalized entropy curve.

5.5 The Influence of Resolution

The question how the resolution influences the entropy spectrum of the averaged values of temperature, water vapor, sensible and latent heat fluxes is investigated

5. Results

in this section. Figure 5.9 shows the normalized entropy spectrum of temperature (Figure 5.9 (a)), water vapor (Figure 5.9 (b)), sensible heat flux (Figure 5.9 (c)) and latent heat flux (Figure 5.9 (d)), for the experiments where the underlying land use input is the original land use (blue line in Figure 5.9), the level 1 Haar wavelet transformed land use input (green line in Figure 5.9) and the level 2 Haar wavelet transformed land use input (red line in Figure 5.9). The resolution of the land use input decreases by a factor of 2 from the original land use input to the level 1 Haar wavelet transformed land use input and by a factor of 4 from the original land use input to the level 2 Haar wavelet transformed land use input (cf. Section 4.3). Therefore it is reasonable to compare the results for these three land use inputs in more detail. From Figure 5.9 (a) it can be seen that the entropy profiles of temperature looks similar for the three experiments, as discussed in Section 5.4. By now going into more detail, it can be seen, that a decrease of resolution of the underlying land use input, leads to an increase of entropy of temperature. From Figure 5.9 (a) it can also be seen that this increase is larger comparing the entropy results for the original land use input to the level 1 Haar wavelet transformed land use input, than comparing the entropy of the level 1 Haar wavelet transformed land use input to the level 2 Haar wavelet transformed land use input. In addition, the second maximum at approximately 400 m height, of the entropy spectra of level 1 Haar wavelet transformed land use input and the level 2 Haar wavelet transformed level 2 Haar wavelet transformed land use input is not visible in the entropy spectra of the original land use input. That means that decreasing the resolution of the land use input can lead to a different behavior in the entropy spectrum at higher levels. That the entropy spectra of the level 1 Haar wavelet transformed and the level 2 Haar wavelet transformed land use input have a more similar shape compared to the entropy spectrum of the original land use input is not expected. From Figure 4.3 it can be seen that for the level 1 Haar wavelet transformed land use input (Figure 4.3 (e)) only small scale heterogeneities are removed. These heterogeneities are smaller than 30 m. For the level 2 Haar wavelet transformed land use input (Figure 4.3 (f)) heterogeneities with sizes smaller than 60 m are removed. From Figure 4.3 (f) it can be seen that for example the streets between the fields are removed. It is expected that removing prominent features from the land use pattern (in this case the streets between the field) should have more influence on

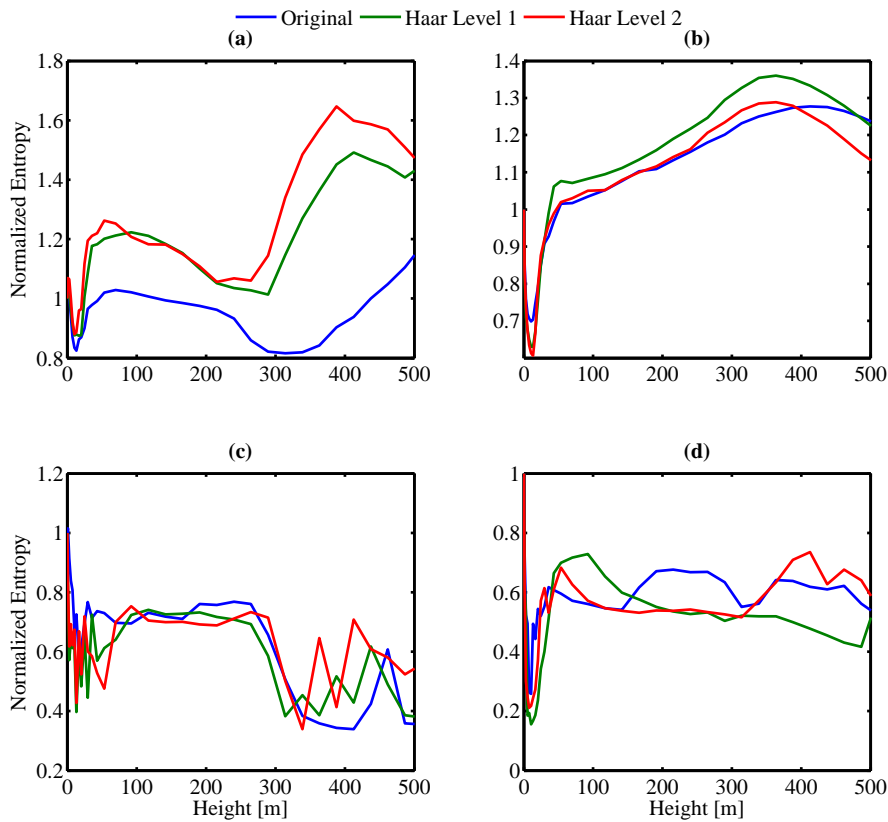


Figure 5.9: Influence of resolution to correlated land use patterns. The land use inputs are the original land use input (blue curve), the level 1 Haar wavelet transformed land use input (green curve) and the level 2 Haar wavelet transformed land use input (red curve) for the averaged values of **(a)** temperature **(b)** water vapor **(c)** sensible heat flux and **(d)** latent heat flux.

the response of temperature than removing only smaller features of the land use.

As discussed in Section 5.4 the resolution of the land-use input does not have a big influence on the behavior on the entropy spectrum of water vapor. However, the trend that decreasing the resolution leads to an increase of entropy is apparent in Figure 5.9 (b).

Figure 5.9 (c) shows the entropy spectra of sensible heat flux for the three land use inputs. In contrast to the entropy spectra of temperature the decrease of reso-

5. Results

lution does not lead to an increase of entropy. From the figure it can be seen that decreasing the resolution of the underlying land use input leads to more oscillations in the entropy spectrum. This behavior is not expected, since oscillations of the entropy spectrum should be interpreted as more dynamics of the investigated parameter. By removing small scale heterogeneities of the land use input, it is expected that the sensible heat flux should be less dynamic. The interpretation of a more oscillating entropy spectrum is that the small scale heterogeneities are not important for the averaged sensible heat flux. In this case the heterogeneities smaller than 30 m do not lead to more variations of the averaged sensible heat flux. However, as explained in Section 5.4 the height at which the influence of the land use pattern is negligible is not affected by removing small-scale heterogeneities from the land use pattern.

Figure 5.9 (d) shows the entropy spectra of the averaged latent heat flux of the three land use inputs. It can be seen that the values of the entropy are near to each other. However, decreasing the resolution leads to a different behavior of the entropy spectra. After approximately 100 m height, the entropy minima and maxima of the latent heat flux for the original land use input lie in different heights than the entropy minima and maxima of the latent heat flux for the level 1 and level 2 Haar wavelet transformed land use input. That means for these three experiments decreasing the resolution of the land surface input change the entropy spectrum.

The investigation of the resolution of the land surface input can be extended to uncorrelated land use patterns. Figure 5.10 shows the entropy spectra of temperature, water vapor, sensible and latent heat flux of the uncorrelated land surface patterns with different structure sizes. These different structure sizes can be interpreted as different resolutions. Figure 5.10 (a) shows the entropy spectra of temperature. It can be seen that for uncorrelated structures, decreasing the structure size leads to different entropy spectra of temperature. Increasing the structure size from 15 m to 120 leads to a decrease of entropy until approximately 350 m height. A further increase of structure size leads to an increase of entropy.

For the entropy spectra of water vapor (Figure 5.10 (b)), the spectrum where the

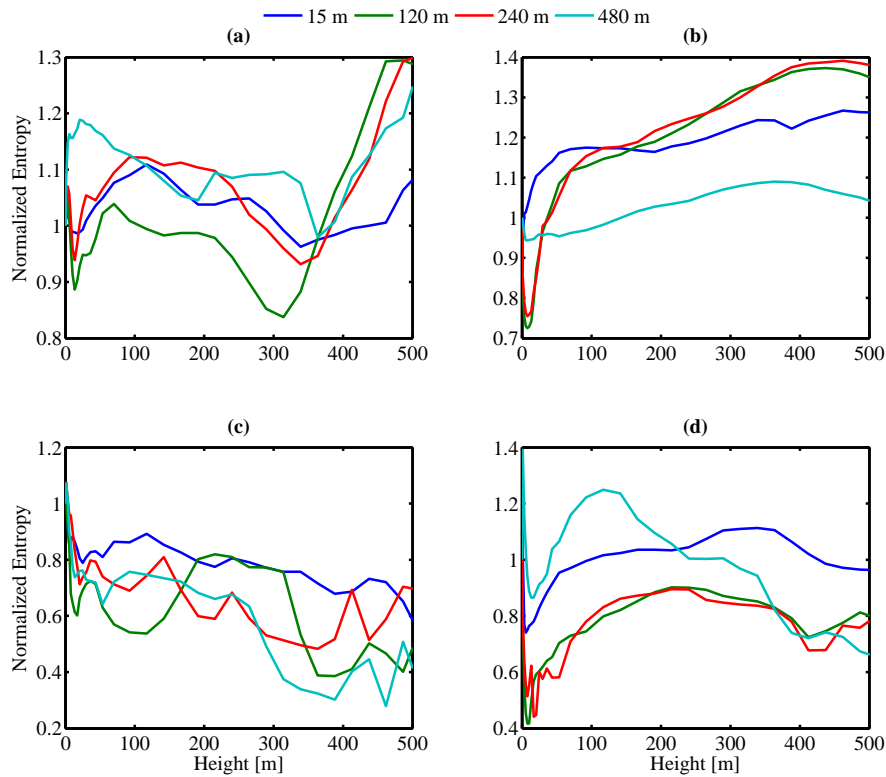


Figure 5.10: Influence of resolution to uncorrelated land use patterns. The land use inputs are the random land use input with 15 m structure size (blue curve), the random land use input with 120 m structure size (green curve), the random land use input with 240 m structure size (red curve) and the random land use input with 480 m structure size (cyan curve) for the averaged values of (a) temperature (b) water vapor (c) sensible heat flux and (d) latent heat flux.

underlying land use pattern has the largest structure size show a significant different behavior than the other three spectra. For them an increase of structure size leads to an increase of entropy. The difference between the 15 m structure size and the 120 m is larger than the difference between the 120 m structure size and the 240 m structure size.

For the entropy spectra of the averaged sensible heat flux, shown in Figure 5.10 (c), it can be seen that increasing the structure sizes of uncorrelated structures lead to different entropy spectra. In addition, for the 15 m structure size (blue

5. Results

curve) and the 240 m structure size (red curve) it is not possible to find a height at which the land surface is negligible. However for the 120 m structure size (green curve) as well as the 480 m structure size (cyan curve), prominent heights at approximately 320 m and approximately 280 m height, respectively can be obtained. Unfortunately, these heights cannot be related to the structure sizes. For the entropy spectra of the averaged latent heat flux shown in Figure 5.10 (d), it can be seen that structure sizes of 120 m and 240 m, lead to similar results. Increasing the structure size from 15 m to 120 m lead to a decrease of entropy. Increasing the structure size to 480 m, the entropy spectrum significantly changes its shape.

It has to be taken into account that due to the change of the resolution of the underlying land use pattern, the PDF of the averaged parameters (cf. Table 4.3) change. Therefore, the conclusions for the dependency of the entropy spectrum to the resolution is not only an effect of the resolution, but moreover from the PDF of the parameter at the surface.

5.6 Comparison to other Methods

In order to validate the results of the entropy spectrum method, it is compared to the correlation coefficient function, R , and the centered root mean square error difference, E' . Together with the standard deviation, these are statistical parameters used in the Taylor diagram, explained in Section 3.1. Figure 5.11 shows an example Taylor diagram for the values of temperature averaged between 1300 - 1330 UTC for experiment (d). It can be seen that by taking into account many levels, the Taylor diagram is difficult to compare to the entropy spectrum. Therefore, for validation of the entropy spectrum method, it is compared to the correlation coefficient function R and to the centered root mean square error difference E' . Both the correlation coefficient function R and the centered root mean square error difference E' are measures for the structure aspect of heterogeneity, while the entropy is a measure of the information aspect of heterogeneity. A comparison between the three quantities will show if the structure aspect or the information aspect is important for the response of the averaged values of temperature, water vapor, sensible and latent heat flux. In the following the correlation coefficient

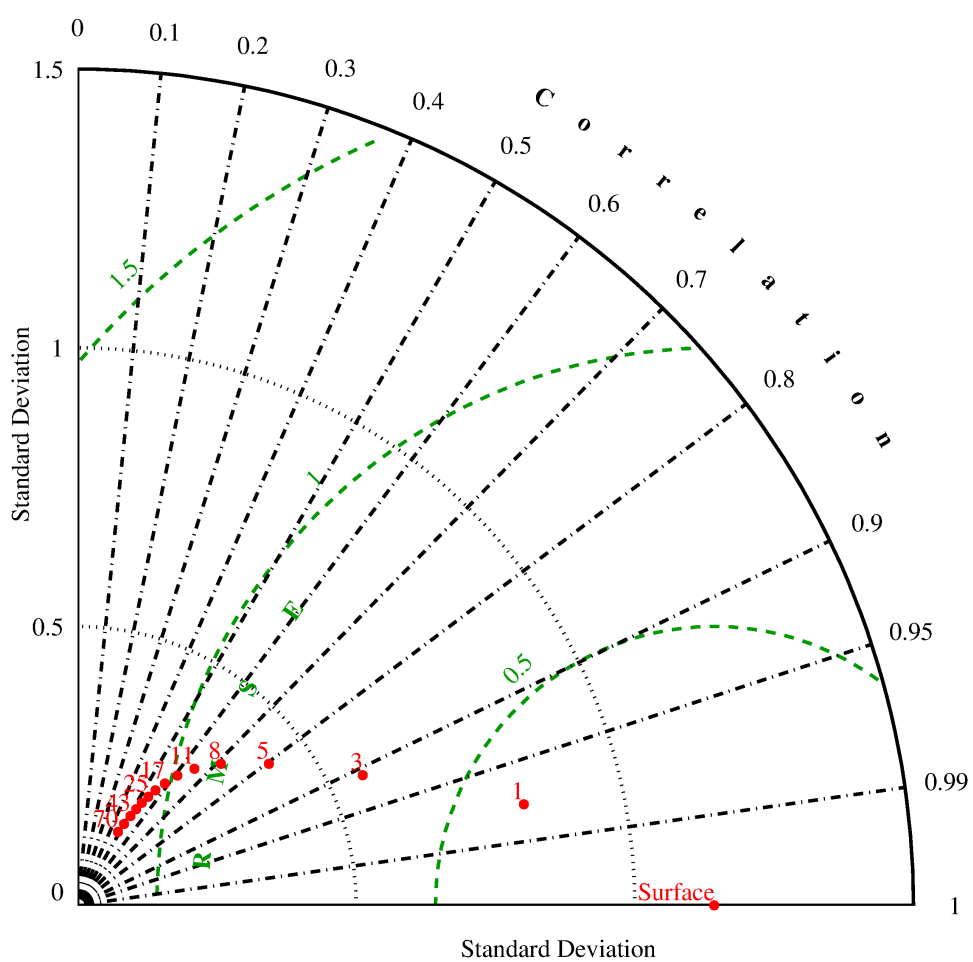


Figure 5.11: Example Taylor diagram for temperature averaged from 1300 - 1330 UTC for the numerical experiment with the original land use as input for the first 70 m.

5. Results

function R is written as correlation and the centered root mean square error difference E' is written as root mean square (RMS). As examples, the comparison is done for the constant land use input of experiment (a), the random land use input of experiment (c) and the original land use of experiment (d).

Figure 5.12 shows the results for experiment (a), the constant land use pattern, for the four parameters temperature, the water vapor, the sensible and latent heat fluxes averaged over a time period from 1300 - 1330 UTC. From Figure 5.12 (b), it can be seen that the correlation of the temperature, decreases fast with height in the first 20 m above ground. After a local minimum and a small increase until a height of 70 m, the correlation decreases slowly and reaches 0 at around 330 m. This means that at this height the temperature pattern has nothing in common with that at the surface. After 330 m, the correlation further decreases until it reaches a value of -0.22 at 388 m height, which means the two patterns are slightly anti correlated. After this height the correlation remains approximately constant. Comparing the correlation to the RMS it can be seen that the RMS increases fast until a height of 70 m. After that height, the RMS remains approximately constant, until it reaches a turning point a 265 m height, after which the RMS increases. Two local maxima are reached at 388 and 462 m height, respectively. It can be seen that the RMS maximum occurs at the same height as the local minimum of the correlation. The connection between correlation and RMS is as expected, since they are related via Equation (3.3). Therefore, it is sufficient to compare the shape of the RMS with the entropy, because the comparison of the correlation with the entropy will show a corresponding behavior. The entropy for temperature shows a similar behavior as the RMS. The entropy has a local maximum at 70 m. The minimum of entropy is reached at 265 m height. In addition, there are two local maxima at 388 and 462 m height. This is in good agreement with the prominent points of the correlation and the RMS. This connection is not a priori apparent, since the correlation as well as the RMS are measures of the structure aspect of heterogeneity, while the entropy is a measure of the information aspect of heterogeneity.

For water vapor the correlation decreases slower with increasing height than the

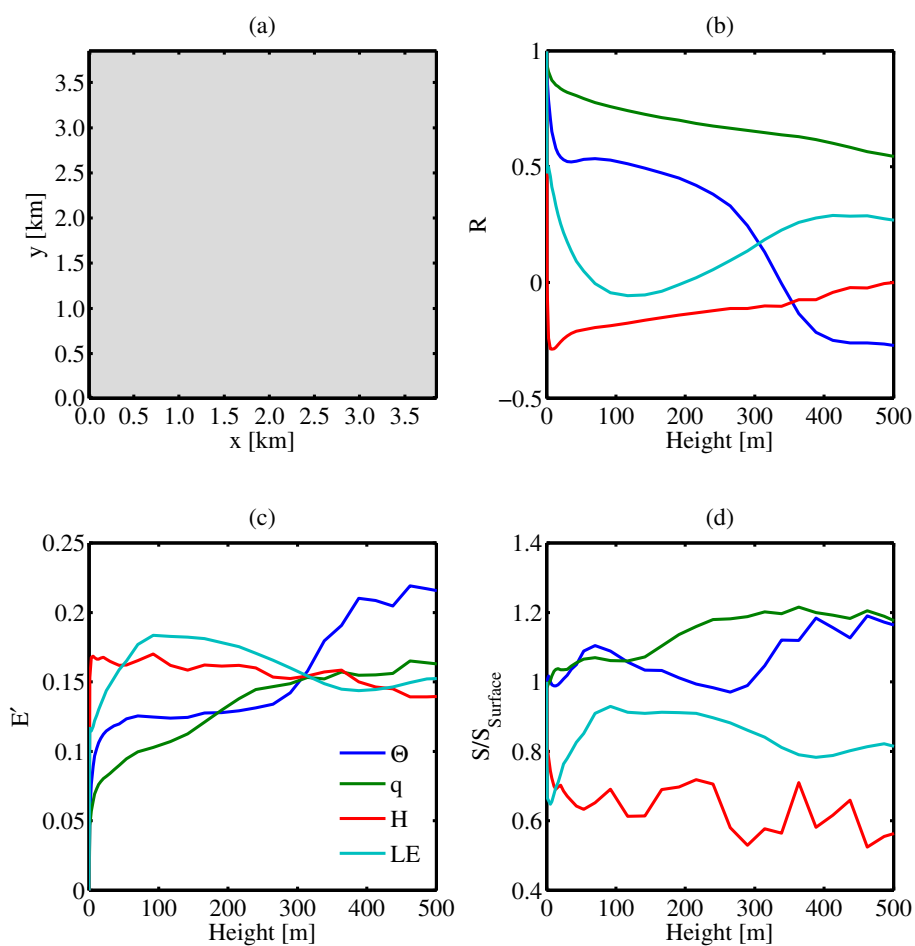


Figure 5.12: Comparison between correlation coefficient, the RMS and normalized entropy for the atmospheric responses. **(a)** The land use input for the numerical experiment. **(b)** The correlation coefficient function as a function of height for the four parameters temperature, water vapor, sensible heat and latent heat. **(c)** Centered root mean square error difference as a function of height for the same parameters as in (b). **(d)** Entropy normalized by the entropy at the surface for the same parameters as in (b).

5. Results

other three parameters. At 488 m height, the correlation has a value of 0.55. The corresponding plot of the RMS (green curve in Figure 5.12) shows increasing values. It can be seen that the values of the correlation for water vapor is larger than that for temperature. That means that the water vapor patterns in higher levels the correlations with the pattern at the surface are stronger than for temperature. For the RMS, the curve for temperature overpowers the curve for water vapor after 314 m height. The reason is that the absolute value of the RMS cannot tell how much two structures have in common. The behavior of the entropy spectrum is similar to that of RMS. For example there are two local maxima at 364 m and 462 m as well as a local minimum at 437 m, which corresponds to the features of E' . That means that for a constant land use the entropy method gives similar insights of the response of water vapor than the RMS. Therefore, the response of water vapor to a constant land use pattern can be described with a measure of structure as well as with a measure of the information content.

For sensible heat flux the correlation decreases rapidly with increasing height. After 11 m, the correlation is -0.23. Above that height, the correlation increases slowly to a value near 0 at 488 m height. The plot of the RMS shows the corresponding behavior. However, more fluctuations can be seen in the entropy spectrum. The entropy decreases rapidly from 1 to 0.69 at 14 m height. With increasing height, the entropy spectrum shows several local minima and maxima. For example, the maxima occur at heights of 92 m, 216 m and 364 m. These maxima can also be seen in the spectrum of the RMS. This is also true for the minima at 54 m, 142 m, 290 m and 462 m height. The similarity seen between the RMS and the entropy for sensible heat flux is also apparent for the entropy spectrum of the latent heat flux. Some of the prominent features are the maximum at 92 m height and the minimum at 388 m height. That means as for water vapor, the response of sensible and latent heat flux to a constant land use input can be either described by quantities describing the structure as well with the entropy spectrum.

For numerical experiment (c), with the random land use input, it can be seen from Figure 5.13 (b) that the correlations between the surface and the higher levels decrease faster with height than for the numerical experiments (a) and (d) (the

results for (d) are discussed below). For temperature, the correlation decreases slower above 43 m height and stronger again above 339 m height. Only in the height of 339 m the RMS shows a corresponding behavior as the entropy spectrum. They show both a local minimum at this height. The maximum of the RMS at 117 m can also be found in the entropy spectrum. The minimum of the entropy spectrum at 216 m height can also be found in the spectra of RMS. For water vapor the local maxima at 364 m and 462 m height, as well as the minimum at 388 m height can also be found in both the entropy spectrum and in the plot of the RMS. However, they are more difficult to obtain in the plot of the RMS. For the sensible heat flux the correlation and the RMS do not show the features of the entropy spectrum, which shows clear maxima and minima. The local minima in the correlation for the latent heat flux at 11 m height can be seen in the maximum of the RMS and in a minimum of entropy. However, the entropy maximum at 339 m height is not visible in the correlation plot and hard to obtain from the plot of the RMS. That means for a random land use input, the response of temperature and water vapor can be described with a quantity describing structure as well as with a quantity describing information. However, for the response of sensible heat flux, the information aspect reacts different, compared to the structure aspect. For the response of latent heat flux, structure and information aspect lead to similar results. However, the similarity is weaker than in the case of temperature and water vapor.

The comparison for the numerical experiment (d), which the land use pattern is taken from the real land-surface data, is shown in Figure 5.14. The comparison between the correlation and the entropy is different than for experiment (a) with the constant land use pattern as input (cf. Figure 5.12). Only for water vapor the plots of the RMS and the normalized entropy correspond to each other. Both show a maximum at 413 m. For the other parameters, Figure 5.14 (c) and (d) show similarities as well as differences. For temperature, the entropy shows a first minimum at 11 m height. Here the correlation still decreases and the RMS still increases. At 54 m height both the RMS and the entropy have a local maximum. The global entropy minimum at 314 m height is not very prominent in the spectrum of the RMS. For the sensible heat flux, both the correlation as well as the RMS do not

5. Results

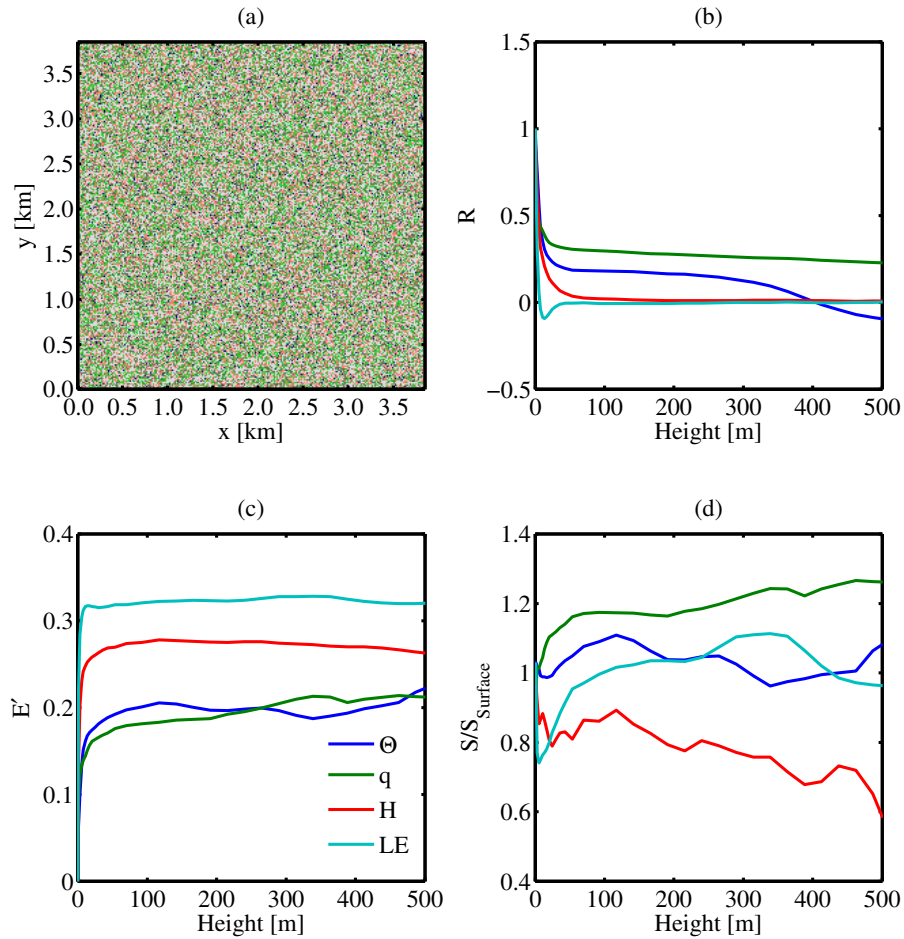


Figure 5.13: Comparison between correlation coefficient, RMS and entropy for the atmospheric responses. **(a)** An arrangement, where the center of the domain is forest surrounded by bare soil. **(b)** The correlation coefficient function as a function of height for the four parameters temperature, water vapor, sensible heat and latent heat. **(c)** Centered root mean square error difference as a function of height for the same parameters as in (b). **(d)** Entropy normalized by the entropy at the surface for the same parameters as in (b).

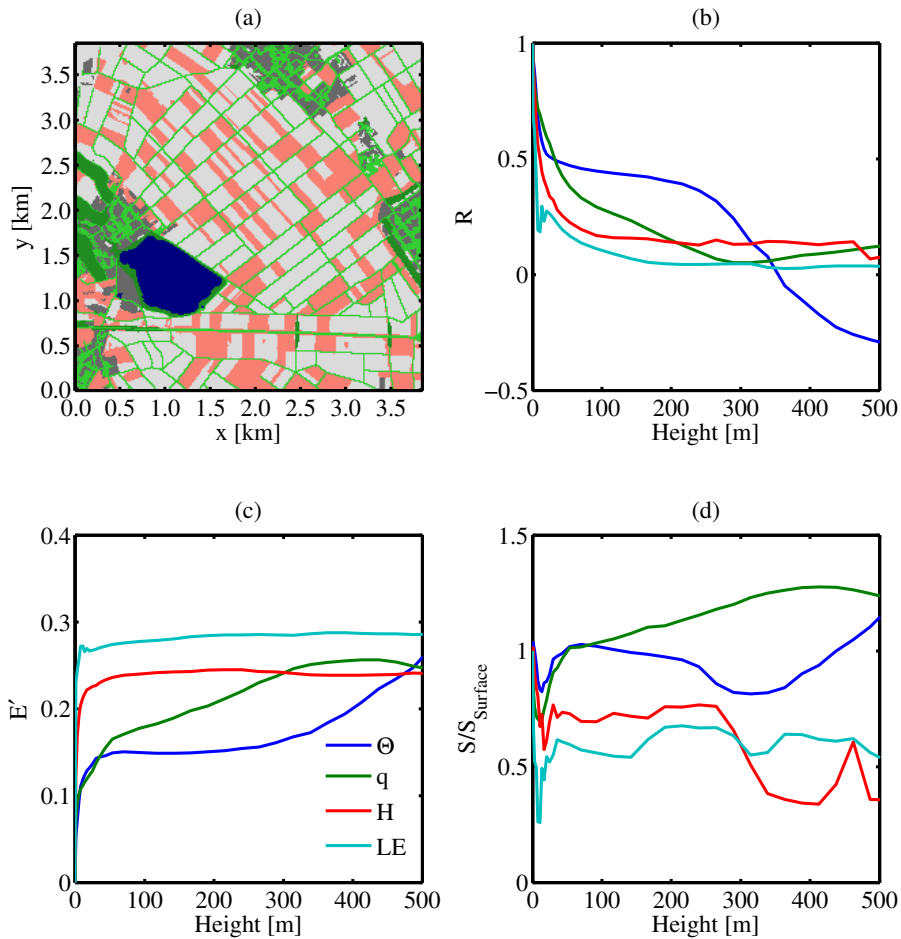


Figure 5.14: Comparison between correlation coefficient, RMS and entropy for the atmospheric responses. **(a)** The original land use data. **(b)** The correlation coefficient function as a function of height for the four parameters temperature, water vapor, sensible heat and latent heat. **(c)** Centered root mean square error difference as a function of height for the same parameters as in (b). **(d)** Entropy normalized by the entropy at the surface for the same parameters as in (b).

5. Results

show the features of the entropy spectrum: this exhibits a maximum at 265 m and 462 m height and a minimum at 388 m height. Only the second maximum can be recognized in the correlation spectra at 462 m height. For the latent heat flux, the correlation show fluctuations in the first 24 m above ground. This is also true for the RMS and the entropy. However none of the two other methods can reproduce the fluctuations of the latent heat flux entropy at higher levels. That means that for a realistic land use input only for water vapor the quantities of the structure aspect as well as the entropy show similar results. For temperature, sensible and latent heat flux, the comparison shows that the with the entropy spectrum it is possible to obtain insights about the dynamic responses. Only with this method it is possible to find the height where the influence of the land surface to the response of the sensible heat flux is negligible.

6 Conclusion

The main goal of the present thesis is to propose a method to quantify land-surface heterogeneity and to investigate the atmospheric responses to it. This study is embedded in a bigger research program. As described in the introduction the overall goal of the research program is to parametrize heterogeneous land-surface processes in weather and climate models. The steps necessary to improve the parametrizations include: (1) development of an LES model to obtain high-resolution data; (2) development of suitable decompositions of land-surface heterogeneity; (3) quantification of land-surface heterogeneity; (4) investigation of the propagation of land-surface heterogeneity in the atmospheric boundary layer; (5) describing the heterogeneity with only a few parameters in order to reconstruct land-surface heterogeneity; and (6) parametrization of land-surface heterogeneity in weather and climate models. In the following it is summarized how these points are dealt with in the present thesis and how this study has contributed to the improved knowledge of each point.

In Chapter 2 the basic theory necessary for the understanding of the LES-ALM (*Shao et al.* [2013]) is presented. LES-ALM is used to produce the high-resolution data [Step (1)]. Step (2) is dealt with in the present thesis in some detail by explaining the wavelet transformation, which decomposes land-surface data into low- and high-pass filtered parts, but keeps the prominent features of the heterogeneity unchanged. With this decomposition, a wavelet filtering scale is introduced. This filtering scale is necessary for the quantification of the information aspect of land-surface heterogeneity [Step (3)]. In Chapter 3 a review of the methods, such as the Taylor diagram, variance, variogram, spectral and PDF approaches, used for heterogeneity quantification is given. Many of the exist-

6. Conclusion

ing methods are useful for studying land-surface heterogeneity. However, most of them, for example, the variogram method, requires a large number of calculations, since the variogram calculates the squared distance for each point at a specific lag distance. Other methods such as the decomposition with the Fourier transformation are computationally cheaper, but the Fourier transformation does not preserve the patterns on different scales.

Land-surface heterogeneities have four different aspects: structure, information content, contrast and anisotropy. In the present thesis, the emphasis lies on the information aspect of heterogeneity. In Chapter 3, the entropy as a quantitative description of the information aspect of heterogeneity is discussed. By combining the information entropy with the wavelet transformation, the entropy spectrum is obtained. This method quantifies heterogeneity by measuring the information of the land-surface patterns on different scales. It can also be used to describe a pattern. In this context, a pattern is defined as the distribution of information as a function of (wavelet) scale. The entropy spectrum overcomes the difficulty of using the Shannon entropy as a single measure, i.e., it cannot distinguish the different patterns which have the same PDF. Based on the entropy spectrum, the dominant scale of a pattern can be defined (cf. Chapter 4).

The investigation of the propagation of land-surface heterogeneity (Step 4) is done in Chapter 5 by analyzing the responses of the atmospheric variables to different land-surface patterns in a series of numerical experiments using the LES-ALM. The difference between the numerical experiments lies only in the land-surface patterns used for the simulation. The land-use patterns tested include a homogeneous pattern, a pattern with only two land use types and a strong contrast between them, four different random patterns with different structure sizes, one real land-surface pattern, and wavelet filtered patterns. The simulation results of potential temperature, water-vapor-mixing ratio, sensible and latent heat flux are examined in considerable detail. The entropy spectrum analysis is applied to the instantaneous values and half-hourly averaged values of these variables. For all four variables, the atmosphere at high levels is dominated by the Eigen-turbulence-pattern. That means the influence from land-surface heterogeneity is destroyed by

the atmospheric motion. For investigated patterns, the results show that the shape of the entropy spectra depend more on the investigated variable than on the land-surface heterogeneity. In the following the main findings of the entropy analysis are summarized.

Although, the entropy spectra of potential temperature do not show a strong dependency of the underlying land-use inputs, some relations between the land surface and the behavior of potential temperature can be obtained. (i) The response of potential temperature to a homogeneous surface is similar to that to a random surface. (ii) For the instantaneous values, the entropy spectra show maxima between 340 - 388 m depending on the land surface. The maxima of the averaged potential temperature are above 400 m for experiments (e) and (f). The interpretation is that the Eigen-turbulence-pattern begins to superimpose the influence from the land-surface heterogeneity and it can be concluded that above these heights the influence of the land-surface heterogeneity becomes less important. (iii) For averaged potential temperature, the spatial distribution of the land use is more important than the structure size of uncorrelated land-use patterns. (iv) In addition, the results show that the PDF of the averaged potential temperature at the surface is more important than the correlations of the land-use patterns. That means, that similar PDF of the averaged potential temperature at the surface leads to similar responses of entropy spectrum of averaged potential temperature at higher levels. (v) If the scales of the low-pass entropy maxima is constant, then the entropy spectrum roughly follows the change of the scales of the high-pass entropy maxima. (vi) For correlated structures decreasing the resolution of the land-use input leads to an increase of entropy. For uncorrelated patterns changing the structure size, leads to different entropy spectra.

For the water-vapor-mixing ratio, the following results are obtained. (i) The entropy spectra of the instantaneous water-vapor-mixing ratio show maxima between 290 - 388 m depending on the land use. Above this height, it can be concluded that the influence of the land-surface heterogeneity begin to become less important. For the averaged water-vapor-mixing ratio, these height is at approximately 400 m nearly independent from the land-use input. (ii) The entropy spectra

6. Conclusion

of the averaged water-vapor-mixing ratio reacts in a similar way to a homogeneous land-use pattern, a random land-use pattern and land-use patterns with large structures. (iii) It can also be seen that the entropy spectra of the averaged water-vapor-mixing ratio show a similar behavior for land-use patterns with similar PDF but different spatial arrangements. (iv) If the scales of low- and high-pass entropy maxima stay nearly constant then the corresponding entropy spectrum is approximately constant. (v) For correlated land-use patterns, changing the structure sizes of the underlying land-use pattern has no significant effect on the entropy spectrum of the averaged water-vapor-mixing ratio. For uncorrelated land use patterns with not to large structure sizes, an increase of structure size leads to an increase of entropy.

For the entropy spectra of the sensible heat flux some of the results can be summarized as follows. (i) The entropy spectra of the instantaneous sensible heat flux show maxima between 314 - 413 m depending on the land-use pattern. For the entropy spectra of the averaged sensible heat flux maxima can be obtain at approximately 260 m height, for experiments with realistic land-surface pattern (experiments (d),(e) and (f)). Above this height, the influence of the land-surface heterogeneity begins to become less important. (ii) The shapes of the entropy spectra of the averaged sensible heat flux to the homogeneous land-use experiment and the response to the small-scale random land use experiment are different. (iii) The entropy as function of height shows oscillations. That means for the sensible heat flux, the results from heights which are close together vary more than in the case of potential temperature and water-vapor-mixing-ratio. (iv) Decreasing the resolution of the underlying land-use input, leads to more oscillations in the entropy spectrum. The comparison of different resolutions leads to the conclusion that for the studied patterns, small-scale heterogeneities do not lead to more dynamics in the entropy spectrum of the averaged sensible heat flux. The results show, that increasing the structure size of uncorrelated patterns lead to different entropy spectra. (v) For uncorrelated land-use inputs it is more difficult to obtain a height above that the influence of the land surface is negligible.

For the entropy spectra of the latent heat flux the following conclusions can be

obtained. (i) The height of the entropy maximum is difficult to obtain, since the entropy spectra of the instantaneous values of the latent heat flux show many oscillations. Therefore, the maxima of the entropy spectra lie in relatively large range between 92 - 364 m depending on the land-use pattern. The maxima of the entropy spectra of the averaged latent heat flux lie in a range between 92 - 412 m. However, for experiment (b) it is difficult to find a maximum and for some experiments the maxima are not very profound. (ii) Changing the resolution of the correlated land-use inputs, changes the entropy spectra.

The results of the comparison of the entropy to statistical methods, show that the response of the averaged water-vapor-mixing ratio, sensible and latent heat flux to a homogeneous land use input can be equally described with a measure of structure as well with a measure of information content. For a random land use input, the response of the averaged potential temperature and the averaged water-vapor-mixing ratio can be described with a quantity describing structure as well as with a quantity describing information. However, for the response of averaged sensible heat flux, the information aspect reacts different, compared to the structure aspect. For the response of the averaged latent heat flux, structure and information aspect leads to similar results. However, the similarity is weaker than in the case of the averaged potential temperature and the averaged water-vapor-mixing ratio. For a realistic land use input only for the averaged water-vapor-mixing ratio the quantities of the structure aspect as well as the entropy show similar results. The results of the averaged values of potential temperature, sensible and latent heat fluxes show, that with the entropy spectrum method it is possible to obtain insights about the dynamic responses. Only with this method, it is possible to find the height where the influence of the land surface to the response of the atmospheric variables is negligible.

For the analyzed data, the response of the parameters to the original land-use input with 15 m resolution is different from that of the level one Haar wavelet filtered land-use input. The level one Haar wavelet filtered land-use input corresponds to a 30 m resolution. However, the results from the 30 m and the 60 m resolution (level 2 Haar wavelet filtered land-use input) are similar. The entropy

6. Conclusion

spectrum method shows that the atmospheric responses of potential temperature and water-vapor-mixing-ratio are similar for the homogeneous experiment and for the random experiment with 15 m structure size.

In this research, the Haar wavelet is used. The investigation with entropy spectrum could be done with other wavelets. However, by using different wavelets, the same findings should be obtained, since the physical behavior of a system is independent of the analyzing method. The investigation presented in this thesis is not sufficiently comprehensive, since only nine different land use inputs and four different parameters were investigated. The study could be extended to other land-use patterns, other model resolutions, other models and other atmospheric parameters.

Coming back to the Steps (5) and (6), the reconstruction and the parametrization, the entropy spectrum can be used as a parameter that describes the information aspect of land-surface heterogeneity. However, other parameters are needed in order to reconstruct the pattern from the spectrum. To determine these missing parameters and to develop a reconstruction method that keeps all important features of the heterogeneity, are the next logical steps for the research. This parameter should tell if a specific atmospheric parameter is sensitive to a specific length scale of the land-surface heterogeneity. It should also indicate, whether it is necessary to simulate the system with a very high resolution. For Step (6), the heterogeneity parameter found in step (5) needs to be implemented into the model in order to find the optimal resolution for modeling of a specific heterogeneity (Step 6). However, Step (5) has to be finished before the parametrization of land surface heterogeneities can be improved in weather and climate models.

Bibliography

- Andraud, C., J. Lafait, and A. Beghdadi (1998), Entropic model for the optical properties of heterogeneous media: Validation on granular gold films near percolation, *Physical Review B: Condensed Matter and Materials Physics*, 57(20), 13,227–13,234, doi:10.1103/PhysRevB.57.13227.
- Avissar, R., and R. A. Pielke (1989), A parameterization of heterogeneous land surfaces for atmospheric numerical models and its impact on regional meteorology, *Monthly Weather Review*, 117(10), 2113–2136, doi:10.1175/1520-0493(1989)117<2113:APOHLS>2.0.CO;2.
- Bacry, E., J. Muzy, and A. Arneodo (1993), Singularity spectrum of fractal signals from wavelet analysis: Exact results, *Journal of Statistical Physics*, 70(3), 635–674, doi:10.1007/BF01053588.
- Beare, R., M. Macvean, A. Holtslag, J. Cuxart, I. Esau, J.-C. Golaz, M. Jimenez, M. Khairoutdinov, B. Kosovic, D. Lewellen, T. Lund, J. Lundquist, A. McCabe, A. Moene, Y. Noh, S. Raasch, and P. Sullivan (2006), An intercomparison of large-eddy simulations of the stable boundary layer, *Boundary-Layer Meteorology*, 118(2), 247–272, doi:10.1007/s10546-004-2820-6.
- Briggs, W. M., and R. A. Levine (1997), Wavelets and field forecast verification, *Monthly Weather Review*, 125(6), 1329–1341, doi:10.1175/1520-0493(1997)125<1329:WAFFV>2.0.CO;2.
- Brunsell, N., J. Ham, and C. Owensby (2008), Assessing the multi-resolution information content of remotely sensed variables and elevation for evapotranspiration in a tall-grass prairie environment, *Remote Sensing of Environment*, 112(6), 2977–2987, doi:10.1016/j.rse.2008.02.002.
- Brunsell, N. A., and M. C. Anderson (2011), Characterizing the multi-scale spatial structure of remotely sensed evapotranspiration with information theory, *Biogeosciences*, 8(8), 2269–2280, doi:10.5194/bg-8-2269-2011.

BIBLIOGRAPHY

- Brunsell, N. A., D. B. Mechem, and M. C. Anderson (2011), Surface heterogeneity impacts on boundary layer dynamics via energy balance partitioning, *Atmospheric Chemistry and Physics*, *11*(7), 3403–3416, doi:10.5194/acp-11-3403-2011.
- Chen, F., and J. Dudhia (2001), Coupling an advanced land surface-hydrology model with the penn state-NCAR MM5 modeling system. Part I: model implementation and sensitivity, *Monthly Weather Review*, *129*(4), 569–585, doi:10.1175/1520-0493(2001)129<0569:CAALSH>2.0.CO;2.
- Courault, D., P. Drobinski, Y. Brunet, P. Lacarrere, and C. Talbot (2007), Impact of surface heterogeneity on a buoyancy-driven convective boundary layer in light winds, *Boundary-Layer Meteorology*, *124*(3), 383–403, doi:10.1007/s10546-007-9172-y.
- Curran, P. J. (1988), The semivariogram in remote sensing: An introduction, *Remote Sensing of Environment*, *24*(3), 493–507, doi:10.1016/0034-4257(88)90021-1.
- Daubechies, I. (1990), The wavelet transform, time-frequency localization and signal analysis, *IEEE Transactions on Information Theory*, *36*(5), 961–1005, doi:10.1109/18.57199.
- Deardorff, J. W. (1970), A numerical study of three-dimensional turbulent channel flow at large Reynolds numbers, *Journal of Fluid Mechanics*, *41*(2), 453–480, doi:10.1017/S0022112070000691.
- Deardorff, J. W. (1980), Stratocumulus-capped mixed layers derived from a three-dimensional model, *Boundary-Layer Meteorology*, *18*(4), 495–527, doi:10.1007/BF00119502.
- Dolman, A. (1992), A note on areally-averaged evaporation and the value of the effective surface conductance, *Journal of Hydrology*, *138*(3), 583–589, doi:10.1016/0022-1694(92)90138-L.
- Fjellstad, W. J., W. E. Dramstad, G.-H. Strand, and G. L. A. Fry (2001), Heterogeneity as a measure of spatial pattern for monitoring agricultural landscapes, *Norsk Geografisk Tidsskrift-Norwegian Journal of Geography*, *55*(2), 71–76, doi:10.1080/00291950119811.
- Fließbach, T. (2010), *Statistische Physik*, Spektrum Akademischer Verlag, doi:10.1007/978-3-8274-2528-7.

- Ford, E. (1976), The canopy of a scots pine forest: Description of a surface of complex roughness, *Agricultural Meteorology*, 17(1), 9–32, doi:10.1016/0002-1571(76)90081-9.
- Garrigues, S., D. Allard, F. Baret, and M. Weiss (2006), Quantifying spatial heterogeneity at the landscape scale using variogram models, *Remote Sensing of Environment*, 103(1), 81–96, doi:10.1016/j.rse.2006.03.013.
- Garrigues, S., D. Allard, and F. Baret (2007), Using first- and second-order variograms for characterizing landscape spatial structures from remote sensing imagery, *IEEE Transactions on Geoscience and Remote Sensing*, 45(6), 1823–1834, doi:10.1109/TGRS.2007.894572.
- Giorgi, F. (1997), An approach for the representation of surface heterogeneity in land surface models. Part I: Theoretical framework, *Monthly Weather Review*, 125, 1885–1899, doi:10.1175/1520-0493(1997)125<1885:AAFTR0>2.0.CO;2.
- Gloaguen, E., and R. Dimitrakopoulos (2009), Two-dimensional conditional simulations based on the wavelet decomposition of training images, *Mathematical Geosciences*, 41(6), 679–701, doi:10.1007/s11004-009-9235-3.
- Haar, A. (1910), Zur Theorie der orthogonalen Funktionensysteme, *Mathematische Annalen*, 69(3), 331–371, doi:10.1007/BF01456326.
- Haken, H. (1983), *Synergetics*, Springer-Verlag Berlin Heidelberg, doi:10.1007/978-3-642-88338-5.
- Hannachi, A., I. T. Jolliffe, and D. B. Stephenson (2007), Empirical orthogonal functions and related techniques in atmospheric science: A review, *International Journal of Climatology*, 27(9), 1119–1152, doi:10.1002/joc.1499.
- Hechtel, L. M., R. B. Stull, and C.-H. Moeng (1990), The effects of nonhomogeneous surface fluxes on the convective boundary layer: A case study using large-eddy simulation, *Journal of the Atmospheric Sciences*, 47(14), 1721–1741, doi:10.1175/1520-0469(1990)047<1721:TEONSF>2.0.CO;2.
- Heinemann, G., and M. Kerschgens (2005), Comparison of methods for area-averaging surface energy fluxes over heterogeneous land surfaces using high-resolution non-hydrostatic simulations, *International Journal of Climatology*, 25(3), 379–403, doi:10.1002/joc.1123.
- Hintz, M., S. Lennartz-Sassinek, S. Liu, and Y. Shao (2014), Quantification of land-surface heterogeneity via entropy spectrum method, *Journal of Geophysical Research: Atmospheres*, 119(14), 8764–8777, doi:10.1002/2014JD021825.

BIBLIOGRAPHY

- Hough, S. E. (1989), On the use of spectral methods for the determination of fractal dimension, *Geophysical Research Letters*, 16(7), 673–676, doi: 10.1029/GL016i007p00673.
- Huang, H.-Y., and S. A. Margulis (2009), On the impact of surface heterogeneity on a realistic convective boundary layer, *Water Resources Research*, 45(4), doi: 10.1029/2008WR007175.
- Irannejad, P., and Y. Shao (1998), Description and validation of the atmosphere-land-surface interaction scheme (ALSIS) with HAPEX and Cabauw data, *Global and Planetary Change*, 19(1), 87–114, doi:10.1016/S0921-8181(98)00043-5.
- Kleissl, J., V. Kumar, C. Meneveau, and M. B. Parlange (2006), Numerical study of dynamic smagorinsky models in large-eddy simulation of the atmospheric boundary layer: Validation in stable and unstable conditions, *Water Resources Research*, 42(6), doi:10.1029/2005WR004685.
- Koster, R. D., and M. J. Suarez (1992), A comparative analysis of two land surface heterogeneity representations, *Journal of Climate*, 5(12), 1379–1390, doi: 10.1175/1520-0442(1992)005<1379:ACAOTL>2.0.CO;2.
- Kumar, P., and E. Foufoula-Georgiou (1993), A multicomponent decomposition of spatial rainfall fields: 1. Segregation of large- and small-scale features using wavelet transforms, *Water Resources Research*, 29(8), 2515–2532, doi: 10.1029/93WR00548.
- Kumar, P., and E. Foufoula-Georgiou (1997), Wavelet analysis for geophysical applications, *Reviews of Geophysics*, 35(4), 385–412, doi:10.1029/97RG00427.
- Kumar, V., J. Kleissl, C. Meneveau, and M. B. Parlange (2006), Large-eddy simulation of a diurnal cycle of the atmospheric boundary layer: Atmospheric stability and scaling issues, *Water Resources Research*, 42(6), doi: 10.1029/2005WR004651.
- Labat, D. (2005), Recent advances in wavelet analyses: Part 1. A review of concepts, *Journal of Hydrology*, 314(1), 275–288, doi: 10.1016/j.jhydrol.2005.04.003.
- Labat, D., J. Ronchail, and J. L. Guyot (2005), Recent advances in wavelet analyses: Part 2-Amazon, Parana, Orinoco and Congo discharges time scale variability, *Journal of Hydrology*, 314(1), 289–311, doi:10.1016/j.jhydrol.2005.04.004.
- Landau, L., and E. Lifshitz (1987), *Fluid Mechanics*, Pergamon Press.

- Leonard, A. (1975), Energy cascade in large-eddy simulations of turbulent fluid flows, *Advances in Geophysics*, 18, Part A, 237–248, doi:10.1016/S0065-2687(08)60464-1.
- Lhomme, J.-P. (1992), Energy balance of heterogeneous terrain: Averaging the controlling parameters, *Agricultural and Forest Meteorology*, 61(1-2), 11–21, doi:10.1016/0168-1923(92)90022-V.
- Liu, S., Y. Shao, M. Hintz, and S. Lennartz-Sassinek (2015), Multiscale decomposition for heterogeneous land-atmosphere systems, *Journal of Geophysical Research: Atmospheres*, 120(3), 917–930, doi:10.1002/2014JD022258.
- Mahrt, L. (2000), Surface heterogeneity and vertical structure of the boundary layer, *Boundary-Layer Meteorology*, 96(1-2), 33–62, doi:10.1023/A:1002482332477.
- Mandelbrot, B. B. (1983), *The fractal geometry of nature*, vol. 173, Macmillan.
- Moeng, C.-H. (1984), A large-eddy-simulation model for the study of planetary boundary-layer turbulence, *Journal of Atmospheric Sciences*, 41(13), 2052–2062, doi:10.1175/1520-0469(1984)041<2052:ALESMF>2.0.CO;2.
- Mölders, N., A. Raabe, and G. Tetzlaff (1996), A comparison of two strategies on land surface heterogeneity used in a mesoscale β meteorological model, *Tellus A*, 48(5), 733–749, doi:10.1034/j.1600-0870.1996.00012.x.
- Monin, A., and A. Obukhov (1954), Basic laws of turbulent mixing in the ground layer of the atmosphere (in russian), *Trudy Geofizicheskogo Instituta, Akademiya Nauk SSSR*, 24(151), 163–187.
- Morlet, J., G. Arens, E. Fourgeau, and D. Glard (1982), Wave propagation and sampling theory-part I: Complex signal and scattering in multilayered media, *Geophysics*, 47(2), doi:10.1190/1.1441328.
- Perron, J. T., J. W. Kirchner, and W. E. Dietrich (2008), Spectral signatures of characteristic spatial scales and nonfractal structure in landscapes, *Journal of Geophysical Research: Earth Surface (2003-2012)*, 113(F4), doi:10.1029/2007JF000866.
- Pope, S. B. (2000), *Turbulent Flows*, Cambridge University Press.
- Prager, W. (2004), *Introduction to Mechanics of Continua*, Dover Books.

BIBLIOGRAPHY

- Schomburg, A., V. Venema, R. Lindau, F. Ament, and C. Simmer (2010), A downscaling scheme for atmospheric variables to drive soil-vegetation-atmosphere transfer models, *Tellus B*, 62(4), 242–258, doi:10.1111/j.1600-0889.2010.00466.x.
- Shannon, C. (1948), A mathematical theory of communication, *Bell System Technical Journal*, 27(4), 623–656, doi:10.1002/j.1538-7305.1948.tb00917.x.
- Shao, Y., M. Sogalla, M. Kerschgens, and W. Brücher (2001), Effects of land-surface heterogeneity upon surface fluxes and turbulent conditions, *Meteorology and Atmospheric Physics*, 78(3-4), 157–181, doi:10.1007/s703-001-8171-3.
- Shao, Y., S. Liu, J. H. Schween, and S. Crewell (2013), Large-eddy atmosphere-land-surface modelling over heterogeneous surfaces: Model development and comparison with measurements, *Boundary-layer meteorology*, 148(2), 333–356, doi:10.1007/s10546-013-9823-0.
- Shaw, R., and U. Schumann (1992), Large-eddy simulation of turbulent flow above and within a forest, *Boundary-Layer Meteorology*, 61(1), 47–64, doi:10.1007/BF02033994.
- Shaw, R., G. Den Hartog, and H. Neumann (1988), Influence of foliar density and thermal stability on profiles of Reynolds stress and turbulence intensity in a deciduous forest, *Boundary-Layer Meteorology*, 45(4), 391–409, doi:10.1007/BF00124010.
- Skamarock, W., J. Klemp, J. Dudhia, D. Gill, D. Barker, M. Duda, X.-Y. Huang, and W. Wang (2008), A description of the advanced research WRF version 3, *NCAR Technical Note NCAR/TN-475+STR*, doi:10.5065/D68S4MVH.
- Smagorinsky, J. (1963), General circulation experiments with the primitive equations, *Monthly Weather Review*, 91(3), 99–164, doi:10.1175/1520-0493(1963)091<0099:GCEWTP>2.3.CO;2.
- Stull, R. B. (1988), *An Introduction to Boundary Layer Meteorology*, *Atmospheric and Oceanographic Sciences Library*, vol. 13, Springer Netherlands, doi:10.1007/978-94-009-3027-8.
- Sullivan, P. P., C.-H. Moeng, B. Stevens, D. H. Lenschow, and S. D. Mayor (1998), Structure of the entrainment zone capping the convective atmospheric boundary layer, *Journal of Atmospheric Sciences*, 55, 3042–3064, doi:10.1175/1520-0469(1998)055<3042:SOTEZC>2.0.CO;2.

- Taylor, K. E. (2001), Summarizing multiple aspects of model performance in a single diagram, *Journal of Geophysical Research: Atmospheres*, 106(D7), 7183–7192, doi:10.1029/2000JD900719.
- Van Sicen, C. D. (1997), Information entropy of complex structures, *Physical Review E: Statistical, Nonlinear, and Soft Matter Physicst*, 56, 5211–5215, doi:10.1103/PhysRevE.56.5211.
- Vereecken, H., S. Kollet, and C. Simmer (2010), Patterns in soil-vegetation-atmosphere systems: Monitoring, modeling, and data assimilation, *Vadose Zone Journal*, 9(4), 821–827, doi:10.2136/vzj2010.0122.
- Waldhoff, G. (2010), Land use classification of 2009 for the Rur catchment, CRC/TR32 Database (TR32DB), doi:10.1594/GFZ.TR32.1.
- Woodcock, C. E., and V. J. Harward (1992), Nested-hierarchical scene models and image segmentation, *International Journal of Remote Sensing*, 13(16), 3167–3187, doi:10.1080/01431169208904109.
- Woodcock, C. E., and A. H. Strahler (1987), The factor of scale in remote sensing, *Remote Sensing of Environment*, 21(3), 311–332, doi:10.1016/0034-4257(87)90015-0.

Acknowledgements

This work is supported by the DFG Transregional Cooperative Research Centre 32 “Patterns in Soil-Vegetation-Atmosphere-Systems: Monitoring, Modelling and Data Assimilation.” The simulations have been carried out with the Cologne High Efficient Operating Platform for Science (CHEOPS).

Erklärung

Ich versichere, dass ich die von mir vorgelegte Dissertation selbständig angefertigt, die benutzten Quellen und Hilfsmittel vollständig angegeben und die Stellen der Arbeit - einschließlich Tabellen, Karten und Abbildungen -, die anderen Werken im Wortlaut oder dem Sinn nach entnommen sind, in jedem Einzelfall als Entlehnung kenntlich gemacht habe; dass diese Dissertation noch keiner anderen Fakultät oder Universität zur Prüfung vorgelegen hat; dass sie - abgesehen von unten angegebenen Teilpublikationen - noch nicht veröffentlicht worden ist sowie, dass ich eine solche Veröffentlichung vor Abschluss des Promotionsverfahrens nicht vornehmen werde.

Die Bestimmungen der Promotionsordnung sind mir bekannt. Die von mir vorgelegte Dissertation ist von Professor Dr. Yaping Shao betreut worden.

Teilpublikation

Hintz, M., S. Lennartz-Sassinek, S. Liu, Y. Shao (2014), Quantification of land-surface heterogeneity via entropy spectrum method, *Journal of Geophysical Research: Atmospheres*, 119(14), 8764-8777, doi: 10.1002/2014JD021825.